University of California
Santa Barbara

# Molecular beam epitaxy and magnetotransport studies of thin films of the topological semimetal cadmium arsenide

A dissertation submitted in partial satisfaction
of the requirements for the degree

Doctor of Philosophy
in
Materials

by

Manik Goyal

Committee in charge:

Professor Susanne Stemmer, Chair
Professor Leon Balents
Professor Stephen D. Wilson
Professor Kunal Mukherjee

December 2020

The Dissertation of Manik Goyal is approved.

---

Professor Leon Balents

---

Professor Stephen D. Wilson

---

Professor Kunal Mukherjee

---

Professor Susanne Stemmer, Committee Chair

December 2020

Molecular beam epitaxy and magnetotransport studies of thin films of the topological semimetal cadmium arsenide



by

Manik Goyal

This thesis is dedicated to my parents

## Acknowledgements

It is impossible to imagine to complete the Ph.D. journey without the help and encouragement of others. I am blessed by their unconditional support. First, I would like to acknowledge and thank my advisor, Prof. Susanne Stemmer, for giving me this opportunity and providing me all the support needed during my graduate study. I am fortunate to have her guidance for this critical part of my career where I learned to ask the right questions, look at the problem at different angles, and identify the relevant and critical steps for doing science. Additionally, I appreciate her patience with my fast speaking habits, bad slides, and helping me to work on improving these. I am thankful to my committee members, Prof. Stephen Wilson, Prof. Leon Balents, and Prof. Kunal Mukherjee, for their guidance and helpful discussion during my Ph.D. I am grateful to the past and present group members for making my Ph.D. joyful and filled with learning: Santosh, Chirs, Timo, Honggyu, Jack, Evegeny, Brandon, Gift, Patrick, David, Alex, Evan, Salva, Tyler, Luca, Wangzhou, Omor, Nick, Hanbyeol, Tess, Biswajit, Kaveh. Their constant support made the work environment uplifting and positive. I especially thank Dr. Timo Schumann for being a great mentor and teaching me MBE and being efficient. I thank David and Evan for helping me with writing, giving me great suggestions, and Alex, Evan, and Tylor who proofread my thesis. I am glad to have such cheerful and motivating colleagues who happen to be good friends. I thank MBE staff Kurt and John for helping me to keep the MBE running, making the MBE lab environment welcoming and joyful. I am grateful to John for giving me his valuable life advice; I will always remember his lessons. I would like to extend my thanks to Amanda and Joanne for their support. I thank Amanda for tolerating my bad jokes and making the work environment so friendly. I truly cannot imagine a better workplace with such welcoming and helpful people. I thank you all for accepting me as a part of the family and helping me grow in

this critical part of my career.

I am thankful to my roommates Sophia and Joe for their constant support and help. I especially express my gratitude to Sophia for being so supportive and not making me feel far from my family. I also thank my officemate Jan and Jimmy for the fun discussion and conversation about life and career. Further, I also thank my friends who were an integral part of my Ph.D. journey and gave me moments that will remain in my memory for the rest of my life, especially: Elayne, Emily, Alan, Harsha, Mo, Naveen, Rubayne, Sam, Emmanuel, Kimberley, Sarah, Mia. I am thankful to my undergraduate friends: Aditya, Akash, Rajneesh for their support and for believing in me, and for never letting me feel any absence of siblings in my life. At last, I am most grateful to my parents and family for supporting me throughout my life and helping me achieved my goals.

# Curriculum Vitæ

Manik Goyal

## Education

| | |
|---|---|
| 2020 | Ph.D. in Materials (Expected), University of California, Santa Barbara. |
| 2013 | B.Tech. in Ceramic Engineering, Indian Institute of Technology, Banaras Hindu University (IIT-BHU) |

## Publications

- **M. Goyal**, D. A. Kealhofer, T. Schumann, and S. Stemmer, Magnetoresistance effects in cadmium arsenide thin films, *Applied Physics Letters* **117,** 170601 (2020). [doi]
- O. F. Shoron, **M. Goyal**, B. Guo, D. A. Kealhofer, T. Schumann, and S. Stemmer, Prospects of Terahertz Transistors with the Topological Semimetal Cadmium Arsenide, *Advanced Electronic Materials*, 2000676 (2020).[doi]
- **M. Goyal**, S. Salmani-Rezaie, T. N. Pardue, B. Guo, D. A. Kealhofer, and S. Stemmer, Carrier mobilities of (001) cadmium arsenide films, *APL Materials* **8,** 051106 (2020). [doi]
- H. T. Chorsi, S. Yue, P. P. Iyre, **M. Goyal**, T. Schumann, S. Stemmer, B. Liao and J. A. Schuller, Widely Tunable Optical and Thermal Properties of Dirac Semimetal $Cd_3As_2$, *Advanced Optical Materials* **8,** 1901192 (2020). [doi]
- S. Yue, H.T. Chorsi, **M. Goyal**, T. Schumann, R. Yang, T. Xu, B. Deng, S. Stemmer, J. A. Schuller and B. Liao, Soft phonons and ultralow lattice thermal conductivity in the Dirac semimetal $Cd_3As_2$, *Physical Review Research* **1,** 033101 (2019). [doi]
- H. Kim, **M. Goyal**, S. Salmani-Rezaie, T. Schumann, T. N. Pardue, J.-M. Zuo and S. Stemmer, Point group symmetry of cadmium arsenide thin films determined by convergent beam electron diffraction, *Physical Review Materials* **3,** 084202 (2019). [doi]
- O. F. Shoron, T. Schumann, **M. Goyal**, D. A. Kealhofer, and S. Stemmer, Field-effect transistors with the three-dimensional Dirac semimetal cadmium arsenide, *Applied Physics Letters* **115,** 062101 (2019). [doi]
- **M. Goyal**, H. Kim, T. Schumann, L. Galletti, A. A. Burkov, and S. Stemmer, The surface states of strained thin films of the Dirac semimetal $Cd_3As_2$, *Physical Review Materials* **3,** 064204 (2019). [doi]

- L. Galletti, T. Schumann, D. A. Kealhofer, **M. Goyal** and S. Stemmer, Absence of signatures of Weyl orbits in the thickness dependence of quantum transport in cadmium arsenide, *Physical Review B* **99,** 201401 (2019). [doi]
- D. A. Kealhofer, H. Kim, T. Schumann, **M. Goyal**, L. Galletti, and S. Stemmer, Basal-plane growth of cadmium arsenide by molecular beam epitaxy, *Physical Review Materials* **3,** 031201 (2019). [doi]
- L. Galletti, T. Schumann, O. F. Shoron, **M. Goyal**, D. A. Kealhofer, H. Kim, and S. Stemmer, Two-dimensional Dirac fermions in thin films of $Cd_3As_2$, *Physical Review B* **97,** 115132 (2018). [doi]
- **M. Goyal**, L. Galletti, S. Salmani-Rezaie, T. Schumann, D. A. Kealhofer, and S. Stemmer, Thickness dependence of the quantum Hall effect in films of the three-dimensional Dirac semimetal $Cd_3As_2$, *APL Materials* **6,** 026105 (2018). [Editors Choice] [doi]
- T. Schumann, L. Galletti, D. A. Kealhofer, H. Kim, **M. Goyal**, and S. Stemmer, Observation of the quantum Hall effect in confined films of the three-dimensional Dirac semimetal $Cd_3As_2$, *Physical Review Letters* **120,** 016801 (2018). [doi]
- S. Pal, G. Sharada, **M. Goyal**, S. Mukherjee, B. Pal, R. Saha, A.Sundaresan, S. Jana, O. Karis, J. W. Freeland, and D. D. Sarma, Effect of anti-site disorder on magnetism in $La_2NiMnO_6$, *Physical Review B* **97,** 165137 (2018). [doi]
- T. Schumann, **M. Goyal**, D. A. Kealhofer, and S. Stemmer, Negative magnetoresistance due to conductivity fluctuations in films of the topological semimetal $Cd_3As_2$, *Physical Review B* **95,** 241113 (2017). [doi]
- T. Schumann, **M. Goyal**, H. Kim, and S. Stemmer, Molecular beam epitaxy of $Cd_3As_2$ on a III-V substrate, *APL Materials* **4,** 126110 (2016). [doi]
- K.P. Murali, H. Sharma, P.M. Raj, D. Mishra, **M. Goyal**, K. Silver, E. Shipton, R. Tummala, Structure-magnetic property correlations in nickel-polymer nanocomposites, *Journal of Materials Science: Materials in Electronics* **27,** 154-162 (2016). [doi]
- C. Marini, B. Joseph, S. Caramazza, F. Capitani, M. Bendele, M. Mitrano, D. Chermisi, S. Mangialardo, B. Pal, **M. Goyal**, A. Iadecola, O. Mathon, S. Pascarelli, D. D. Sarma and P. Postorino, Local disorder investigation in $NiS_{(2-x)}Se_x$ using Raman and Ni K-edge x-ray absorption spectroscopies, *Journal of Physics: Condensed Matter* **26,** 452201 (2014). [FAST TRACK COMMUNICATION] [doi]

## Abstract

Molecular beam epitaxy and magnetotransport studies of thin films of the topological semimetal cadmium arsenide

by

Manik Goyal

$Cd_3As_2$ is a three-dimensional Dirac semimetal. Electrons in $Cd_3As_2$ behave like massless particles known as Dirac fermions. Their linear dispersion in momentum space results in novel properties, such as ultrahigh electron mobility, giant magnetoresistance, and chiral currents, among many others. Additionally, due to non-trivial topology of their electronic band structure, $Cd_3As_2$ has distinct surface and bulk electronic states.

In this dissertation, the epitaxial growth of $Cd_3As_2$ and its structural and electrical characterization are presented. $Cd_3As_2$ was synthesized by molecular beam epitaxy (MBE) which is a low energy deposition technique that enables the growth of high-quality thin films. First, I discuss the epitaxial growth of $Cd_3As_2$ in the theoretically predicted Dirac semimetal phase at low temperatures. Magnetotransport studies of quantum confined and biaxially strained $Cd_3As_2$ films showed transport signatures from robust two-dimensional surface states while the bulk electronic states were gapped out. Further, we explored the effect of dislocations on the carrier mobilities of the bulk and surface electronic states. Misfit dislocations were found to have little influence on the bulk carrier mobilities. In the next part of the study, we developed the growth of a capping layer by migration enhanced epitaxy to protect the surface states. In the last part, we discuss the anisotropic magnetoresistance and planar Hall effect in the $Cd_3As_2$ films as a combined effect of three mechanisms: the chiral anomaly, Berry phase, and orbital magnetoresistance.

# Contents

# Chapter 1

# Introduction

## 1.1 Topological semimetals

Topological semimetals are a distinct class of electronic materials that host relativistic fermions[1]. Weyl and Dirac semimetals are topological semimetal. Weyl semimetals are characterized by Weyl nodes at the Fermi level. The low energy excitation near the nodes is given by Weyl Hamiltonian $H = \pm v\vec{\sigma}.\vec{k}$[2, 3]. $\vec{\sigma}$ is the Pauli matrix, $v$ is the velocity, and $\vec{k}$ is the crystal momentum. The sign of the velocity defines the chirality of the nodes. Weyl semimetals are required to have broken time-reversal or/and inversion symmetry. When both TR and inversion symmetry are present, the Weyl nodes are 2-fold degenerate and the system is called a 3D Dirac semimetal. The Hamiltonian for a 3D Dirac material is described by four-component Dirac fermion[4]

$$H = \begin{pmatrix} v\vec{\sigma}.\vec{k} & 0 \\ 0 & -v\vec{\sigma}.\vec{k} \end{pmatrix}$$

Dirac fermions can be visualize as two copies of Weyl fermions with opposite chirality. This overlap is generally unstable and leads to a bandgap opening. 3D Dirac semimetals

are divided into two categories based on the Dirac nodes stabilizing mechanism. The first class is nonsymmorphic Dirac semimetals[5]. The Dirac semimetal depends on the nonsymmorphic nature of the crystallographic space group. The second type is described as topological Dirac semimetal. This class of 3D Dirac semimetal has a band inversion in the bulk. This bulk band crossing is protected by rotational symmetry of the crystal[6]

## 1.2 $Cd_3As_2$, a 3D Dirac semimetal

$Cd_3As_2$ and $Na_3Bi$ were the first materials to be identified 3D Dirac semimetals[7, 8]. $Cd_3As_2$ attracted special attention due to its chemical stability. $Cd_3As_2$ is a symmetry protected 3D Dirac semimetal where the bulk band crossing is protected by the 4-fold rotational symmetry of the crystal.

### 1.2.1 Crystal structure

$Cd_3As_2$ has a complex crystal structure and undergoes a polymorphic transitions at high temperatures. The $Cd_3As_2$ unit cell can be derived from a distorted antifluorite structure with two vacant positions on the Cd site. In this antifluorite subcell, As atoms form a face-centered cubic (FCC) array and the Cd atom form a distorted cube with two vacant sites at the vertices. The vacancy ordering changes at high temperatures.

At room temperature, $Cd_3As_2$ has a large body-centered tetragonal unit cell containing 160 atoms. This large unit cell is given by a $2\times2\times4$ stacking of distorted antifluorite sub-cells with two vacant Cd cations (Shown in Fig.1.1). These sub-cells are arranged in a specific manner so that the Cd vacancies acquire a three-dimensional ordering. These sub-cells are stacked in such a way that the plane containing the Cd vacant positions rotates. Therefore, the position of vacant sites is different in different antifluorite sub-cells. Two x-ray diffraction (XRD) studies proposed different structure for the room temper-

ature phase. In the earlier study, $Cd_3As_2$ was shown to have a non-centrosymmetric structure with space group $I4_1/cd$ [9]. In the recent structural study, $Cd_3As_2$ crystal strucutre is claimed to be centrosymmetric with $I4_1/acd$ space group [10, 11]. Moreover, a wide range of lattice constants ($a = 12.63 - 12.67$Å, $c = 25.42 - 25.48$Å) have been reported for $Cd_3As_2$[10, 9, 12].

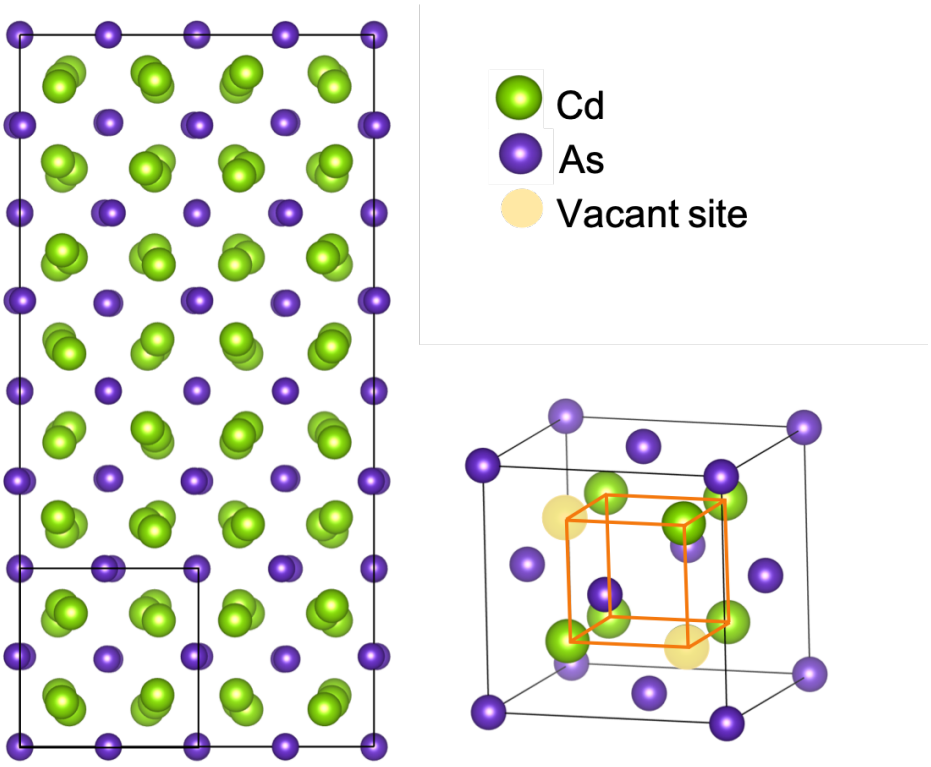


Figure 1.1: Tetragonal unit cell of $Cd_3As_2$ with the enlarged version of small subcell

The distribution of the vacant sites changes at high temperatures. The distribution of vacant sites is random at temperatures greater than 600 °C and $Cd_3As_2$ acquires a cubic structure with space group $Fm\bar{3}m$. In an intermediate temperatures range (600 °C > T > 220 °C), the vacancies distribution acquires a 2D ordering and the structures has a primitive tetragonal unit cell with space group $P4_2/nmc$ (No. 137) for 470 °C-600 °C[13] and changes to $P4_2/nbc$ (No. 133) for 220 °C-475 °C [14, 15].

### 1.2.2 Electronic structure

The band structure of $Cd_3As_2$ comprises As *4p* states near the Fermi level. In the early reports, the band structure of $Cd_3As_2$ was described by the Kane model[16] using the same band ordering as zinc blende III-V semiconductors [17]. Later, an optical and magnetotransport study showed an inverted band ordering[18] and $Cd_3As_2$'s band structure was then described using the Kane model for HgTe-type or $\alpha$-Sn-type inverted band structure [19, 20, 21]. HgTe and $\alpha$-Sn have a cubic structure. However, $Cd_3As_2$ has a tetragonal structure due to Cd vacancy ordering. To incorporate the effect of tetragonal structure, Bodnar proposed a crystal field splitting parameter[22] in the $Cd_3As_2$ band structure calculation [23]. This crystal field splitting parameter lifts the degeneracy between the heavy hole and light hole band. Recently, a first principle calculation showed that the crossing in these bands creates the Dirac nodes along Γ-Z direction (Fig.1.2)[7, 24]. This band crossing is stabilized by the $C_4$ symmetry of the crystal. These Dirac nodes are highly anisotropic and disperse linearly in a small energy scale. The Dirac nodes are formed by the p-type arsenic states. The inverted s-type state lies well below the Fermi level.

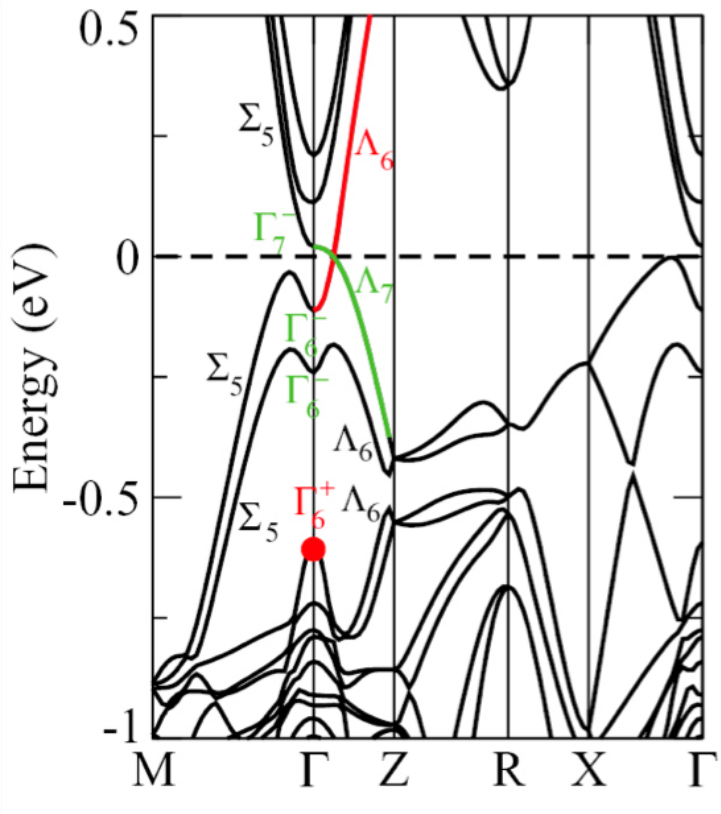


Figure 1.2: Band structure of $Cd_3As_2$ calculated form first principle calculation reported in ref.[7]. Reprinted with permission from ref.[7].

It is important to define the correct crystallographic structure to identify the electronic phase. The first calculation for the electronic band structure of $Cd_3As_2$ was done on $I4_1/cd$ which is non-centrosymmetric. Due to the lack of inversion symmetry, a small splitting in the Dirac nodes was observed, identifying $Cd_3As_2$ as a Weyl semimetal[7]. Recent detailed XRD studies showed $Cd_3As_2$ to have a centrosymmetric structure with $I4_1/acd$ and as a result, $Cd_3As_2$ is a 3D Dirac semimetal[10, 24].

## 1.3 Dirac/Weyl semimetal: surface states

The surface states for a topological semimetal are an arc connecting the projection of the bulk nodes[6, 25, 26, 27, 7]. For Weyl semimetals, the surface states are a single open arcs. The Fermi arc for Weyl semimetals is topologically protected due to the non-zero Chern number in between the Weyl nodes[25, 28]. For the case of Dirac semimetals, there are two copies of Weyl nodes superimposed on each other and as a result, a double Fermi arc on each surface is observed. These two Fermi arcs meet at the projection of bulk Dirac nodes. The topological protection of the surface states of Dirac material is an open question. It has been shown that with a small perturbation these double arcs can be deformed into a trivial Fermi loop[29]. However, due to the $\mathbb{Z}_2$ invariant in the bulk, the surface states of Dirac semimetal can not be destroyed completely.

Another special feature of Dirac and Weyl semimetals is that these surface states are crystallographic direction-dependent[7]. Figure 1.3 shows the surface states along different crystallographic directions for $Cd_3As_2$. For the projection along the $\Gamma - Z$ direction which is the (001) plane for $Cd_3As_2$, point-like surface states are expected. For other crystallographic directions, the surface states are arc-type.

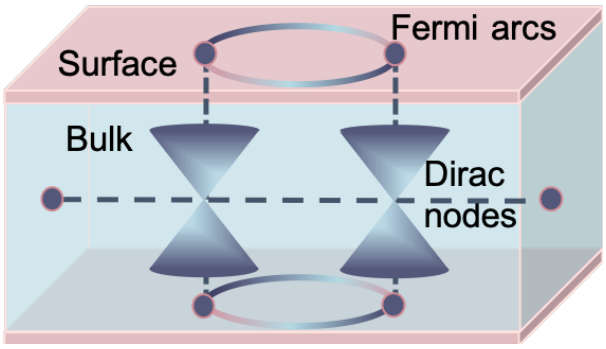


Figure 1.3: Schematic of surface and bulk electronic states of $Cd_3As_2$.

## 1.4 Magnetotransport

Magnetotransport studies are used to probe the non-trivial band topology of topological semimetals. Due to the relativistic nature of the carriers, topological semimetals exhibit unusual transport properties such as large magnetoresistance, high carrier mobility, chiral anomaly and small effective mass. In this study, we conducted a magnetoresistance study to probe the electronic structure of $Cd_3As_2$.

### 1.4.1 Classical Hall effect and magnetoresistance

Hall effect was discovered by E. H. Hall[30] as an induced transverse voltage when a magnetic field is applied perpendicular to the direction of the current. The Hall effect has been used extensively to investigate the electronic properties of semiconductors. In the classical limit, the Hall voltage is proportional to the applied magnetic field and applied current. The Hall coefficient is given as

$$R_H = \frac{E_y}{j_x B} = -\frac{1}{ne}.$$

$E_y$ is the induced electric field, $j_x$ is the applied current density, $B$ is the magnetic field, $e$ is the electron charge, and $n$ is the sheet density. The Hall coefficient is used to calculate the carrier density and mobility. The sign of the Hall coefficient is determined by the type of carriers present in the sample. In the classical limit, the Hall resistance is linear with $B$ for a single electronic band. In $Cd_3As_2$ two electronic states (surface and bulk) contribute to the electrical transport, therefore, a nonlinear Hall resistance is expected.

Longitudinal resistance changes with the applied magnetic field. A large nonsaturating linear magnetoresistance is observed for topological semimetals[31, 32, 33]. The magnetoresistance behavior is described by the resistivity tensor. For a 2D isotropic

material, the resistivity tensor is given as

$$\rho = \begin{pmatrix} \rho_{xx} & \rho_{xy} \\ \rho_{xy} & \rho_{xx} \end{pmatrix}.$$

The elements of the resistivity tensor are directly related to the experimentally measured longitudinal and Hall resistance as follow:

$$\rho_{xx} = \frac{R_{xx}w}{l},$$

$$\rho_{xy} = R_{xy}.$$

$w$ and $l$ are the width and length of the channel carrying the current. The conductivity tensor can be calculated simply by the inversion of the resistivity tensor

$$\sigma = \begin{pmatrix} \sigma_{xx} & \sigma_{xy} \\ \sigma_{xy} & \sigma_{xx} \end{pmatrix}.$$

The elements of conductivity tensor are given as

$$\sigma_{xx} = \frac{ne^2}{m^*}\langle\frac{\tau}{1+\omega^2\tau^2}\rangle,$$

$$\sigma_{xy} = -\frac{ne^2}{m^*}\langle\frac{\omega_c\tau^2}{1+\omega^2\tau^2}\rangle,$$

where $\tau$ is the scattering time and $\omega_c$ is the cyclotron frequency. For an ideal system, $\tau$ is independent of energy and the system shows no magnetoresistance. However, in a real system, $\tau$ changes with the magnetic field, and a magnetoresistance is observed. The longitudinal resistance shows a $B^2$ dependence and saturates at the high magnetic field.

The large magnetoresistance in topological semimetals is explained by the charge

compensation[31, 32, 33]. The magnetoresistance for the multicarrier system can be understood by the conductivity tensor. The total conductivity is calculated by adding the conductivity from individual carriers. For simplicity, we show the conductivity tensor for a two carriers system with n and p-type as carriers. The conductivity components are given by the following equations

$$\sigma_{xx} = \frac{|e|n_e\mu_e}{1+\mu_e^2B^2} + \frac{|e|n_h\mu_h}{1+\mu_h^2B^2},$$

$$\sigma_{xy} = \frac{e_en_e\mu_e^2B}{1+\mu_e^2B^2} + \frac{e_hn_h\mu_h^2B}{1+\mu_h^2B^2},$$

where $\mu_h(\mu_e)$ and $n_h(n_e)$ are the mobility and carrier density of hole (electron), respectively. These equations are given with the assumption that scattering time is independent of energy. As it is clear that, even for the energy-independent $\tau$, magnetoresistance exists. In our magnetotransport study on $Cd_3As_2$, we observed a non-linear Hall resistance as a signature of multi-carrier transport. The individual carrier density and their mobility were calculated by fitting the above conductivity equations. The resistivity components are calculated by the conductivity tensor. For the two carriers model, the longitudinal and transverse resistivity are given by the following equations

$$\rho_{xx} = \frac{\sigma_{xx}}{\sigma_{xx}^2+\sigma_{xy}^2} = \frac{(n_e\mu_e+n_h\mu_h)+(n_e\mu_e\mu_h^2+n_h\mu_h\mu_e^2)B^2}{(n_e\mu_e+n_h\mu_h)^2+\mu_h^2\mu_e^2(n_h-n_e)^2B^2}.\frac{1}{e},$$

$$\rho_{xy} = \frac{\sigma_{xy}}{\sigma_{xx}^2+\sigma_{xy}^2} = \frac{(n_h\mu_h^2-n_e\mu_e^2)+\mu_h^2\mu_e^2(n_h-n_e)^2B^2}{(n_e\mu_e+n_h\mu_h)^2+\mu_h^2\mu_e^2(n_h-n_e)^2B^2}.\frac{B}{e}.$$

This non-saturating behavior in resistance as a function of the magnetic field is more clear for the resistivity equations for two carriers (n and p-type). As can be seen from the resistivity equations when $n_h = n_e$ the longitudinal resistivity does not saturate and has a $B^2$ dependence.

The second explanation for the large magnetoresistance in topological semimetals is related to the topological nature of the electronic band. Due to non-trivial topology, the carriers are chiral, and as a result, backscattering is forbidden. By applying the magnetic field this protection is lifted resulting in a large magnetoresistance[34]. Moreover, these semimetals exhibit very large carrier mobility with low carrier density. Therefore, a large linear quantum magnetoresistance can be observed at a relatively low magnetic field[35, 7].

### 1.4.2 Carrier mobility and scattering time

Carrier mobility is an important parameter for electronic materials. The carrier mobility is determined by the electronic band structure and the material's quality. Ultrahigh mobility is another signature of topological materials.

For a parabolic electronic band, the average carrier mobility is given as follow:

$$\mu = \frac{e\langle\tau\rangle}{m^*},$$

where $e$, $\langle\tau\rangle$, and $m^*$ are the electron's charge, average scattering time, and effective mass, respectively. The effective mass of carriers in parabolic band is given by the inverse of the electronic band curvature.

Dirac and Weyl semimetals have linear band dispersion. The effective mass for linear dispersion can not be defined by the curvature of the band. The effective mass of the Dirac electron is given as $E_f/v_f$. The carrier mobility for Dirac electrons is given by the following equation

$$\mu = \frac{ev_f\tau}{E_f},$$

where $v_f$ and $E_f$ are the Fermi velocity and Fermi energy of the electrons. As is clear from the equation, the effective mass vanishes at the Dirac nodes. This very small effective mass leads to ultrahigh mobility for Dirac electrons. Long scattering time is another reason for high mobility in Dirac materials. This scattering time is calculated by the semi-classical Drude-Boltzmann transport approach[36, 37]. The transport scattering time for the isotropic band is given by

$$\frac{1}{\tau} = \int W(k,k')(1-\cos\theta)d^3k'.$$

$\theta$ is the scattering angle between the in-coming ($k$) and outgoing ($k'$) wave vectors. $W(k,k')$ is the scattering matrix which is calculated by the Fermi-golden rule. $(1-\cos\theta)$ term shows the weighting factor for the scattering mechanism. For conventional semiconductors, the scattering time is unaffected by the small-angle scattering[38]. Therefore, Hall mobility is mostly affected by large-angle scattering. This Hall mobility determines the conductivity in the material.

Quantum mobility, which is given as a single particle scattering time, determines the quantum level broadening of momentum eigenstates. The quantum mobility reflects the collision broadening of the Landau level and is experimentally measured by the quantum oscillations in the magnetic field. Quantum scattering time is affected by all angle scattering and is given as follow:

$$\frac{1}{\tau_q} = \int W(k,k')d^3k'.$$

The ratio between the quantum and classical scattering time is used to identify the dominant scattering mechanism in the system. This scattering time depends on the type and source of the scattering mechanisms.

For topological materials, there is an additional factor due to the chirality of the

carriers. The eigenvectors of the Dirac Hamiltonian are plane waves multiplied by the spinor. Therefore, the overlap of incoming and outgoing waves involves the overlap of the spinor that introduces an additional factor of $(1+\cos\theta)$ in the scattering time [39, 40, 41]. The scattering time for the Dirac electrons is given as follow:

$$\frac{1}{\tau} = \int W(k,k')(1-\cos\theta)(1+\cos\theta)d^3k'.$$

This additional factor $(1+\cos\theta)$ indicates that backscattering is suppressed for the Dirac electrons. The Hall mobility for Dirac electrons is weighted by a $(1+\cos\theta)(1-\cos\theta)$ factor that suppresses the small angle and large-angle scattering. For the quantum mobility, the scattering time is weighted by $(1+\cos\theta)$ which suppresses the high angle scattering. As a result, the scattering time is large for the Dirac electrons.

### 1.4.3 Landau quantization and quantum oscillations

Landau levels are the quantized energy levels due to cyclotron orbits of charged particles under a magnetic field[42]. The Landau level quantization depends on the electronic band dispersion. For a 2D parabolic dispersion, the Landau level energy states are given as

$$\varepsilon_n = (n+\frac{1}{2})\hbar\omega_c,$$

where $\omega_c$ is the cyclotron frequency and $n$ is the Landau level index. The Landau levels are equally spaced by $\hbar\omega_c$. For the 2 D Dirac dispersion, the Landau level energy states are given as

$$\varepsilon_n = v_f sgn(n)\sqrt{2e\hbar|B||n|}.$$

Landau quantization for the Dirac dispersion is different from the parabolic band. The energy of level depends on $\sqrt{n}$ and the Landau levels are not equally spaced in energy. Moreover, a field independent zeroth Landau level exists. This field independent zeroth level Landau level is unique to linear band dispersion. For 3D Dirac semimetals, the Landau level energy dispersion is given as

$$\varepsilon_n = v_f sgn(n)\sqrt{2e\hbar|B||n| + (\hbar k_z)^2}.$$

A field independent zeroth Landau level with constant energy exist. This zeroth Landau level is chiral and leads to many unusual magnetotransport properties in 3D topological semimetal.

### 1.4.4 Shubnikov-de Haas oscillations

Oscillations in conductivity with the magnetic field are known as the Shubnikov-de Haas (SdH) effect. This is a quantum mechanical effect due to the formation of Landau levels. SdH is generally observed at low temperature and high magnetic field. This effect is observed when the separation of Landau levels is larger than the thermal broadening ($k_B T$) and the scattering time is long enough so that, $\omega_c \tau > 1$. When a magnetic field is applied, Landau levels cross the Fermi level and as a result, the density of states oscillates. This oscillation in the density of states gives rise to oscillations in physical properties such as magnetic susceptibility, thermal conductivity. The oscillations in the conductivity are due to the change in the relaxation rate. The relaxation rate is proportional to the number of available energy states, therefore conductivity fluctuates with the density of states[43]. Due to the small effective mass of the carriers, the energy separation between Landau level for topological materials is large. Moreover, a large scattering time gives a long coherence length. Thus, these oscillations can be measured at the relatively low

magnetic field and high temperature for topological semimetals. The amplitude and frequency of the oscillations depends on the electrical parameters of the system. The oscillation in conductivity is given by[44]

$$\frac{\delta\sigma}{\sigma_0} = \sum_{r=1}^{\infty} \frac{1}{r^{1/2}} a_r \cos[2\pi(\frac{F}{B} - \frac{1}{2}) \pm \frac{\pi}{4}].$$

$\sigma_0$ is the background conductivity, $F$ is the oscillation's frequency and $r$ is the harmonic index. The $a_r$ term is given as follows

$$a_r \propto \frac{m_c B^{1/2}}{(S")^{1/2}} R_T(r) R_D(r) R_S(r).$$

$S"$ is the curvature of the Fermi surface along the direction of the magnetic field, $m_c$ is the cyclotron mass. $R_T, R_D, R_S$ are the damping factors given by Lifshitz-Kosevich (LK) formula.[45, 46, 47].

The cosine term in the conductivity equation describes the frequency and phase factor. The phase factor is $2\pi r(-\gamma + \frac{\delta}{r})$. $\delta$ is determined by the dimensionality of the Fermi surface. For a 3D Fermi surface, $\delta$ is $\pm 1/8$ and for a 2D Fermi surface $\delta$ is 0[48]. The dimensionality of the Fermi surface can be verified by the angle dependence of the oscillations' frequency. For the 2D Fermi surface, the frequency (F) changes as $1/\cos\theta$, where $\theta$ is the angle of rotation from out of the plane magnetic field. The additional phase factor $\gamma$ is given as

$$\gamma = \frac{1}{2} - \frac{\phi_B}{2\pi e},$$

where $\phi_B$ is the Berry phase. The Berry phase is an important phase factor that is used to identify the topological nature of carriers. Berry phase is a geometric phase acquired by adiabatic evolution in the parameter space. The Berry phase contains information about the topology of the electronic band structure. For topological materials, a non-zero

Berry phase of $\pi$ is observed.

The frequency of the oscillation is related to the external Fermi surface cross-sectional area ($S_{ext}$) by the Onsager's relation as follow:

$$F = \frac{\hbar S_{ext}}{2\pi e}.$$

The carrier density can be calculated from the frequency of oscillations. This frequency can be calculated by the Fourier transform of conductivity oscillation with 1/B. Further, the average value of $k_F$ can be calculated by the relation, $S_{ext} = \pi k_F^2$. For a 2D case, the carrier density is given by the following relation

$$n_{2D} = \frac{e}{\hbar} F.$$

### 1.4.5 Fan diagram

A fan diagram is the plot of $1/B_N$ values, corresponding to the nth minima in the conductivity, against the index $N$. The minima in the conductivity occurs when

$$2\pi \frac{F}{B} - \frac{1}{2} + \beta = (2N - 1)\pi.$$

This plot is a straight line and the slope of the line corresponds to the frequency of quantum oscillations. The intercept with the $N$ axis of the fan diagram when $1/B_N$ goes to zero gives the Berry phase.

### 1.4.6 Damping factors

The oscillations amplitude depends on the damping factors. The first damping factor is $R_T$. This factor is given by the LK formula as follow:

$$R_T(r) = \frac{2\pi^2 r k_B T/\hbar\omega_c}{\sinh(2\pi^2 r k_B T/\hbar\omega_c)}.$$

$\omega_c$ is the cyclotron frequency and is given by $eB/m^*$. $m^*$ is the effective cyclotron mass, $k_B$ is Boltzmann's constant. Under a fixed magnetic field, the oscillation amplitude depends on $R_T$ and by fitting the oscillation amplitude as a function of temperature, one can obtain $\omega_c$. The cyclotron effective mass is calculated from cyclotron frequency.

$R_D$ is called the Dingle damping factor. By fitting the magnetic field dependent oscillation amplitude at a constant temperature, one can obtain the Dingle temperature. The Dingle temperature indicates the Landau level broadening in the material. The Dingle damping factor is given as follows:

$$R_D(r) = \exp\frac{\pi r}{\omega_c \tau} = \exp\frac{-Kr\mu T_D}{B}.$$

$T_D$ is the Dingle temperature. The Dingle temperature is given as $T_D = \hbar/(2\pi k_B \tau_q)$. $\tau_q$ is the single-particle scattering time which is different than the classical scattering time. Quantum mobility can be calculated by using the scattering time and effective mass. $R_s(r)$ is damping due to the Zeeman spin splitting and given as

$$R_s(r) = \cos(\frac{\pi}{2} r g m^*),$$

where $g$ is the Lande factor.

### 1.4.7 Quantum Hall effect

The quantum Hall effect is observed in a 2D system due to the Landau quantization. In this effect, the longitudinal resistance oscillates, similar to Shubnikov-de Haas oscillations, and the Hall resistance shows plateaus with the magnetic field. The resistance of

these plateaus is quantized as

$$\rho_{xy} = \frac{2\pi\hbar}{e^2}\frac{1}{\nu}.$$

Where, $\nu$ is an integer. This quantized resistance is independent of the sample geometry and can be measured with high precision. The plateaus occur when the magnetic field satisfy the following condition:

$$B = \frac{2\pi\hbar n}{\nu e} = \frac{n}{\nu}\phi_0,$$

where $n$ is the electron density and $\phi_0 = 2\pi\hbar\ e$ is the flux quantum.

## 1.5 Chiral anomaly

The chiral anomaly is a chiral charge imbalance induced by the application of the collinear electric and magnetic fields (Fig.1.4). This anomaly was predicted in particle physics as broken chiral charge symmetry when fermions are coupled to an electromagnetic field [49, 50]. Later, Nielsen and Ninomiya showed that this chiral anomaly can be realized in condensed matter systems as longitudinal magnetoconduction when strong parallel electric and magnetic field applied[51]. This magnetic field induced current can be experimentally observed as negative longitudinal magnetoresistance (NLMR). The chiral anomaly in the Dirac and Weyl semimetal is due to the zeroth Landau level. The zeroth Landau levels are chiral and when a collinear magnetic field and the electric field is applied, the chiral electrons transfer to another zeroth Landau level creating the imbalance in the total chiral charge and lead to NLMR in the system. This chiral current depends on the relaxation rate and the Fermi level. Recently, this NLMR was described by semi-classical Boltzmann transport theory, indicating that the chiral anomaly induced NLMR can be observed in the low magnetic field[52]. The observation of NLMR has been

used as a smoking gun signature for topological semimetals[53, 54, 55, 56, 57, 58, 59].

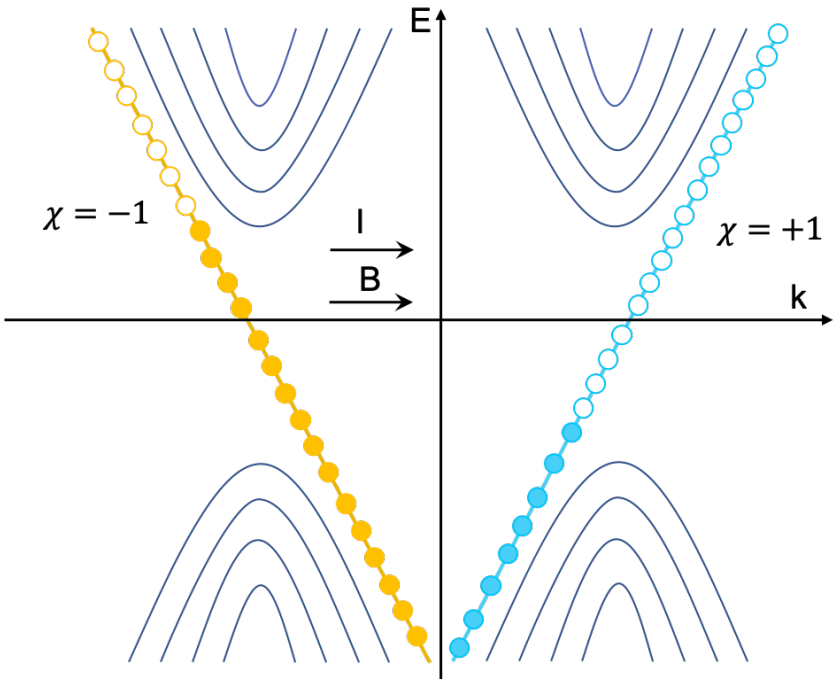


Figure 1.4: Chiral anomaly effect; chiral charge imbalance in the zeroth Landau level due to collinear magnetic and electric field.

## 1.6 Weyl orbits

The arc-type Fermi surface states is a unique signature of the topological semimetal. For the Weyl semimetals, these states are open arc type connecting the projection of bulk Weyl nodes of opposite chirality. Quantum oscillations in the magnetic field required a close Fermi surface. The quantum oscillations from these 2D surface states are predicted in the form of a closed orbit from the top and the bottom surface connected by the chiral Landau level of the bulk electronic states[60, 61]. These close orbits are called Weyl orbits. These quantum oscillations acquire an additional phase that depends on the thickness of the bulk. For a Dirac semimetal, Dirac nodes can be viewed as a superposition of two Weyl nodes with opposite chirality and, therefore have two Weyl

loops. Figure 1.5 shows the Weyl orbits for the Dirac and Weyl semimetal. For the Dirac semimetal, the electrons travel in opposite directions. For the Dirac semimetal, the Weyl orbit has a complicated behavior with the magnetic field. when a magnetic field is applied to the direction except $z$ the rotational symmetry is broken at the high magnetic field and as a result the chiral Landau level of bulk gaps out. In this situation, the quantum oscillations occur from individual surface states. The quantum oscillations from the Weyl orbit have a 2D character that can be verified by conducting an angle dependence magnetoresistance study that follows the $1/\cos\theta$ behavior. Quantum oscillations from these surface states were experimentally shown for the single crystal of $Cd_3As_2$ by fabricating different microstructure[62]. In another study done on $Cd_3As_2$ nanobelts, the transport from the Weyl orbit was demonstrated by measuring a thickness-dependent phase in quantum oscillations [63].

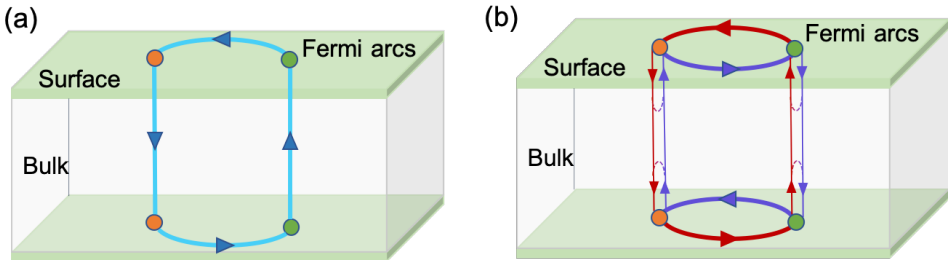


Figure 1.5: Weyl orbit in Weyl (a) and Dirac (b) semimetals. Figure (b) shows the two copy of Weyl orbits with opposite chirality.

## 1.7 Experimental Methods

### 1.7.1 Molecular beam epitaxy

We used the molecular beam epitaxy (MBE )to grow thin films of $Cd_3As_2$. MBE is a low energetic deposition that produces very high-quality films with atomic-level control. Figure 1.6 shows the schematic of the MBE used in this study. The system

is equipped with Knudsen effusion cells for group III elements (gallium, indium, and aluminum), $Cd_3As_2$ and cracker sources for group V elements (antimony and arsenic). The chamber is installed with an RHEED (reflection of high energy electron diffraction) source operating at 15 kV to monitored the growth *in-situ*. The growths were done in an ultrahigh vacuum of $10^{-10}$ Torr. The ultrahigh vacuum in the growth chamber was maintained by constantly running ion and cryogenic pumps.

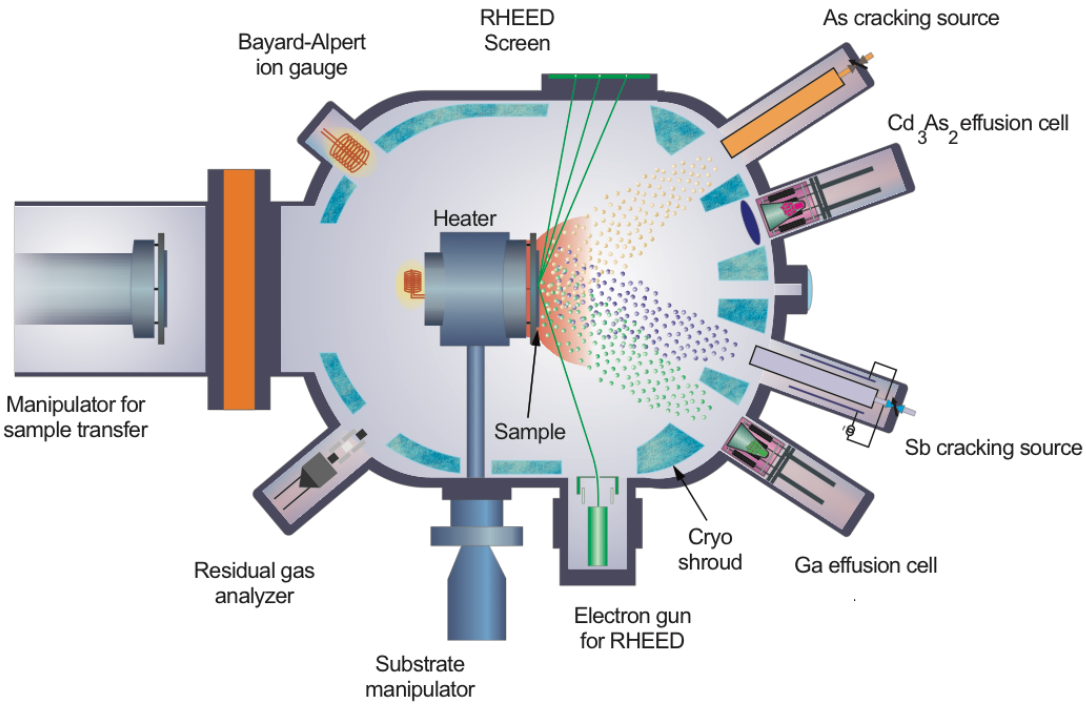


Figure 1.6: Schametic of MBE chamber used for the growth.

The substrate temperature plays an important role in determining the growth quality and to control the growth mode. Therefore, it is crucial to have consistent and reliable temperature readings. In our early growth studies, substrates were loaded on a tungsten

block. To increase the thermal homogeneity, a quartz plate was used on the back of the substrates. Substrates were heated by radiative heating from a heater sitting behind the blocks. The temperature was measured by a thermocouple located on continuous azimuthal rotation (CAR). This thermocouple is heated by the back radiation from the block. Therefore, the thermocouple does not measure the absolute substrate temperature accurately. Moreover, temperature readings depended on the block and sample position. The repeated use of blocks and chemical etching affects the block's absorption and radiation. This created a change in the temperature readings with time. A band-edge pyrometer was installed to address this issue. This band edge pyrometer measure the temperature directly from the substrates. In this method, the transmission from the substrate is measured by an infrared detector. This transmission spectrum is fitted to find the band edge and the substrate temperature is extracted. However, this technique is limited to relatively large bandgap material, and does not work for the low-temperature range. $Cd_3As_2$ has a zero bandgap and the growth is limited to low temperature. This method is not useful to measure the growth temperature for $Cd_3As_2$. A low-temperature optical pyrometer was installed to address this problem. To use this pyrometry, the substrate loading mechanism was modified. In this case, substrates were attached to molybdenum blocks by gallium bonding. This bonding provides thermal contact from block to substrates and increases the temperature homogeneity. The temperature is directly measured from the substrate by the optical pyrometer.

An atomic hydrogen source was installed in the buffer chamber for native oxide removal from substrates. The hydrogen molecules were cracked by the high energy electron beam. This electron beam is generated by a filament and accelerated with a high voltage of 12 kV.

### 1.7.2 Hall and magnetotransport measurements

Magnetotransport measurements were done in Van der Pauw and Hall bar geometries. For the Van der Pauw method, 10×10 mm$^2$ pieces were used. For contacts, 50 nm Ti and 200 nm Au were deposited on the corner of the sample (Fig.1.7).

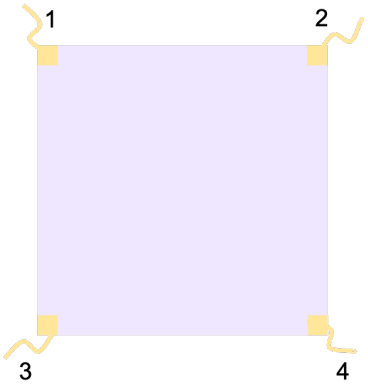


Figure 1.7: Schematic of measurement geometry for Van der Pauw method.

The current was applied on one edge of the sample and voltage drop was measured across the opposite edge. The resistance was calculated as follow:

$$R_{12,34} = \frac{V_{34}}{I_{12}}.$$

The resistance was measured in the vertical and horizontal direction and the average of these values was calculated. The sheet resistance is given by

$$R_s = \frac{\pi R}{\ln 2}.$$

R is the average resistance. The Hall resistance is measured diagonally. The Hall resistance is given as

$$R_H = \frac{R_{14,23} + R_{23,41}}{2}.$$

For high accuracy, most of the magnetotransport measurements were done in the Hall bar structure(Fig. 1.8). The Hall bar was fabricated by contact photolithography in the cleanroom. Mesa etch was done by the Ar-ion milling and the 50 nm/150 nm thick Ti/Au were deposited for metal contacts. The contact pads are larger than the Hall bar width to minimize the current inhomogeneity in the bar. The size of the Hall bar is defined by the width of the bar and the separation between the contacts. The study was done on 100×100 $\mu$m$^2$ and 50×50 $\mu$m$^2$ Hall bars. Two contacts were used to apply the current in the bar. The longitudinal and transverse resistance was calculated by measuring the voltage drop along and across the bar gives as follow:

$$R_{xx} = \frac{V_{xx}}{I},$$

$$R_{xy} = \frac{V_{xy}}{I}.$$

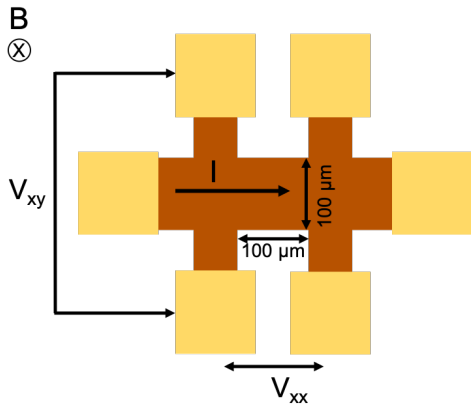


Figure 1.8: Schematic of Hallbar used for the electrical transport.

## 1.8 Permissions and Attributions

1. Figure (1.2) of chapter 1 has been adapted with permission from ref.[7]. This figure is copyrighted by the American Physical Society.

2. Some content of chapter 2 has previously appeared in APL Materials **4,** 126110 (2016)[64] and APL Materials **6,** 026105 (2018)[65]. The content is licensed under Creative Commons Attribution (CC BY 4.0) by the AIP Publishing LLC, and reproduced here.

3. Some content of chapter 2 has previously appeared in Physical Review B **95,** 241113 (2017)[66] and Physical Review Materials **3,** 064204 (2019)[67]. It is Copyrighted by the American Physical Society and reproduced here with permission.

4. The STEM study in chapter 3 was done by Salva Salmani-Rezaie. Some content of this chapter has previously appeared in APL Materials **8,** 051106 (2020)[68]. It is licensed under Creative Commons Attribution (CC BY 4.0) by the AIP Publishing LLC, and reproduced here.

5. Some content of chapter 4 has previously appeared in Physical Review Materials **3,** 064204 (2019)[67]. It is Copyrighted by the American Physical Society and reproduced here with permission.

6. Some content of chapter 4 has previously appeared in APL Materials **6,** 026105 (2018)[65]. It is licensed under Creative Commons Attribution (CC BY 4.0) by the AIP Publishing LLC, and reproduced here.

7. The content of chapter 5 has previously appeared in Applied Physics Letters **117,** 170601 (2020)[69]. It is Copyrighted by the AIP Publishing LLC and reproduced here.

# Chapter 2

# Epitaxial growth of $Cd_3As_2$

The growth of high-quality thin films is an important step to utilize $Cd_3As_2$ for device applications. Thin films provide a platform for systematic study to explore the underlying physics of different quantum phases and engineer them by epitaxial strain, heterostructure, and quantum confinement. Previously, the thin-film growth of $Cd_3As_2$ is explored by different methods such as pulsed laser deposition[70, 71], thermal evaporation[72, 73, 74, 75, 76, 77, 78, 79]. Most of these growth studies were done on amorphous or weakly bonded substrates with no epitaxial relations. The $Cd_3As_2$ films were amorphous or polycrystalline with significantly lower carrier mobility in comparison to single-crystals[34].

In this chapter, the epitaxial growth of $Cd_3As_2$ and different buffer layers is discussed. In the first part, the growth of (112)-oriented $Cd_3As_2$ on GaSb and CdTe is discussed. In the second part, the growth of lattice-matched alloys along (111) and (001) orientations are discussed.

## 2.1 Selection of substrates

Substrates play a crucial role in epitaxy. Ideally, substrates with a similar atomic arrangement and lattice spacing to the $Cd_3As_2$ are the best choice for the epitaxial growth. Moreover, surface energies and bonding energy play significant roles in the growth and determines the substrates' suitability for epitaxy. There was no prior epitaxial growth study for $Cd_3As_2$. Thus, our first goal was to explore the substrates for $Cd_3As_2$ epitaxy. An initial growth study for (112)-orientated $Cd_3As_2$ was conducted. (112) is the preferred growth plane for $Cd_3As_2$ as shown by single-crystal studies[10, 80]. Hence, the substrates for this orientation were first explored. The atomic arrangement of $Cd_3As_2$ along (112) plane is similar to the atomic arrangement of (111) plane for cubic zincblende structure. Figure 2.1 shows the comparison of (112) plane of $Cd_3As_2$ with (111) plane of GaAs. GaAs has a zinc blende structure. The two surfaces show a similar arrangement of As atoms denoted by the hexagon showing the potential for the epitaxial relationship between $Cd_3As_2$ and GaAs. The spacing of As in the hexagon for $Cd_3As_2$ is 4.4-4.6 Å. For zinc blende structure, a wide range of III-V and II-VI substrates are commercially available in this spacing range. Therefore, the substrates with the zinc blende structure were selected.

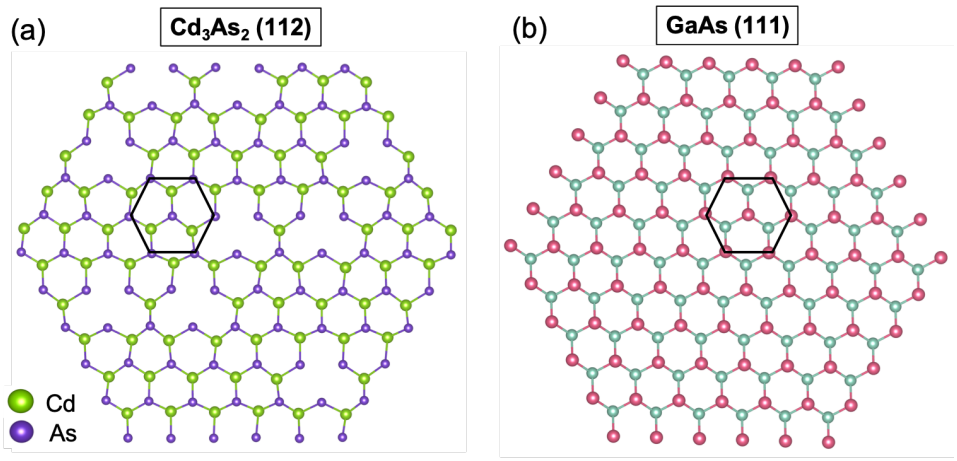


Figure 2.1: Atomic arrangements of top two atomic layers of $Cd_3As_2$ (112) plane (a) and GaAs (111) plane (b).

Figure 2.2 shows the lattice spacing and bandgap for commercially available semiconductor substrates along with the $Cd_3As_2$ pseudocubic unit cell parameters. The closest semiconductors compounds to $Cd_3As_2$ with zincblende structure are the antimonides (GaSb, InSb, AlSb) and the tellurides (ZnTe and CdTe) (shown in Fig.2.2) and thus, are a first choice of selection for $Cd_3As_2$ epitaxy. III-V (GaSb and AlSb) semiconductor compounds are especially interesting due to their well-developed epitaxial growth. This enables the growth of an *in-situ* buffer layer to provide a clean surface for further growth. Additionally, by alloying III-V compounds ($Al_xIn_{(1-x)}Sb$ and $In_xGa_{(1-x)}Sb$), lattice-matched pseudo substrates for $Cd_3As_2$epitaxy can be developed. The lattice-matched alloys minimize the structural defects produced by lattice misfit and allows for strain studies and band engineering of $Cd_3As_2$. In the early stage, the growth of $Cd_3As_2$ on GaSb and CdTe is developed and compared.

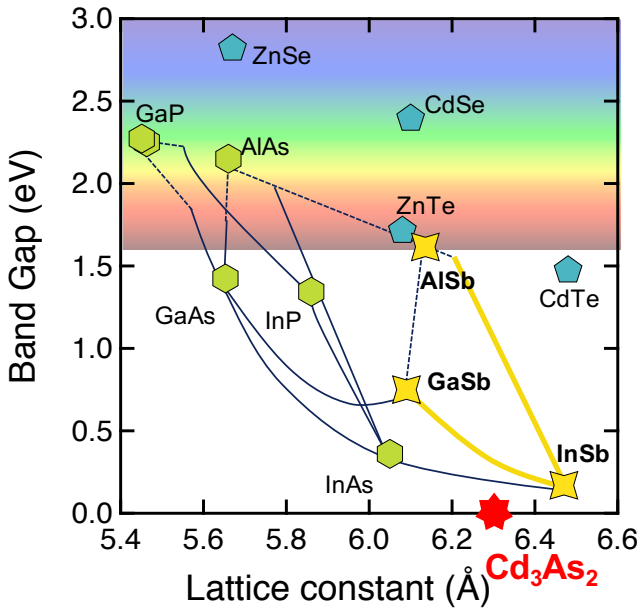


Figure 2.2: Bandgaps and lattice parameters for the different compound semiconductors and $Cd_3As_2$.

## 2.2 Growth of $Cd_3As_2$ on lattice-mismatched substrates

### 2.2.1 Epitaxy of III-V semiconductors

The molecular flux ratio between the group V and III elements (V/III ratio) and substrate temperature were optimized to find the growth window for group III-V semiconductor epitaxy. Group V elements have a high vapor pressure in comparison to group III elements. For thin film growth, the sticking coefficient for the group V molecule is temperature-dependent dropping from unity at high temperature. The sticking coefficient for group III elements remains close to one for a wide temperature range and controls the growth rate. Generally, a high growth temperature is desired to produce

high structural quality. At high temperatures, molecules have a long diffusion length on the surface that promotes two-dimensional growth. Therefore, excess group V flux in comparison to group III is needed. The excess group V desorbs from the surface leaving the stoichiometric III-V compounds. The desorption of group V increases with increasing the growth temperature that opens the growth window by allowing a wide range of group V flux over group III flux. At sufficiently high growth temperature and V/III ratio greater than one, the V/III flux-ratio controls the growth mode. These different growth modes and their transformation with the ratio have been studied extensively in the past and details can be found elsewhere[81]. For our purpose, we developed the growth of Sb based III-V compounds.

The growth of Sb based III-V compounds and alloys were developed for $Cd_3As_2$ growth study. As mentioned earlier, these compounds are structurally suitable substrates for $Cd_3As_2$ epitaxy. Sb is relatively less volatile in comparison to other group V elements (As and P), resulting in a narrower growth window and a lower V/III flux ratio[82, 83]. For antimonides, when the flux ratio is higher than an optimal value, the growth mode shift towards 3D growth, unlike other As-based III-V, due to the limited diffusion of group III adatoms caused by excess Sb molecules[82]. When the flux ratio is lower than a certain value, the growth swifts toward a 3D mode due to the short diffusion length of group III adatoms and results in a rough surface. Hence, an optimal flux ratio and substrate temperature were determined by growing a series of films. The film quality was measured by monitoring *in-situ* reflection of high energy electron diffraction (RHEED) during and after growth and studying the evolution of surface morphology measured by atomic force microscopy (AFM) with different growth parameters. Initially, the growth of GaSb was developed for (111) orientation.

### 2.2.2 Growth of GaSb

we developed the growth of GaSb on (111) GaAs substrates. As received GaSb substrates are covered by a native oxide due to air exposure. A surface treatment process was optimized to remove the native oxides. Finding the optimal process for oxide removal with low damage is challenging, since, the rigorous oxide removal steps such as high temperature or concentrated acid damage the surface, and gentle cleaning does not remove the oxide thoroughly. Growing an *in-situ* buffer layer provides a clean surface to grow by covering the damage and roughness caused by oxide removal and surface cleaning steps. Epitaxial growth of GaSb is well-developed along (001) orientation, however, there are very few MBE studies reported for (111)-orientated GaSb[84].

#### Early optimization

An initial optimization for the GaSb growth was done on GaSb substrates. (111)A GaSb (Ga polar) and (111)B GaSb (Sb polar) substrates were tested. The growth was done on 10×10 $mm^2$ size pieces of GaSb, diced from a 2 inch wafer. Before loading, the substrates were cleaned by solvent (acetone and isopropanol) in an ultrasonic cleaner and a chemical etch in concentrated HCl for 5 minutes was done to remove the native oxide. The substrates were loaded on the molybdenum blocks and held by pins (discussed in chapter 1 MBE section). After loading, the substrates were baked in the load lock chamber for 2 hours at 200 °C to remove the moisture and organic contaminants. Before growth, annealing at 600 °C substrate temperature under $2.5\times10^{-7}$ Torr Sb flux was done for 2 minutes to remove remaining oxides. A Knudsen type effusion cell is used to obtain Sb molecular flux in this initial growth studies which supplies $Sb_4$ molecules. A series of films with different group V/III ratio at 500 °C substrate temperature were grown.

A series of GaSb samples were grown by varying the III/V ratio from 3 to 7. The beam flux measurement (BFM) values were used to calculate the flux ratio that is not necessarily the same as the actual molecular flux. All the films were grown for 20 minutes. After growth, the surface morphology was studied by AFM. The V/III flux ratio has a significant effect on the surface quality. The films grown with a lower ratio (<5) showed a 3D growth mode due to the relatively large supply of Ga flux. The best surface morphology in AFM images was obtained for the flux ratio of 6.6 at 500 °C on GaSb (111)B substrates.

An insulating substrate was desired for the electrical characterization of $Cd_3As_2$. GaSb has a relatively small electrical bandgap and contributes significantly to electrical transport. GaAs has a relatively large electronic bandgap with a zinc blende structure. However, the lattice-mismatch between GaAs and $Cd_3As_2$ is large (∼11%). Therefore, the growth of GaSb on GaAs was developed to reduce the lattice mismatch with sufficient electrical insulation for $Cd_3As_2$ growth.

Films were grown on a 10×10 $mm^2$ size pieces of (111)A GaAs, diced from a 2 inch wafer. Before loading, substrates were chemically etched for five minutes in concentrated HCl to remove the native oxides. Before growth, annealing under Sb flux at 600 °C was done for two minutes to remove the remaining native oxide. Initially, GaSb was grown by using the same optimized conditions (V/III ratio, substrates temperature) described for GaSb on GaSb in the last section.

RHEED was used as an initial check to identify the growth's quality. Figure 2.3 shows pre- and post-growth RHEED with AFM images for GaSb on GaAs. The growth was done for 20 minutes. A streaky RHEED with visible reconstruction indicated the 2D growth of the GaSb layer. The 10×10 $\mu m^2$ size AFM image shows a relatively smooth surface morphology (RMS roughness of 1.34 nm) (Fig.2.3). However, triangular shaped islands were visible in 1×1 $\mu m^2$ size AFM images, indicating island nucleation on the

surface. A study of $Cd_3As_2$ growth is done on this GaSb layer and discussed in the next section.

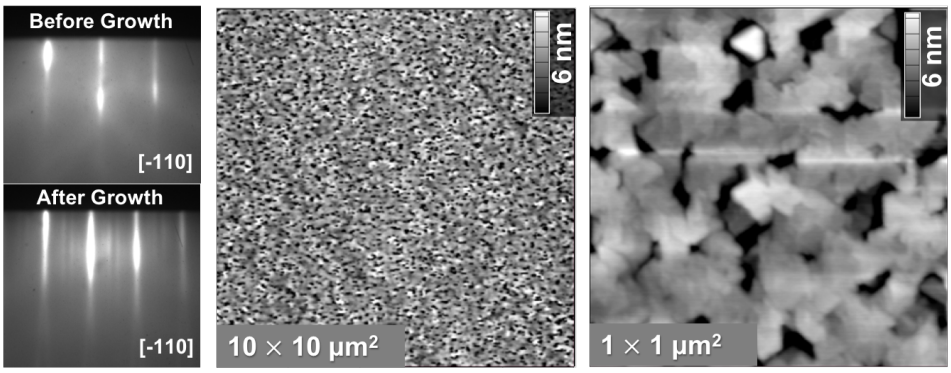


Figure 2.3: RHEED and AFM of the GaSb film grown on on-axis GaAs(111) A substrates.

### Further improvements

Miscut substrates were used to improve the films' quality. $1\times1$ $\mu m^2$ size AFM image shows the triangular shape island indicating the growth in the Volmer-Weber growth mode. These islands are rotated by 180° due to stacking faults in the films and have been observed previously[85]. These crystalline triangles laterally grow in the opposite direction. The next layer atoms preferentially follow the same stacking sequence as the underlying layer and neighbor, resulting in the formation of twin domains in the films. The twin domain boundaries act as a scattering source for the conducting electrons, therefore, degrade the electrical performance of materials [86]. Additionally, the growth by individual islands with stacking fault promotes 3D growth leading to poor surface quality. Miscut substrate has been shown an effective way to suppress the twinning by providing a nucleation site and forcing the growth in the direction of miscut [86, 87, 88]. Moreover, miscut substrates promote the step flow growth that ultimately improves the surface morphology. For further improvement in the films' quality, we switched to miscut substrates for growth.

(111)B GaAs substrates 1° miscut to $< \bar{1}\bar{1}2 >$ were selected for further growth. Additionally, an Sb effusion cell was replaced by an Sb cracker cell to supply Sb. The cracker cell has an additional high-temperature zone that breaks $Sb_4$ molecule to a more reactive $Sb_2$ molecule. The flux ratio was re-optimized again due to a change in the reactivity of antimony molecules. The growth window of the flux ratio was dropped to a lower value of 4.5 at the same growth temperature, indicating the higher reactivity of $Sb_2$ molecules than $Sb_4$. The films were grown by keeping the same oxide removal steps as the previous section. A significant change in the surface's quality was observed by AFM(Fig.2.4). Moreover, a relatively narrow growth window for flux ratio was observed and a slight change in flux ratio leads to a rougher surface with triangular shape features (shown in Fig.2.4).

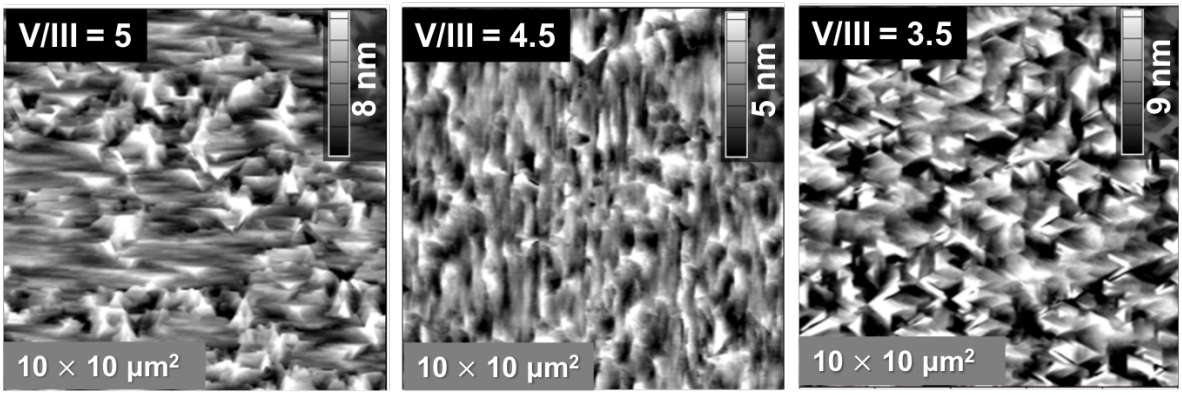


Figure 2.4: AFM of GaSb grown on GaAs (111)A miscut substrate with different V/III flux ratio.

To further improve the growth quality, the oxide removal step was modified. As discussed in the previous part, the native oxides were etched chemically by concentrated HCl for 5 minutes but the exposure of concentrated HCl chemical for a long time (5 minutes in our study) damages the surface[89]. This damaged surface further affects the nucleation and results in a rough surface. One way to bypass this issue is thermal desorp-

tion. However, the thermal desorption at high temperatures also causes the formation of pits on the surface that ultimately affects the surface quality of the films [90, 91]. Atomic hydrogen etching has been shown an effective way to remove native oxide at significantly low temperatures with minimum surface defects [91]. We adopted a similar approach and optimized the surface cleaning by atomic hydrogen. A hydrogen etch at 450 °C substrate temperature under $2\times10^{-6}$ Torr flux was done for an hour. The quality of films grown with different atomic hydrogen etching conditions was compared. An atomically flat surface was obtained when atomic hydrogen etch was combined with chemical etching for 1 minute with diluted HCl (1:1). This short time etching in dilute HCl is less aggressive. Figure 2.5 shows the RHEED and AFM for a GaSb film grown on GaAs by using the optimized oxide removal process. The V/III flux ratio was kept the same as before and the film was grown at a substrate temperature of 480 °C. A sharp streaky RHEED with a reconstruction pattern was obtained after growth. This streaky RHEED indicates 2D growth. Additionally, visible reconstructions lines in RHEED confirmed the 2-dimensionality of the surface. RHEED turned to a streaky pattern in a shorter time (10 seconds) in comparison to previous growth of GaSb. This indicates the growth mode transformed to 2D mode quicker than the previous growth. AFM further confirms the high quality of the films and an atomically smooth surface with RMS roughness of 1.1 nm was observed (Fig.2.5).

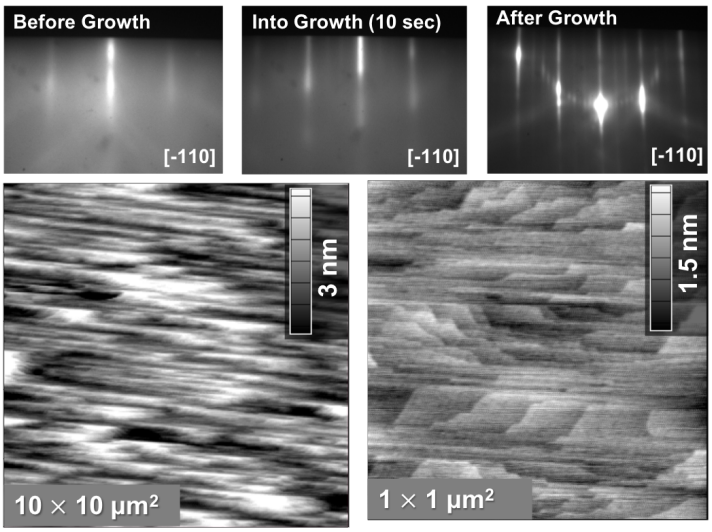


Figure 2.5: RHEED and AFM of GaSb films grown on GaAs (111)B substrates clean with atomic hydrogen and chemical etch.

Pyrometry for monitoring the substrate temperature was modified to improve growth consistency. Block-dependent thermocouple reading was another issue for the temperature reproducibility which led an inconsistency in the growth quality. As mentioned earlier, the temperature was monitored by the thermocouple sitting behind the back of the block. The blocks were chemically etched before every loading. This makes the temperature reading dependent on the block and changes over time as one continues to use the same block. Thus, the growth temperature drifted to a lower value with time. A band-edge pyrometer was installed to overcome this problem and the growth temperature was re-optimized. The optimal growth temperature of 450 °C with a window of ±5 °C was found on the band-edge pyrometer. The growth temperature outside this window produced a rougher surface with triangular shape islands. A narrow growth window for V/III flux ratio (4.5±0.2) was found. The $Cd_3As_2$ growth was continued on GaSb grown on GaAs and discussed in the next section.

### 2.2.3 $Cd_3As_2$ growth on GaSb buffer layers

Growth of $Cd_3As_2$ was developed at the different stages of GaSb growth. GaSb quality shows a great impact on the quality of $Cd_3As_2$ films. The $Cd_3As_2$ growth is divided into two parts; the first part discusses the growth in the early stage of GaSb and the second part discusses the growth of $Cd_3As_2$ on the high-quality GaSb.

#### Preliminary growth

$Cd_3As_2$ growth was investigated by varying the growth conditions including $Cd_3As_2$ molecular flux and substrate temperature. After the growth of *in-situ* GaSb, the substrates were cooled to the $Cd_3As_2$ growth temperature and Sb flux was terminated at 350 °C. $Cd_3As_2$ molecular flux was supplied by evaporating solid pieces of $Cd_3As_2$ in a Knudsen type effusion cell. The growth temperature for $Cd_3As_2$ was found to be relatively low and $Cd_3As_2$ molecular flux dependent. A series of $Cd_3As_2$ films were grown by systematically varying the temperature from 100 °C to 210 °C and $Cd_3As_2$'s flux from $1\times10^{-7}$–$5\times10^{-6}$ Torr. Figure 2.6 shows the after-growth RHEED and AFM for films grown at different temperatures. All the films were grown for an hour. These films were grown on GaSb discussed in the previous section with moderate quality. RHEED for growth temperature below 170 °C showed a spotty pattern indicative of a 3D growth. The films grown at a temperature higher than 170 °C showed a streaky pattern. The AFM images of the film show a rough surface with triangle shape islands for all the films. The island size increase with the growth temperature, indicating the growth shift towards two-dimensional with the increase in growth temperature. The carrier mobilities were compared for the $Cd_3As_2$ films grown at different temperatures (Fig.2.6). High mobility of 19,300 $cm^{-2}V^{-1}s^{-1}$ was observed for the films grown at 210 °C.

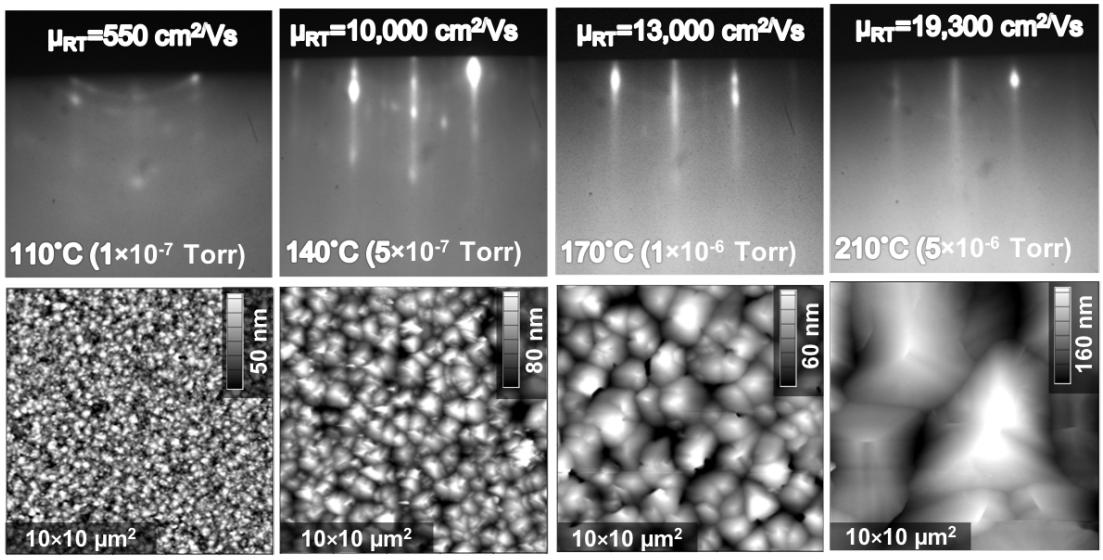


Figure 2.6: RHEED and AFM of $Cd_3As_2$ films grown on GaAs substrates with different substrate temperature and atomic flux.

Further, the growth mechanism and nucleation of $Cd_3As_2$ was studied by monitoring the RHEED during the growth. Figure 2.7 shows RHEED at different growth times during the $Cd_3As_2$ growth. The growth was done at 160 °C substrate temperature under $1\times10^{-6}$ Torr flux. The nucleation started in 30 seconds and the RHEED developed a spotty pattern indicative of 3D nucleation. On further growth, RHEED developed a low-intensity streaky pattern with a spotty pattern on top. This transformation to a streaky pattern is due to increases in island size.

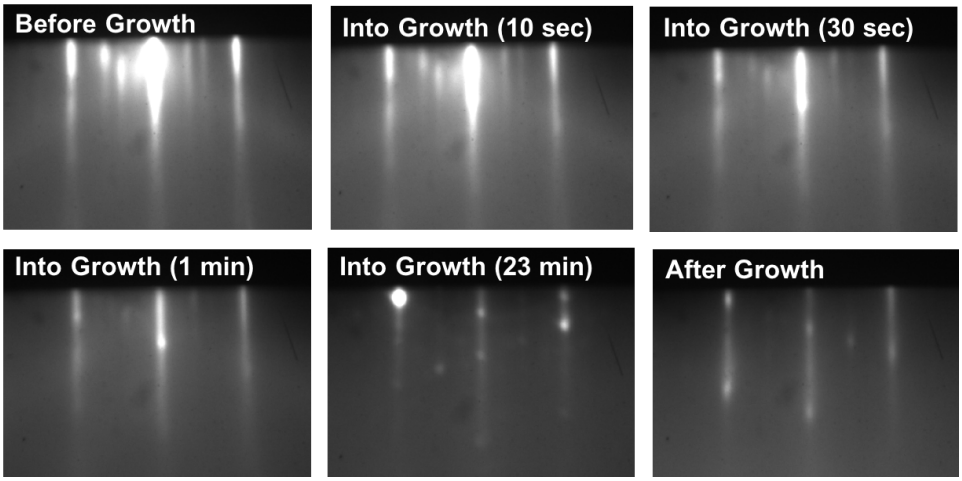


Figure 2.7: RHEED during the growth of $Cd_3As_2$.

RHEED after growth and carrier mobility measurements suggested the improvement in the $Cd_3As_2$ film quality with increasing growth temperature (shown in Fig.2.6). The growth at high temperature was limited by the $Cd_3As_2$ molecular flux supply and greatly affected the nucleation time. Under constant $Cd_3As_2$ molecular flux, the nucleation time increased with increase in the growth temperature and above a certain temperature no growth occurred. A high molecular flux of $Cd_3As_2$ was thus required to push the growth temperatures higher. The films grown at 210 °C substrate temperature (shown in Fig.2.6) needed the molecular flux of $5\times10^{-6}$ Torr and below this flux, there was no growth of $Cd_3As_2$. However, the $Cd_3As_2$ molecular flux is limited by the source material, and the lifetime of $Cd_3As_2$cell decreases with the increase in operating cell temperature. To supply $5\times10^{-6}$ Torr flux, the $Cd_3As_2$cell was heated to 410 °C. This high temperature depleted the cell material and required refilling of the cell. To avoid this, an additional $Cd_3As_2$ effusion cell was installed in the system and a maximum of $1\times10^{-6}$ Torr flux from each cell was fixed for further growth studies.

### Growth of $Cd_3As_2$ on improved GaSb buffer layer

The growth of $Cd_3As_2$ was the studied on the improved GaSb layer. A similar growth study was done by growing a series of $Cd_3As_2$ films by systematically varying the growth temperature. A constant flux of $2\times10^{-6}$ Torr was supplied by two $Cd_3As_2$ effusion cells. A similar growth window for substrate temperature was found as earlier discussed. However, a significant improvement in the film quality and a change in growth mode was observed.

The nucleation during $Cd_3As_2$ growth was studied by RHEED. Figure 2.8 shows the RHEED images during and after the $Cd_3As_2$ growth. The growth was done under $2\times10^{-6}$ Torr $Cd_3As_2$ flux and at 180 °C substrate temperature. The nucleation shows a streaky pattern in RHEED indicating the 2D nucleation of $Cd_3As_2$. A drop in the RHEED intensity was observed during nucleation and the 2D line scan of RHEED showed the instant relaxation of the crystal. On further growth, RHEED gets sharper showing the improvement in the quality of the film. A (2×2) reconstructions were visible in post-growth RHEED. This reconstruction gives another signature of the high-quality 2D surface of $Cd_3As_2$. The nucleation mode is found to be independent of the growth temperature in the range 150 °C to 210 °C, and consistent 2D nucleation of $Cd_3As_2$ was observed. However, the nucleation time depended on the substrate temperature and is discussed further.

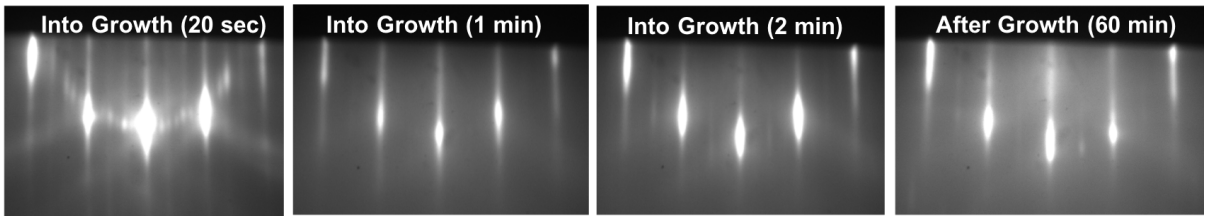


Figure 2.8: RHEED during and after $Cd_3As_2$ growth on improved GaSb buffer layer.

AFM shows a huge improvement in the film surface morphology, consistent with the

RHEED findings. Figure 2.9 shows the 5×5 $\mu m^2$ and 1×1 $\mu m^2$ AFM images for $Cd_3As_2$ films grown at 150 °C under $2\times10^{-6}$ Torr molecular flux. A smooth surface with an RMS roughness of 0.9 nm was observed by AFM. The roughness scale is the same range as the underlying GaSb layer. Atomic steps are visible in 1×1 $\mu m^2$ scale AFM images with the height in the order as a unit cell of $Cd_3As_2$ (shown in Fig.2.9). These AFM images confirmed a high-quality surface morphology of the films.

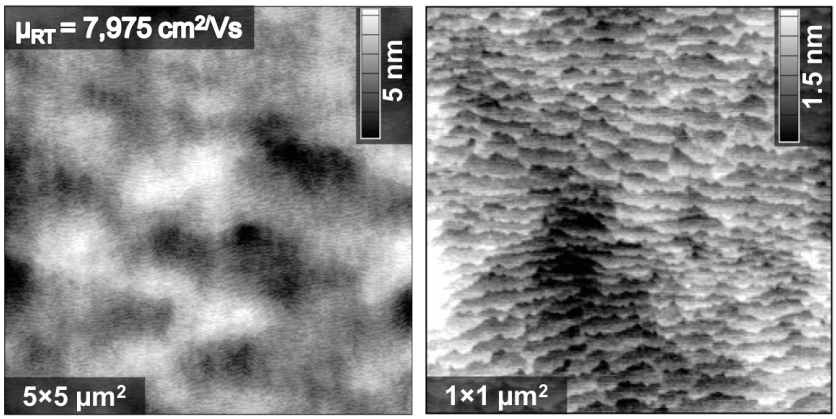


Figure 2.9: RHEED and AFM of $Cd_3As_2$ films grown on improved GaSb buffer layer at 150°C substrate temperature under $2\times10^{-6}$ Torr.

High-resolution x-ray diffraction (HRXRD) measurements were performed to study the crystalline orientation and structural quality of the films. Figure 2.10 shows out-of-plane XRD data for $Cd_3As_2$ film grown for 5 minutes at 150°C substrate temperature. No additional peaks except 111 for GaAs and GaSb, 112 for $Cd_3As_2$ was observed(Fig.2.10a). This confirms the growth of single-phase with single plane oriented $Cd_3As_2$ films. High-resolution out-of-plane XRD data around $Cd_3As_2$ 224 reflection (shown in Fig.2.10b) shows thickness fringes for GaSb and $Cd_3As_2$ reflection peaks. The thickness of 180 nm and 80 nm were calculated for GaSb and $Cd_3As_2$ respectively by fitting these thickness fringes. Based on this thickness, the growth rate for $Cd_3As_2$ is 16 nm/minute. Moreover, these thickness fringes again confirmed the high-quality 2D surface of GaSb and $Cd_3As_2$.

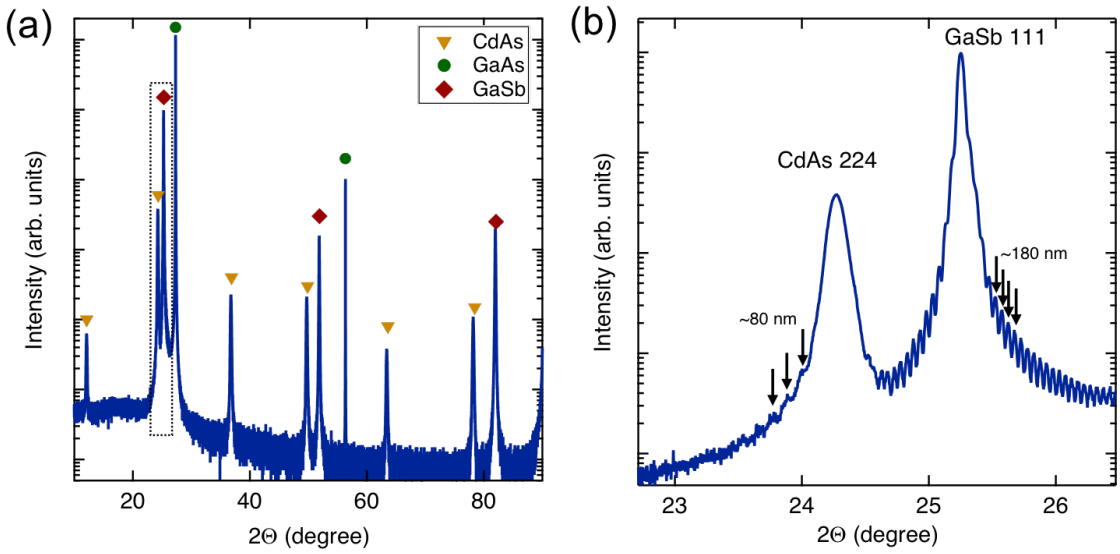


Figure 2.10: Long- and short-range out-of-plane XRD for the $Cd_3As_2$ film grown on GaAs with GaSb buffer layer (Image courtesy of Timo Schumann).

The epitaxial relationship between the GaAs substrates and GaSb and $Cd_3As_2$ layers was confirmed by probing the in-plane alignments by HRXRD measurements. Figure 2.11 shows the phi scan for off-axis GaSb/GaAs 2 2 4 and $Cd_3As_2$ 4 4 16 reflections. Alignment between the in-plane reflection of the substrate (GaAs), buffer (GaSb), and $Cd_3As_2$ peaks was observed. This alignment indicates that $Cd_3As_2$ follows the atomic arrangement as the substrates and can be controlled by the substrate. An additional set of the peaks at the interval of 60° was observed for GaSb and $Cd_3As_2$. These additional peaks represent the twinning in the $Cd_3As_2$ and GaSb films. This twinning is due to the stacking faults. The zinc blende structure has ABCABC stacking along [111] direction. Due to lattice mismatch between GaAs and GaSb that creats the dislocations at the interface and result in stacking fault [85]. Due to these dislocations, the stacking is divided into domains of ABCABC and ACBACBA which are rotated by 180°. These 180° rotated crystals for GaSb have been observed in the AFM images discussed earlier. The rotation of the plane is shown in Fig. 2.11 (b). Because of these rotated domains,

an additional set of peaks is observed in the phi scan indicating the twinning in the films. This twinning can be further addressed by employing a higher degree of miscut substrates. The additional twinning in $Cd_3As_2$ films could not be identified due to a close value of $c/2$ and $a$ that made it difficult to distinguish between 4 4 8, 8 4 8, 4 4 16 peaks.

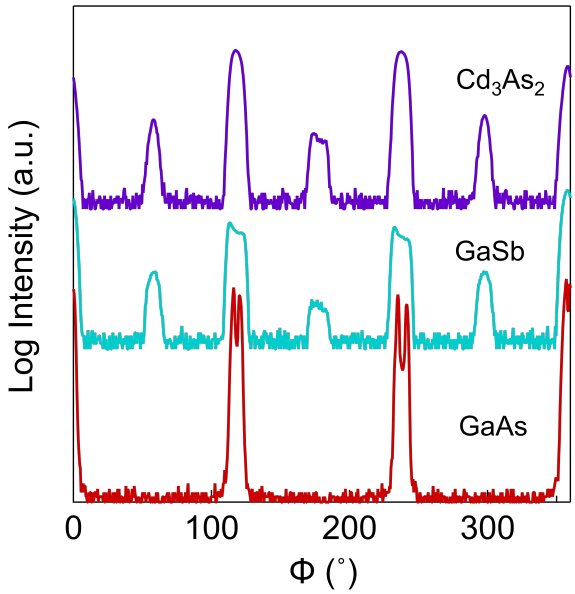


Figure 2.11: In-plane XRD for 4 4 16 $Cd_3As_2$ and 2 2 4 GaSb/GaAs reflections.

STEM images show a sharp interface between the GaSb and $Cd_3As_2$ films indicating the high-quality growth (shown in Fig.2.12a). Cd vacancies were further identified by high angular annular dark-field scanning transmission electron microscopy (HAADF STEM), (Fig.2.12b). This can be seen as an additional intensity drop along the red arrow in comparison to the blue arrow(Fig.2.12b). This ordering of Cd-vacancy matches with vacancy ordering given for low-temperature $Cd_3As_2$ phase (discussed in chapter 1). This finding confirms the growth of $Cd_3As_2$ in a low-temperature Dirac semimetal phase.

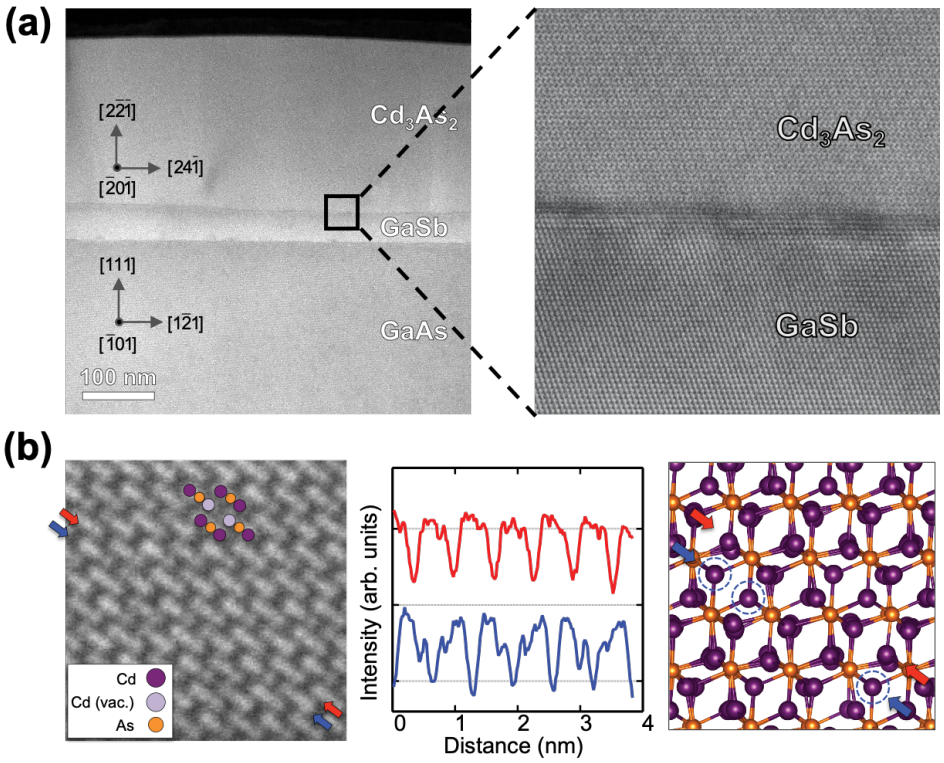


Figure 2.12: HAADF STEM images showing the high-quality interface (a) and vacancy ordering (b) for $Cd_3As_2$ grown on GaAs with the GaSb buffer layer. (Image courtesy of Honggyu Kim).

The nucleation time for $Cd_3As_2$ strongly depends on the substrate temperature. The temperature was monitored by the thermocouple for the growth discussed in the above section, but thermocouple readings are unreliable. Thus, there was not a clear correspondence between the nucleation time and the substrate temperature. To overcome this problem, a low-temperature optical pyrometer was installed for further growth study. This required the substrates to be loaded by gallium bonding. The GaAs substrates are transparent to most of the infrared (IR) radiations: these IR radiations obstruct the measurement of low substrate temperature. The gallium metal layer absorbs the thermal radiation from the heater and transfers the heat through thermal conduction. The growth temperature was calibrated by the nucleation time. For the growth temperature of 135

°C in an optical pyrometer, a 15 seconds nucleation time was observed. A molecular flux of $2\times10^{-6}$ Torr was used for this calibration.

We demonstrated the epitaxial growth of $Cd_3As_2$ on GaSb with high structural and electrical quality. The $Cd_3As_2$ film quality was greatly affected by the buffer layer and showed a huge improvement with improving the buffer layer. The electron mobility was improved from 10,000 $cm^{-2}V^{-1}s^{-1}$ to 20,000 $cm^{-2}V^{-1}s^{-1}$ for the thick films. X-ray studies showed the films are grown single phase with in-plane epitaxial alignment. Further, HAADF-STEM studies confirmed the low-temperature Dirac semimetal phase of the film. The electrical transport from different surface and bulk electronic states of $Cd_3As_2$ was observed and is discussed in chapter 3.

### 2.2.4 Growth of $Cd_3As_2$ on CdTe

In this section, I discuss the growth of $Cd_3As_2$ on CdTe substrates with (111) orientation. The lattice-mismatch between CdTe and $Cd_3As_2$ is $-2.2\%$, slightly lower than the mismatch between GaSb and $Cd_3As_2$. A large bandgap in CdTe provides an insulating substrate for $Cd_3As_2$ that is useful for electrical transport studies.

Initially, the growth study was performed on on-axis CdTe(111)A (Cd polar) substrates. The substrates were loaded on the molybdenum blocks and heated radiatively. A solvent cleaning by isopropanol and acetone were done before loading. Thermocouple readings were used to monitor the substrates' temperatures. An amorphous layer of native oxide on CdTe was observed in RHEED before growth(Fig.2.13) and thermal annealing was done to desorb the oxide. Figure 2.13 shows the evolution of RHEED during oxide desorption at different temperatures. After heating at 300 °C for 10 minutes, a faint streaky RHEED was developed. The intensity of the streaks got sharper at 350 °C after 10 minutes. Upon further heating to 400 °C, RHEED turned to a spotty

pattern indicating that the surface roughens due to thermal desorption. After annealing, the temperature was lowered to the $Cd_3As_2$ growth temperature and a growth study was done by using $2\times10^{-6}$ Torr $Cd_3As_2$ molecular flux in a temperature range of 140 °C-200 °C (same as the study on GaSb substrates).

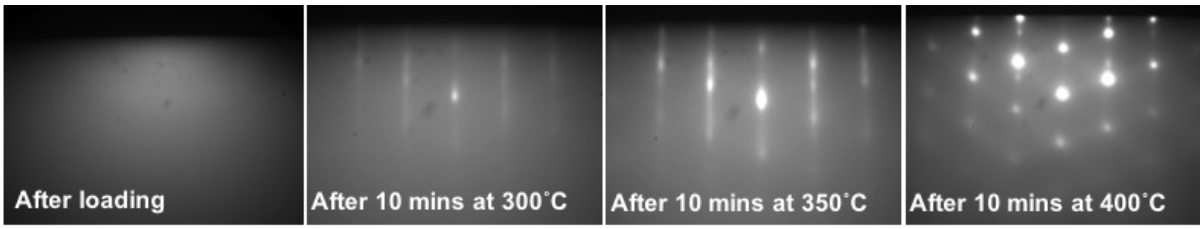


Figure 2.13: RHEED of CdTe substrates after loading and at different temperature during oxide desorption.

The growth of $Cd_3As_2$ was done at 170 °C for 30 minutes with $2\times10^{-6}$ Torr $Cd_3As_2$ molecular flux. The growth temperature for $Cd_3As_2$ is calibrated by the nucleation time. For 170 °C growth temperature, the nucleation took more than a minute to start depositing. The nucleation time of $Cd_3As_2$ is longer on CdTe substrates in comparison to GaSb substrates. Because this growth study is done by using the thermocouple temperature, a direct comparison between nucleation time on GaSb and CdTe can not be made. During $Cd_3As_2$ growth, RHEED developed a streaky pattern indicating 2D growth of $Cd_3As_2$. RHEED after growth of $Cd_3As_2$ is streaky with similar reconstruction to growth on GaSb (Shown in Fig. 2.14). AFM after growth shows the individual islands of $Cd_3As_2$ (Fig. 2.14). As mentioned earlier, these individual islands give stacking faults in the films and introduce structural defects such as twinning in the films.

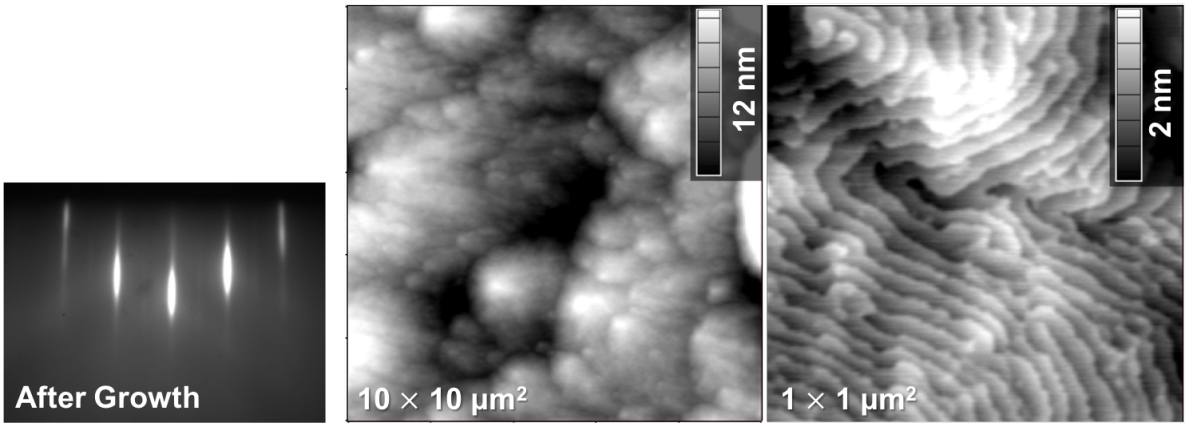


Figure 2.14: RHEED and AFM of $Cd_3As_2$ film grown on on-axis CdTe (111)B substrate.

The epitaxial relation between $Cd_3As_2$ films and CdTe was verified by conducting in-plane XRD measurement. Figure 2.15 shows the in-plane XRD for 4 4 16 and 2 2 4 reflections of $Cd_3As_2$ and CdTe, respectively. An alignment between the in-plane reflections peaks of $Cd_3As_2$ and CdTe was observed with an expected 3-fold symmetry. This sharp alignment confirmed an epitaxial relation between the films and substrates and further confirm the suitability of CdTe substrates for $Cd_3As_2$ epitaxy. However, an additional set of peaks at a 60° interval was observed for $Cd_3As_2$ that indicates the twinning in the films. To address this issue, further growth study on 4° miscut towards $< \bar{1}\bar{1}2 >$ CdTe (111)A (Cd polar) substrates was done. The miscut direction is the same as GaAs substrates but with a higher angle.

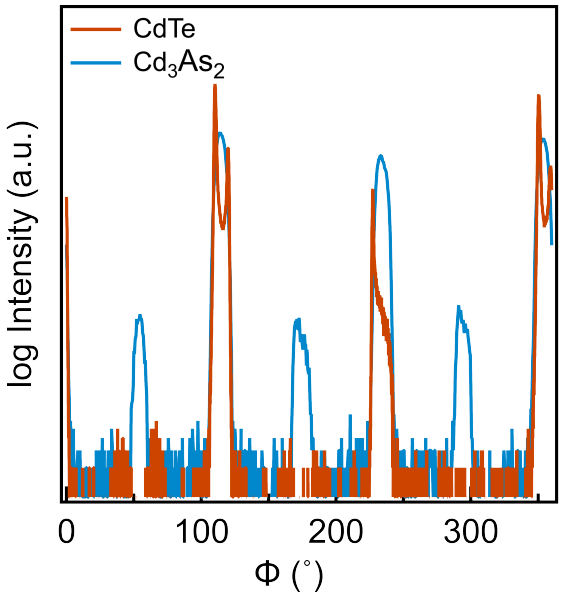


Figure 2.15: In-plane XRD for $Cd_3As_2$ grown on on-axis CdTe substrate.

Modification in the native oxide removal step is required to further improve the film's quality. As shown in the previous section, the underlying substrate has a major impact on $Cd_3As_2$ film growth quality. Thermal annealing for CdTe substrates at high temperatures produced a rough surface, observed in RHEED as a spotty pattern (Fig.2.13). It is important to remove the oxide completely. When a relatively low temperature for annealing was used and the RHEED similar to 350 °C in Fig.2.13 was obtained, there was no growth of $Cd_3As_2$ due to remaining oxide on the surface. Thus, finding the surface treatment procedure with minimum damage is essential.

We developed the oxide removal process by combing the chemical etch with atomic hydrogen. The etching process depends on the surface bonding and therefore, sensitive to the polarity of the surface (Cd or Te polar). Thus, this process is optimized for (111)A CdTe substrates and $Cd_3As_2$ growth was continued for this polarity. Atomic hydrogen etching has been shown an effective way to remove native oxide for (001) CdTe and (110)

CdTe at low temperatures[92]. For our case of (111) orientation, an optimal process was developed by using 0.2% bromine methanol for 20 seconds before loading followed by atomic hydrogen etch at 350 °C for 30 minutes. Figure 2.16 (a) shows the RHEED after oxide removal of CdTe substrates. A sharp streaky RHEED with visible reconstructions was observed, indicating the high quality of CdTe surface after oxide removal.

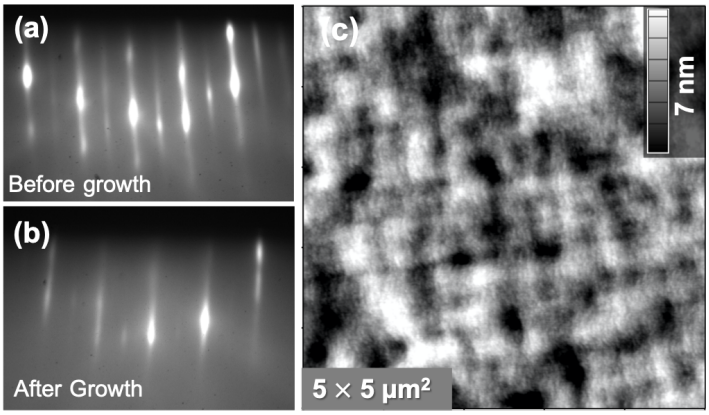


Figure 2.16: (a) RHEED of CdTe after oxide removal by atomic hydrogen and chemical etching. (b) RHEED and AFM (c) after $Cd_3As_2$ growth on 4° miscut CdTe (111)A substrate.

$Cd_3As_2$ growth was further developed on these high-quality substrates. The nucleation mechanism was unchanged and a streaky RHEED with reconstruction was observed. AFM shows a smooth surface morphology with $Cd_3As_2$ films steps growing in the miscut directions (Fig.2.17 (c)). The RMS roughness (1.8 nm) of the films is slightly higher than the films grown on GaAs substrates. This can be further improved by growing an *in-situ* buffer layer before $Cd_3As_2$ growth.

In-plane XRD measurements were done to check the twinning in the films. Figure 2.17)(a) shows the in-plane XRD and confirms no twinning in the $Cd_3As_2$ films with an in-plane alignment between CdTe and $Cd_3As_2$ (Fig. 2.17)(a). A sharp interface between the substrate and films is observed indicating the high quality of the films (Fig. 2.17)(b). Again a similar vacancy ordering for Cd was observed, verifying the low-temperature

Dirac semimetal phase growth for the $Cd_3As_2$.

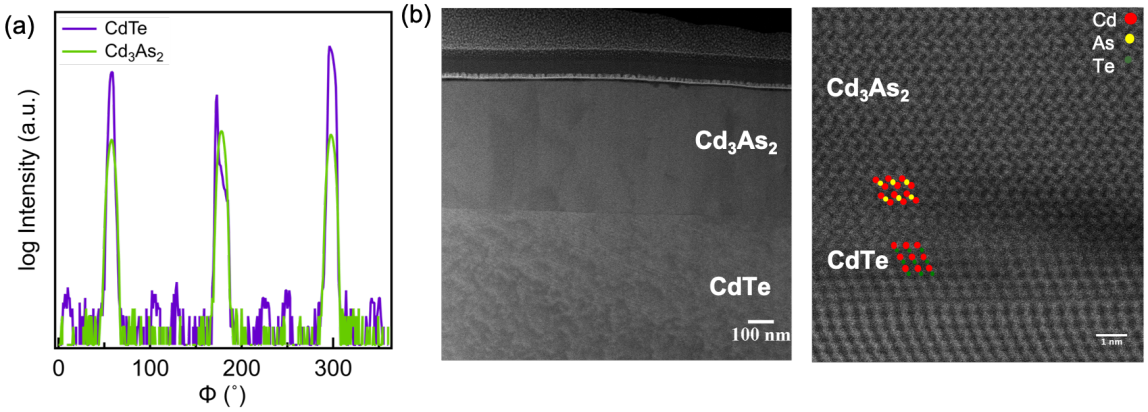


Figure 2.17: In-plane XRD (a) and HAADF-STEM (b) images for $Cd_3As_2$ grown on 4° miscut (111)A CdTe substrate.

This study shows that the epitaxial growth of $Cd_3As_2$ on CdTe can be realized. The films are grown in a low-temperature Dirac semimetal phase with high structural quality. The electrical transport is discussed in chapter 3.

### 2.2.5 Comparison of the growth of $Cd_3As_2$ on GaSb and CdTe

$Cd_3As_2$ growth strongly depends on the substrate quality. The films grow epitaxially on GaSb and CdTe substrates with the same nucleation mechanism. The carrier transport in the films grown on GaSb and CdTe were in the same range for similar film thickness. To further improve the structural quality, a lattice-matched buffer layers were developed.

## 2.3 Growth of $Cd_3As_2$ on lattice-matched alloy

The lattice-matched buffer layers were developed to further improve the $Cd_3As_2$ film's quality and strain study. Strain proportional to lattice-mismatch is induced for heteroepitaxy and when the film is thicker than a critical thickness, the strain relaxation occurs

by the generation of misfit dislocations. In this case, the growth occurs in Stranski-Krastanov (SK) mode: First, a 2D layer by layer growth occurs up to the critical thickness of the films that is later followed by three-dimensional islands growth to relieve the strain. 3D island growth produce a rough surface [93]. Surface roughness and misfit dislocations act as a scattering source for the conducting electrons and limits the carrier mobility that ultimately affects the device performance.

In our growth study on (111)-oriented lattice-mismatched substrates, the RHEED intensity drops during the nucleation. However, it remained streaky during nucleation and after growth. 2D line scan of RHEED during the growth on GaSb and as well as on CdTe showed an instant relaxation of $Cd_3As_2$ films. This instant relaxation is due to large lattice mismatch. The epitaxial growth done on GaSb showed a significant impact of substrate quality on the $Cd_3As_2$ structural quality of the films. Thus, growing the lattice-matched buffer layer was the next step to further improve the film quality. Additionally, this lattice-matched layer provides a platform for strain study.

### 2.3.1 Growth of $Cd_3As_2$ on lattice-matched buffer layer along (111)

#### Growth of lattice-matched $In_xGa_{(1-x)}Sb$ alloy

Lattice-matched layer along (111) orientation was obtained by alloying GaSb and InSb. Growth along (111) for this alloy composition is not well-developed. Thus, growth for this alloy is first developed for $Cd_3As_2$ growth study. The alloy composition $x$ is calculated from Vegard's law applicable to this case:

$$a_{Cd_3As_2} = x \times a_{InSb} + (1 - x) \times a_{GaSb},$$

where $a_{InSb}$ and $a_{GaSb}$ are the lattice constants for InSb and GaSb. For $Cd_3As_2$, the lattice parameter for the pseudocubic unit cell was used is 6.33 Å. By using the above equation, the value of $x$ is calculated 0.7.

The growth study was done on semi-insulating (111)B GaAs substrates. The native oxide was removed by chemical etch and atomic hydrogen etch, discussed earlier, and then loaded on molybdenum blocks by gallium bonding. An optical pyrometer was used to monitor the growth of III-V alloy and $Cd_3As_2$. Before growth, samples were heated under $5\times10^{-7}$ Torr Sb flux for 10 minutes to remove remaining oxides. Initially, the growths were compared on various miscut substrates along with different crystallographic directions by using the group V/III flux ratio of 4 (similar to GaSb growth). 3° miscut towards $< \bar{1}\bar{1}2 >$ substrate produced the best surface morphology and further growth is developed on these substrates.

Growth temperature and group III/V flux ratio was optimized for the best structural quality of the films. All the films were grown for an hour. The flux ratio was varied from 3 to 5 with substrate temperature from 330 °C to 380 °C. In this growth parameters range, a sharp streaky RHEED was obtained with visible reconstruction (2×). Surface morphology, studied by AFM, showed a step bunching along the miscut direction with an RMS roughness of 2 nm. This step bunching became more pronounced for higher temperature growth (> 380 °C) and flux ratio (>4) resulting in a rough surface. Moreover in this growth range, a large number of micro-size defects were observed in an optical microscope. To optimize the best growth parameters, the optical microscope in bright field and dark field image were compared to get a minimum number of defects. Substrate temperature of 360 °C with group V/III flux ratio of 3 produced a minimum number of defects. Figure 2.18 shows the RHEED and AFM image for $In_{0.7}Ga_{0.3}Sb$ film grown with a flux ratio of 3 and a substrate temperature of 360 °C for an hour. A streaky RHEED with visible reconstruction was observed with a relatively smooth surface. The $Cd_3As_2$

growth study was done on this buffer layer.

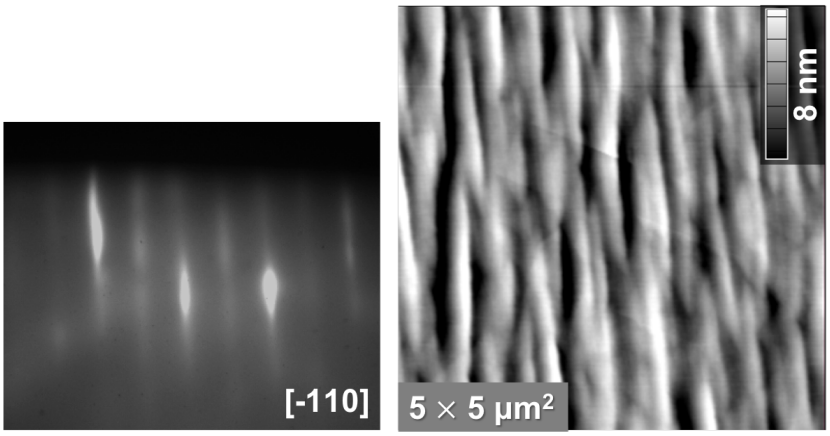


Figure 2.18: RHEED and AFM for the $In_{0.7}Ga_{0.3}Sb$ grown for an hour.

### Growth of $Cd_3As_2$ on lattice matched $In_xGa_{(1-x)}Sb$ alloy

Growth of $Cd_3As_2$ is studied on the lattice-matched InGaSb buffer layer. After InGaSb growth, Sb was turned off along with group III molecular flux and the substrate was cooled down to $Cd_3As_2$ growth temperature. All growths were carried out using $Cd_3As_2$ molecular beam flux of $2\times10^{-6}$ Torr, similar to the previous study. Growth temperature for $Cd_3As_2$ was calibrated by the nucleation time, as discussed for $Cd_3As_2$ on GaSb, and a similar behavior between nucleation time and $Cd_3As_2$growth temperature was observed. The nucleation time of 20 seconds for 135 °C substrate temperature was observed, and increased with substrates temperatures. On further increase in growth temperature above 140 °C, the growth transformed to a 3D growth mode with nucleation time more than a few minutes. For further study, the growth of $Cd_3As_2$ was carried out at 135 °C.

Figure 2.19 shows the RHEED, AFM and HAADF STEM images for a $Cd_3As_2$ films grown at 135 °C for 100 seconds. The growth mechanism remains unchanged and RHEED

during growth shows a drop in intensity while remaining streaky (Fig.2.19). A streaky RHEED with visible reconstruction was obtained after $Cd_3As_2$ growth. AFM shows the growth of layers along the miscut direction with the RMS (2.7 nm) roughness. This roughness scale is in the same range as the underlying buffer layer. HAADF STEM images shows a clean and abrupt interface between InGaSb and $Cd_3As_2$ layers(Fig.2.19). Cd-vacancy ordering was observed for $Cd_3As_2$ indicating the growth of the low-temperature Dirac semimetal phase. $Cd_3As_2$ films grown on lattice-matched InGaSb shows the carrier mobility in the same range as the films grown on GaSb and CdTe substrates.

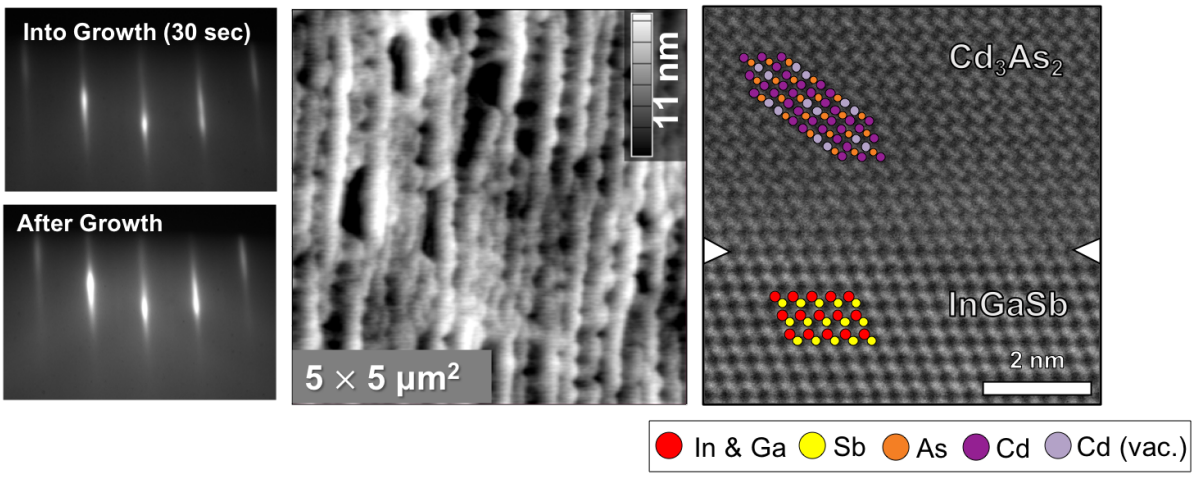


Figure 2.19: RHEED, AFM and STEM images for $Cd_3As_2$ grown on lattice matched $In_{0.7}Ga_{0.3}Sb$ buffer layer.

### 2.3.2 Growth of $Cd_3As_2$ on lattice-matched buffer layer along (001)

#### Growht of lattice-matched $Al_xIn_{(1-x)}Sb$ alloy

In this section, the growth of a (001)-oriented lattice-matched buffer layer is discussed. The growth of $Al_xIn_{(1-x)}Sb$ alloy is selected for this study. $Cd_3As_2$ has a tetragonal unit cell and has been shown to grow along (001) previously from our group[94]. The

in-plane lattice parameter of $Cd_3As_2$ (a = 6.315 Å) was used to calculate the alloy composition. The calculation was done by using Vegard's law and the composition for lattice-matched alloy was found to be 47% aluminum with the remaining indium. AlInSb alloy near this desired composition has been studied extensively in past for InSb quantum wells[95, 96, 97, 98, 99, 100, 101]. This composition has a relatively wide electrical bandgap that provides electrical insulation between GaSb and $Cd_3As_2$ film.

The films were grown on small pieces of $10\times10$ mm$^2$ chips cleaved from a 2-inch undoped (001) GaSb wafer. Substrates were loaded by gallium bonding on molybdenum blocks and the temperature was monitored by an optical pyrometer. Before growth, thermal annealing under $3.3\times10^{-7}$ Torr of Sb molecular flux was done to desorb the native oxides. This oxide desorption for GaSb occurs at 540 °C and is used for calibration for thermometry[102]. Oxide desorption was monitored by RHEED and pyrometer temperature value was noted to standardize and calibrate the optical pyrometer. At this oxide desorption temperature, RHEED quickly developed a spotty pattern. The pyrometer value for this desorption was 500 °C, a slightly lower than the reported value. Substrates were annealed for 15 minutes at this temperature. After the oxide desorption, the substrate temperature was lowered by 10 °C in thermocouple reading and a 80 nm thick GaSb layer was grown to provides a smooth surface for alloy growth.

After the GaSb growth, the substrate temperature was lowered to the AlInSb growth temperature under Sb flux. As mentioned earlier, due to the small growth window, antimonides are grown with a low V/III ratio, therefore, the growth window was investigated with a small V/III flux ratio (1-2). The Sb flux of $4\times10^{-7}$ Torr is used to grow the alloy with group III flux by keeping the flux ratio close under 2. This flux ratio is close to unity when calculated from actual molecular flux measured form RHEED oscillations. The flux of Al and In for lattice matched composition was calculated by the RHEED oscillations and corresponding BFM values were used to grow the alloy. Further, the

out-of-plane XRD measurements were used to confirm and re-optimize these BFM values for lattice-matched alloy compositions.

Surface reconstructions were used to optimize the growth temperature. Usually, a transition in surface reconstruction under Sb rich conditions is used to identify the real temperature with high accuracy. For InSb, the surface reconstruction changes from (4×4) to a(1×3) at 390 °C[103]. For the best quality, indium based antimonides are grown just above this transition temperature by maintaining the (1×3). For AlSb this transition to (1×3) occurs at a temperature of 410 °C[104] and in the case of an AlInSb alloy with 9% Al, the (1×3) is obtained at $T_{tr(InSb)}$+20 °C[96], which is same as transition temperature for AlSb. In this study, the temperature was selected to get the (1×3) reconstructions. An initial estimate for the growth was obtained from GaSb oxide desorption, which occurs at 540 °C[102]. However, In our growth study, this oxide desorption occurred at 500 °C. Thus a 40°C offset was used for the initial estimate of growth temperature. A series of samples with temperatures from 360 °C to 390 °C were grown with the same group III (Al and In) molecular flux and Sb flux ranging from $4\times10^{-7}$ Torr (360 °C-380 °C) to $5\times10^{-7}$ Torr (390 °C). A (1×3) reconstruction was observed for this temperature range indicating the growth temperature is higher than the transition temperature ( 410 °C). Fig.2.20 shows the RHEED after growth and AFM of the films grown at 380 °C. RHEED shows a sharp streaky pattern with (1×3) reconstruction. AFM shows the growth of 3D islands with the RMS roughness of 2.4 nm. Moreover, for the growth temperature range from 360 °C to 390 °C, there is no significant change in surface morphology and roughness.

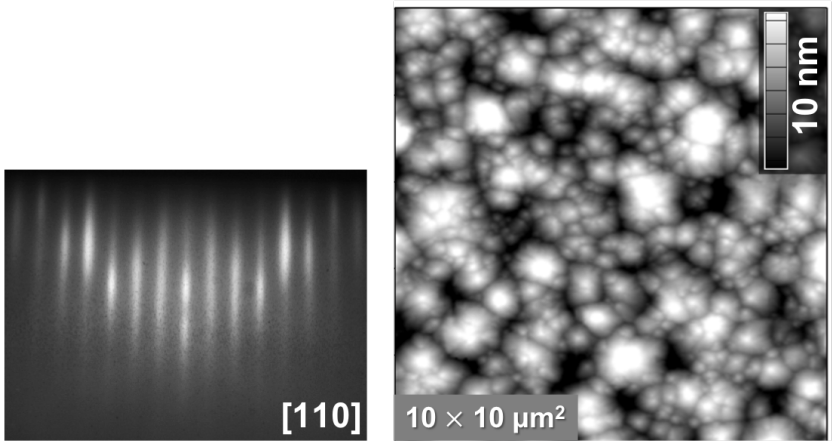


Figure 2.20: RHEED and AFM for the $Al_{0.4}In_{0.6}Sb$ grown at 380 °C for one hour.

Further, a growth study with different group V/III flux ratios was conducted to explore the growth window. A growth with different Sb flux while keeping the group III flux the same was done. Figure 2.21 shows the RHEED and AFM for the buffer layer grown under different Sb beam fluxes. All of these films were grown at 370 °C for one hour.

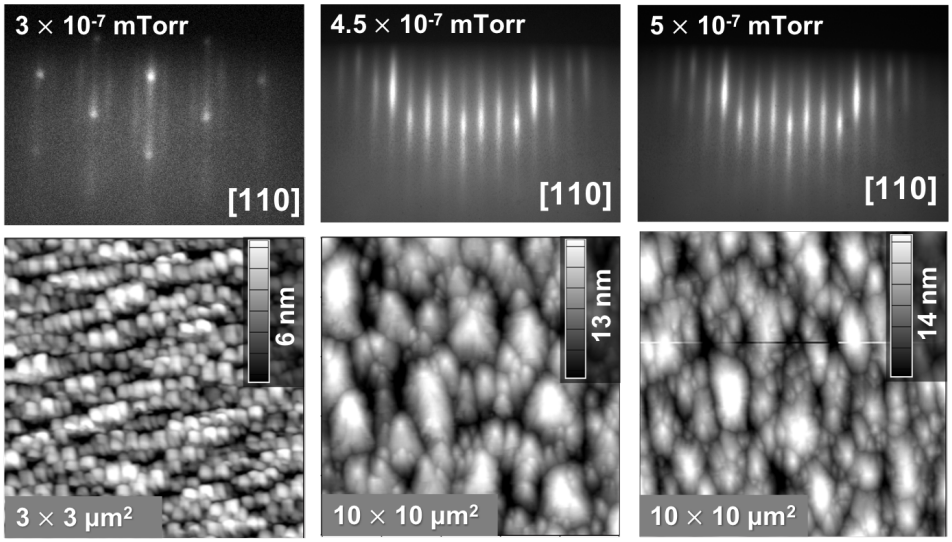


Figure 2.21: RHEED and AFM for the $Al_{0.4}In_{0.6}Sb$ grown with different molecular flux of Sb.

The growth is found to be very sensitive to the Sb flux. For the lower Sb flux, RHEED showed a group III rich reconstruction with a spotty and streaky pattern. AFM showed the growth of square shape crystals indicating the III/V flux ratio to be less than one. The 10×10 $\mu m^2$ image for this growth shows droplets, indicating an excess of group III elements. For higher Sb flux of $5\times10^{-7}$ Torr, surface morphology and surface reconstructions were unchanged. However, the RMS roughness of the films increased slightly from 3.1 to 3.4 nm when Sb is increased from $4.5\times10^{-7}$ Torr to $5\times10^{-7}$ Torr. Moreover, this RMS roughness is higher than the previous growth done with $4\times10^{-7}$ Torr at 370 °C. Therefore, the study was continued with the films grown at 370 °C by using the Sb flux of $4\times10^{-7}$ Torr.

To further improve the surface morphology, substrates with a 3° miscut towards (111)B were used. Miscut substrates had been shown to improve the surface morphology significantly. The films were grown using the same optimized growth parameters as on-axis substrates and, as expected, a (1×3) reconstruction pattern was obtained for the post-growth RHEED.

To further improve the crystalline quality, the growth temperature for the buffer layer was pushed to a higher value by keeping other parameters constant. The quality of the buffer layer was measured by the 004 reflection peak broadening in the out-of-plane XRD data. For this study, a very thick layer of 2.2 $\mu$m AlInSb were grown at different temperature and XRD data was compared for the structural quality (Fig.2.22). As shown in Fig.2.22, the AlInSb 004 reflection peak got narrower with the growth temperature of 410 °C and got broader on further increase in the temperature. An optimized growth temperature of 410 °C was thus found. AFM of the film grown at 410 °C shows a relatively smooth surface morphology with visible atomic steps. However, the RMS roughness scale for 10×10 $\mu m^2$ remains in the same range as the films grown at lower temperature.

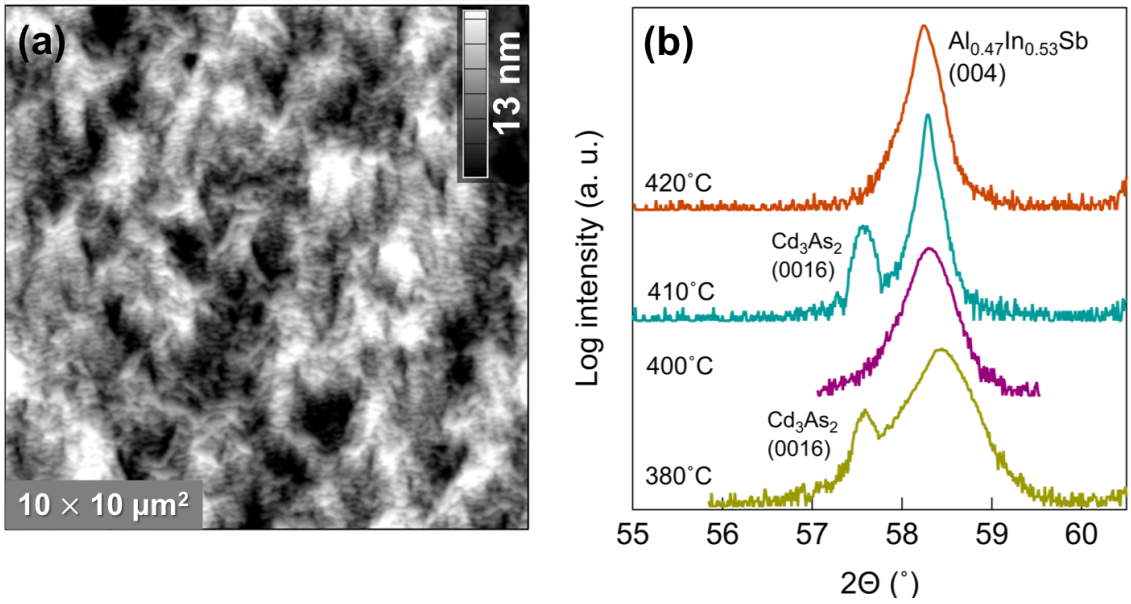


Figure 2.22: (a).AFM for the $Al_{0.4}In_{0.6}Sb$ layer grown at 410 °C. (b) out-of-plane XRD for $Al_{0.4}In_{0.6}Sb$ grown at different substrate temperatures.

### Growth of $Cd_3As_2$ on lattice matched $Al_xIn_{(1-x)}Sb$ buffer layer

$Cd_3As_2$ was grown by using a molecular flux of $2\times10^{-6}$ Torr flux. The optical pyrometer was used to monitor the substrate temperature and the film was grown at 125 °C. Figure 2.23 shows RHEED images during and after the growth of $Cd_3As_2$, and RHEED intensity scans during growth. During nucleation, the RHEED intensity dropped and the RHEED turned to a spotty pattern, indicating the 3D nucleation of $Cd_3As_2$. As the growth continues, this RHEED transformed into a low-intensity streaky pattern. Due to the growth from an individual small island, the surface roughness did not change significantly for the $Cd_3As_2$ films. $Cd_3As_2$ films follow similar surface features like the buffer. AFM images of $Cd_3As_2$ grown on different buffer layers are shown and compared in the next chapter on dislocation study. The carrier transport is discussed in the next chapter with different structure of buffer layers for dislocations study.

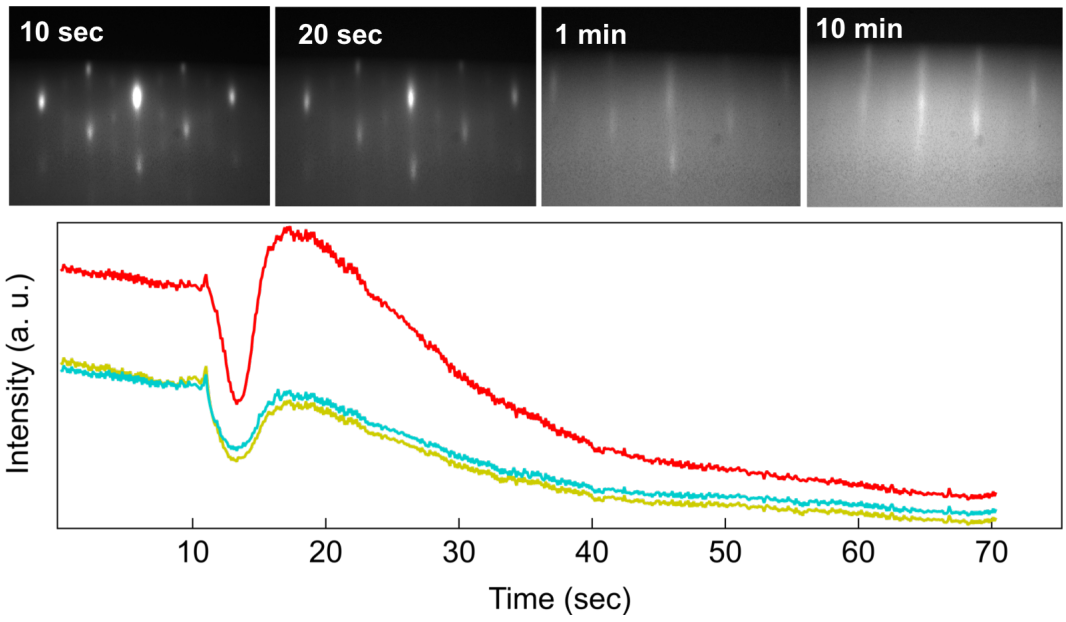


Figure 2.23: RHEED and intensity scan during and after $Cd_3As_2$'s growth

# Chapter 3

# Structural and transport improvement

In this chapter, I discuss the different approaches we developed to improve the structural and electrical quality of $Cd_3As_2$ films. Structural quality was improved by careful design of the lattice-matched buffer layers and their effect on carrier transport is discussed. In the next section, I discuss the low-temperature growth of an *in-situ* GaSb capping layer. This capping layer is needed to protect the top surface from air exposure and processing steps.

## 3.1 Dislocation filtering

Growth and proper design of the buffer layer is important to improve the electrical and structural quality of the films. In this study, we developed the growth of lattice-matched $Al_xIn_{(1-x)}Sb$ and $In_xGa_{(1-x)}Sb$ alloys for (001) and (111) orientations, respectively. Figure 3.1 shows the cross-sectional scanning transmission electron microscope (STEM) image of the interface of (001)-oriented $Al_{0.5}In_{0.5}Sb$ alloy grown on GaSb. A

large number of dislocations were observed originating at the interface. Most of these dislocations align vertically and propagate through the buffer layer. These dislocations can potentially enter the $Cd_3As_2$ film. However, because of the different crystal symmetries and slip systems of $Cd_3As_2$ and the buffers it is not actually known which dislocations can enter the $Cd_3As_2$ layer. The dislocations are a major source of carrier scattering and therefore, degrade the carrier mobility. Low carrier mobility in the films obscures quantum transport and degrades device performance. Therefore, a carefully designed buffer layer is needed to stop these dislocations from entering the $Cd_3As_2$.

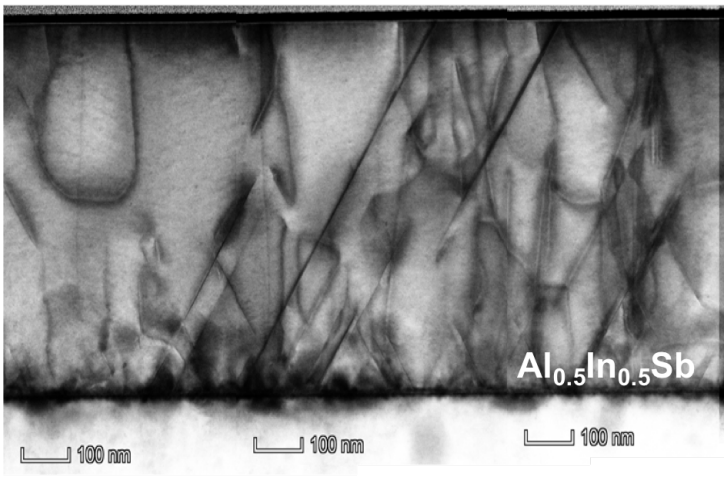


Figure 3.1: Scanning transmission electron micrograph (STEM) of $Al_{0.5}In_{0.5}Sb$ layer grown on (001) GaSb (Image courtesy of Salva Salmani-Rezaie).

The dislocation study provides a platform to understand the effects of structural defects on 3D Dirac electrons. So far, very little is known about the effect of defects on Dirac materials and there is no experimental study for 3D Dirac semimetals in this regard. As discussed in chapter 1, the dislocations act as a short-range scattering source that is dominated by large-angle scattering. However, the Dirac electrons are immune to backscattering due to their chiral nature, therefore, Hall mobility should not be affected by this mechanism. A theoretical study predicts chiral modes hosted by dislocations in

Dirac materials[105]. Thus, a careful dislocation study would clarify the role of these dislocations on electrical transport in 3D Dirac semimetals and would be helpful in identifying the mechanism limiting the electrical transport.

Different heterostructures of buffer layers were designed and compared for their effectiveness in filtering dislocations. Superlattice structures with different nucleation layers or/and strained layers have been shown as an effective way to filter the threading dislocations originating due to misfit [98, 106]. We adopted the strained layer approach, in which an interlayer with a slightly different lattice constant relative to the lattice-matched layer is introduced, to filter dislocations. The strain due to a slightly different lattice constant in the interlayers bends the threading dislocation towards the in-plane direction. This bending increases the annihilation reaction between dislocations or pushes them towards the edge of the films. As a result, this mechanism stops the threading dislocation going through the films. The difference in the in-plane lattice constants of $Cd_3As_2$ and InSb is small, thus a buffer layer that effectively filters dislocations for InSb is expected to due the same for $Cd_3As_2$. There have been numerous studies done on the growth of $Al_xIn_{(1-x)}Sb$ to reduce the dislocation density for InSb quantum wells [99, 107, 100, 108]. Interlayers of $Al_xIn_{(1-x)}Sb$/ $Al_yIn_{(1-y)}Sb$ are introduced with a slight difference in $x$ and $y$. The difference in the values of $x$ and $y$ determines the thickness of the interlayers, as given by Matthews and Blakeslee[109]. For $Cd_3As_2$ growth, we adopted a similar approach in which a total number of 2 strained-layer superlattices (SLS) were grown. For simplicity this buffer layer structure is referred to as Type I. For comparison with a filtering mechanism, a thick buffer layer with a total thickness of structure 1 is grown. And for the 3rd structure, a thin single buffer layer with a single structure is grown. This buffer layer is grown to have high dislocation density in $Cd_3As_2$ films in order to identify the carrier mobility limiting mechanism in $Cd_3As_2$ films.

## 3.2 Growth of $Cd_3As_2$ on different buffer layer structures

The buffer layer structures mentioned in the previous section were grown. Growth conditions such as substrates temperature and group III flux for the $Al_xIn_{(1-x)}Sb$ alloy were the same for all intermediate layers, as discussed in chapter 2. Figure 3.2(a) shows a schematic of the two structures for the buffer layer. For the Type I buffer layer structure, a 520 nm $Al_{0.37}In_{0.63}Sb$ layer was first grown on GaSb. Then a 290 nm $Al_{0.50}In_{0.50}Sb$ layer was grown, followed by another 300 nm $Al_{0.37}In_{0.63}Sb$ layer. These last two layers are referred to together as one filtering layer. In total, two of such filtering layers were grown. Next, a 310 nm $Al_{0.47}In_{0.53}Sb$ layer was grown on the two filtering layers. This layer is lattice-matched to the final $Cd_3As_2$ film. For all subsequent discussion, I will refer to this structure as the Type I buffer layer. In the second type of buffer layer structure, only a single $\sim$2.2 $\mu$m thick lattice-matched $Al_{0.47}In_{0.53}Sb$ layer was grown. Accordingly, this design will be referred to as a Type II buffer layer. For the third structure, a 520 nm lattice-matched $Al_{0.47}In_{0.53}Sb$ was grown. $Cd_3As_2$ films with two different thickness ranges, thick (210–250 nm) and thin (45 nm), were grown on these three buffer layer structures. All the $Cd_3As_2$ films were grown at a substrate temperature of 125 °C. Figure 3.2(b) shows XRD results of thick $Cd_3As_2$ grown on two different buffer layers. The out-of-plane ($c$) lattice constant of $Cd_3As_2$ was calculated to be 25.5 Å, which is slightly larger than the literature value. However, the lattice constants of $Cd_3As_2$ have been reported in a wide range ($a$ = 12.6-12.7 Å, $c$= 25.4-24.5 Å) [10, 9, 12].

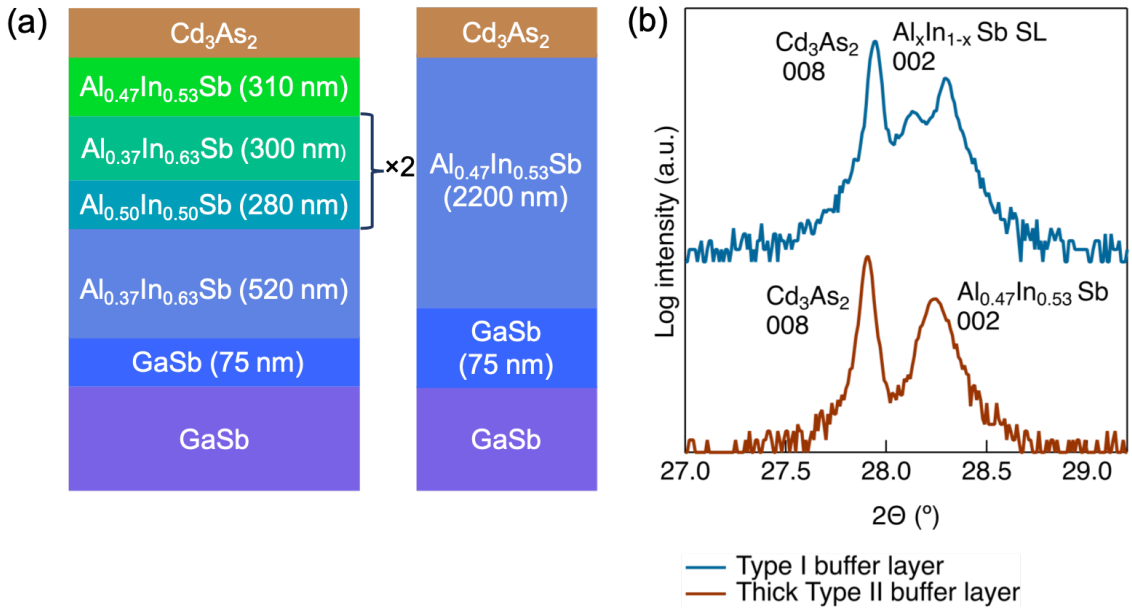


Figure 3.2: (a) Schematic of samples grown on different buffer layer structures described in the text. (b) Out-of-plane $2\theta - \omega$ XRD scans for 004 and 002 reflections for $Cd_3As_2$ and $Al_xIn_{(1-x)}Sb$ layer (layers) respectively.

Figure 3.3 shows AFM images for thick (210–250 nm) $Cd_3As_2$ films grown on the three different buffer layer structures. The underlying buffer layer strongly affects the surface morphology of $Cd_3As_2$ and the RMS roughness is on the same scale as the buffer layer. RMS surface roughness of thick (210–250 nm) $Cd_3As_2$ films grown on these buffer layers were measured to be 5.6 nm (thick Type II buffer layer), 5.2 nm (Type I buffer layer), and 1.8 nm (thin Type II buffer layer). The thin films of $Cd_3As_2$ grown on these buffer layers show similar trends in the surface roughness, i.e. the surface roughness was 4.9 nm on a Type I buffer layer and 1.5 nm on a thin Type II buffer layer.

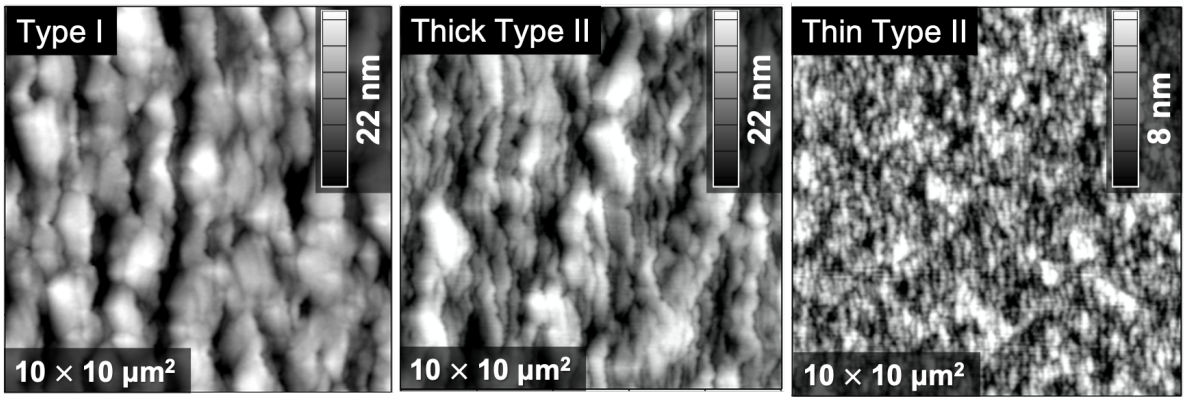


Figure 3.3: AFM for the $Cd_3As_2$ films grown on different buffer layers.

## 3.3 Dislocation study

We used diffraction contrast STEM to study the dislocation density of $Cd_3As_2$ films grown on different buffer layers. Compared to conventional TEM, diffraction contrast STEM can provide sharp and uniform defect contrast with negligible background contrast features, such as bending contours and thickness fringes.

Figure 3.4 shows bright–field (BF) and dark–field (DF) cross section diffraction contrast STEM images recorded using $g_{\bar{2}20}$ of the buffer layer. The line contrasts in Fig. 3.4 can be attributed to dislocations. Figure 3.4 (a) and (b) show a sample with a thin Type II buffer layer. A high density of dislocations in the buffer layer was observed. The rearrangement and annihilation of the dislocations in the buffer layer were limited, and the dislocation density was the same at the substrate/buffer and buffer/$Cd_3As_2$ interfaces. Dislocation images for the sample on the thick Type II buffer layer (Fig. 3.4 (c) and (d)) indicate that threading dislocations (TD) are created at the substrate/buffer interface. However, most of the TDs are annihilated in this thick Type II buffer layer. Fig. 3.4 (e) and (f) show the $Cd_3As_2$ film on a thick Type I buffer layer. There is a

high density of dislocations at the substrate/buffer and the first interface between the filtering layers. However, because of the effective dislocation filtering, many TDs cease to propagate through the layers and into the $Cd_3As_2$. In our experiment, we observed the same result in reducing the density of TDs at the buffer layer by inserting filtering layers or by growing a thick buffer layer. The two sets of dislocations in the buffer layers were identified: one with Burgers vectors $\frac{1}{2}$ <1$\bar{1}$0> and another one partials with Burgers vectors $\frac{1}{6}$ <112>. The partials dislocations with Burgers vectors $\frac{1}{6}$ <112> have small residual contrast with $g_{\bar{2}20}$ (marked by yellow arrows in Fig.3.4). The important finding of this study is that not all the dislocations enter into the $Cd_3As_2$ films. The dislocations with Burger vectors $\frac{1}{2}$ <1$\bar{1}$0> enters into the $Cd_3As_2$ films, whereas partial dislocations with Burgers vectors $\frac{1}{6}$ <112> terminate at the buffer/$Cd_3As_2$ interface. The density of dislocations in $Cd_3As_2$ films grown on Type I and thick Type II buffer layers were comparable ($2.1\times10^9$ cm$^{-2}$ and $2.6\times10^9$ cm$^{-2}$ respectively) and in both cases, the TD density of $Cd_3As_2$ film was an order of magnitude less than the $Cd_3As_2$ film grown on the thin Type II buffer layer ($1.9\times10^{10}$ cm$^{-2}$).

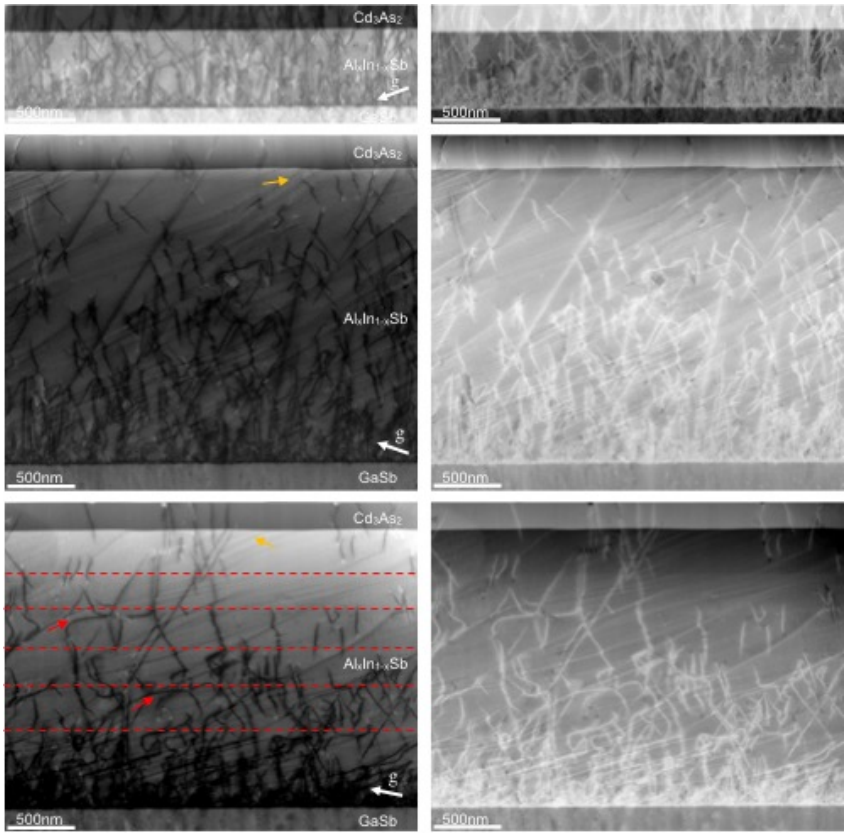


Figure 3.4: Bright-field (left) and dark-field (right) STEM image of the $Cd_3As_2$ films with different buffer layer structures showing the dislocation (Image courtesy of Salva Salmani-Rezaie).

## 3.4 Effect of dislocations on the electrical transport

We studied the electrical transport in thick and thin $Cd_3As_2$ films grown on different buffer layers. Carrier mobility was found to be dependent on film thickness and Fermi level, similar to (112)-oriented relaxed $Cd_3As_2$ films (discussed in chapter 4)[65, 110]. Therefore, it is important to compare the carrier mobility for the same thickness and carrier density. The carrier mobility increased with the film thickness and for the sufficiently thin films ($< 45$ nm), the electrical transport was from 2D surface states while the bulk electronic band was gapped out by quantum confinement. Figure 3.5 shows the

electron mobility and carrier density for thick (> 210 nm) $Cd_3As_2$ films as a function of temperature. It must be noted that the $Cd_3As_2$ films in these three structures were of slightly different thicknesses. On the Type I buffer layer the $Cd_3As_2$ was 210 nm, with a carrier mobility of 26,000 $cm^{-2}V^{-1}s^{-1}$. On the thick Type II buffer layer the $Cd_3As_2$ was 250 nm, while on the thin Type II buffer layer the $Cd_3As_2$ was 230 nm. Both films on the Type II buffer layers have the mobility of 20,000 $cm^{-2}V^{-1}s^{-1}$. Overall, similar carrier mobility, independent of the buffer layer, was obtained for thick $Cd_3As_2$ films. Further, the thickest 1.3 $\mu$m $Cd_3As_2$ film on thin Type II buffer layer exhibited a mobility of 41,000 $cm^{-2}V^{-1}s^{-1}$ at 2 K, which is currently the highest value measured for thin films of this material.

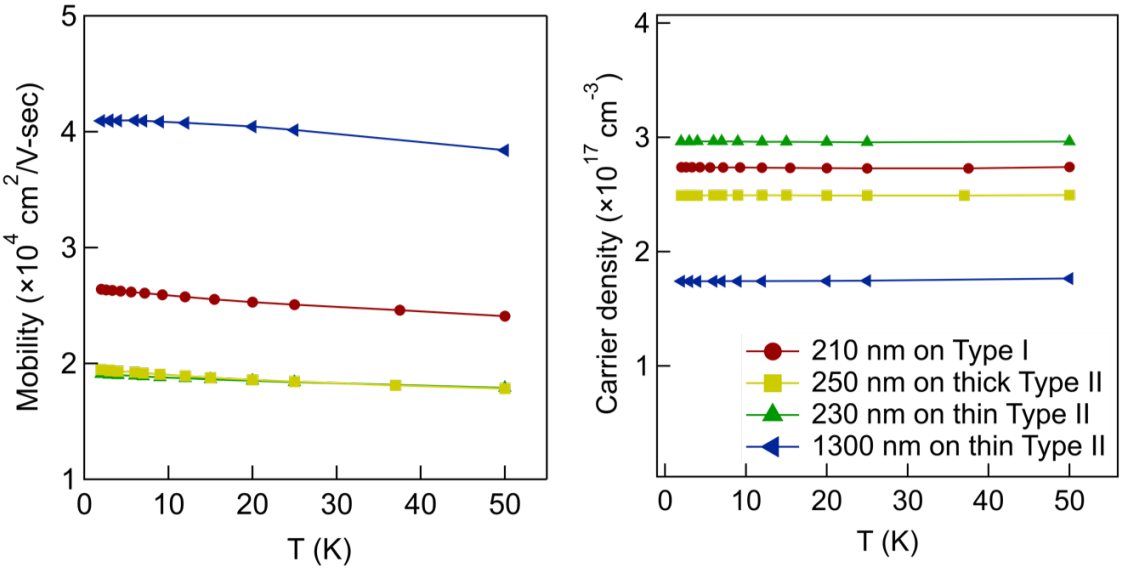


Figure 3.5: Electron mobility (left) and carrier density (right) for $Cd_3As_2$ films grown on different buffer layer structures.

Next, we compare the electronic transport of thick (210–250 nm) $Cd_3As_2$ with different dislocation densities. Recall from the TEM images (Fig. 3.4) that the dislocation density in the $Cd_3As_2$ films grown on the thin Type II buffer layer is an order of magni-

tude higher than those of the films grown on the thick Type II buffer layer and the Type I buffer layers. The carrier densities for all three films were in the range of 2.5–3$\times 10^{17}$ $cm^{-3}$(Fig. 3.5). These results suggest that an order of magnitude difference in dislocation density does not proportionally impact the electron mobility. Carrier mobility increases with further increasing the film thickness. Dislocations in the $Cd_3As_2$ films align vertically, therefore, the dislocation density in the thick $Cd_3As_2$ films does not appear to decrease with film thickness, and the majority of the dislocations traverse through the film. Thus, the increase in carrier mobility with film thickness is due to the increased bulk contribution. This insensitivity of carrier mobility of the thick films can be explained by the following two reasons. First, the bulk mobility may be limited by some other mechanisms such as point defects due to As vacancy. Second, the topological nature of $Cd_3As_2$ makes the carrier immune to the back-scattering. Hence, the Hall mobility is unaffected.

To further understand the role of dislocations on carrier transport, studies were carried out on thin $Cd_3As_2$ films ( 45 nm) grown on the Type I buffer layer and thin Type II buffer layers. On the Type I buffer layer, the thin film has a high mobility of 11,500 $cm^{-2}V^{-1}s^{-1}$. On the thin Type II buffer layer, the thin film shows lower mobility of 5,000 $cm^{-2}V^{-1}s^{-1}$. The magneto-transport measurement shows well-developed quantum Hall plateaus for both films (Fig.3.6). The sheet carrier density was found to be similar ($6\times 10^{11}$ $cm^{-2}$). Furthermore, the carrier densities calculated independently from low-field Hall data, and the quantum oscillations are in good agreement, providing more evidence that the total transport is coming from the 2D surface states. The quantum mobility is calculated from the onset of quantum oscillations (using the criterion $\mu_Q B = 1$)[111], and for the high-mobility film is 4,000 $cm^{-2}V^{-1}s^{-1}$, and for the low-mobility film is 3,000 $cm^{-2}V^{-1}s^{-1}$. This indicates the quantum mobility of the surface states is less affected than the Hall mobility by the dislocation density.

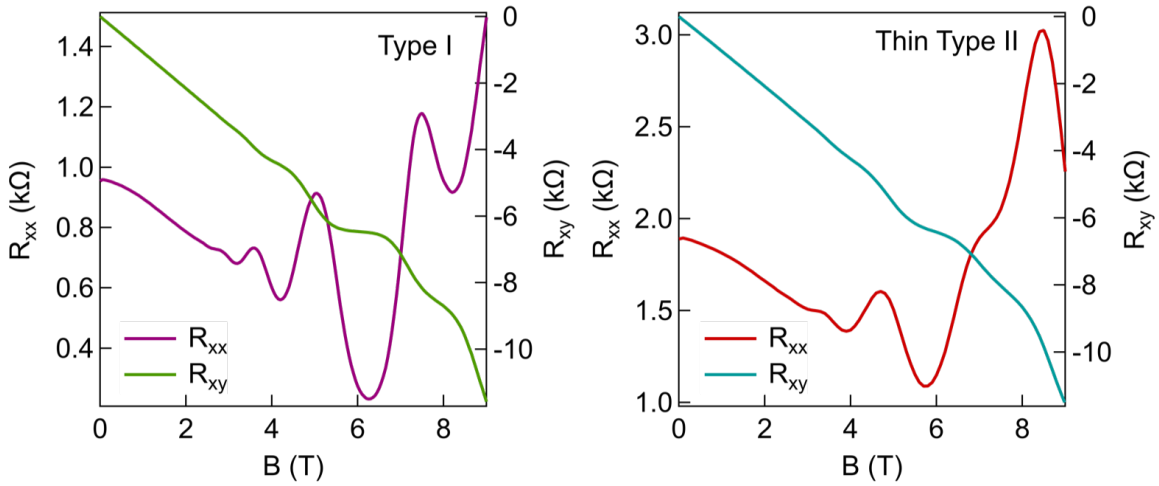


Figure 3.6: Hall resistance ($R_{xy}$) and longitudinal resistance ($R_{xx}$) for thin (45 nm) $Cd_3As_2$ films grown on Type I (left) and thin Type II (right) buffer layer.

Finally, we discuss potential scattering mechanisms that can affect the observed electronic transport in our films. The possible major scattering mechanisms are phonon scattering, surface roughness, dislocations, point defects, and impurities. Since all transport data were taken from 2 K to 50 K, the effects of phonon scattering were excluded first. The contribution to scattering from the different types of disorder can be estimated by comparing classical and quantum mobility. Classical mobility, which determines the conductivity of the sample, is unaffected by small-angle scattering. On the other hand, quantum mobility is affected by all angle scattering events and is calculated from quantum oscillations in magnetic field. The ratio between these two mobilities indicates the nature of the scattering source and ultimately tells the dominating scattering mechanism in the transport. Scattering by short-range disorder is isotropic and the ratio is close to 1. For the long-range disorder, this ratio diverges. For example, the surface roughness, which is a short-range type scattering, has been shown to give a scattering ratio close to 1 for Si metal-oxide-semiconductor field-effect transistors (MOSFET) [112]. Moreover, for the case of GaAs/AlGaAs heterojunctions, where the dominating scattering source is

long-range, this ratio is of the order of 10 [112]. However, For Dirac semimetal, backscattering is forbidden due to spin momentum locking of the electrons. Hence, the scattering ratio, even when short-range scattering is the dominating mechanism, is greater than 1 [113]. For our thin films, the scattering ratio was calculated to be 2.9 for the high mobility film and 1.7 for the low mobility film. This small ratio indicates that transport in the thin films is dominated by short-range scattering. We can eliminate the surface roughness as the limiting mechanism in our case because the film grown on the Type I buffer has an RMS surface roughness of 4.9 nm, while the film on the thin Type II buffer layer has an RMS surface roughness of 1.5 nm. This observation contradicts the measured scattering ratio. The film with higher surface roughness shows the larger ratio (2.9) indicating that the dominating scattering is large angle in comparison to the ratio for the smoother film. The screening for both samples can be considered to be the same due to the same carrier density. Thus, the ratio should increase for the smoother film which is not the case in our thin films. Moreover, for the thick (210–250 nm) $Cd_3As_2$ films where the films on thick Type II buffer layer and Type I buffer have an RMS roughness of 5.6 nm and 5.2 nm, respectively and the $Cd_3As_2$ film on the thin type II buffer layer is smoother, with an RMS roughness of 1.8 nm. The carrier mobility shows no correlation with the surface roughness for the thick $Cd_3As_2$ films. Thus, we can safely discard surface roughness as a dominating scattering mechanism in our thick and thin films. As mentioned earlier, the dislocations show no significant effect on the transport of the thick $Cd_3As_2$ films. However, both the classical and the quantum mobility are reduced for the thin films. These findings for the thick $Cd_3As_2$ films, where the transport is dominated by the bulk, suggest that the carrier transport is limited by some other mechanism, most probably point defects due to Cd or As vacancies. The surface transport is limited by the dislocations in the bulk. The explanation for this effect is not clear at this point and needs further study. A future study on the scattering ratio with different carrier density would

be helpful to identify the source of the limiting mechanism for the transport. Further, a growth study with the co-deposition of As and its effect on transport would be helpful to understand the scattering mechanism and improve the film quality by reducing the point defects.

In conclusion, we have demonstrated the growth of $Cd_3As_2$ along the (001) plane on lattice-matched buffer layers. A high mobility of 41,000 $cm^{-2}V^{-1}s^{-1}$ was obtained. The electronic mobility for the thick $Cd_3As_2$ films is unaffected by the dislocation density. However, for the thin $Cd_3As_2$ film, the classical mobility is greatly reduced but the quantum mobility is only reduced slightly. This study shows that electronic transport from the bulk states is not limited by dislocation density and surface roughness and more likely to be limited by charged defects, such as As vacancies, in the bulk of the material. In contrast, the transport in the thin films when the transport is from the surface states are limited by bulk dislocation.

## 3.5 Capping layer

Electrical transport from the surface states is sensitive to air exposure. Electrical transport in thin films (<60 nm), irrespective of their crystallographic orientation, showed a non-linear Hall resistance at the high magnetic field. Figure 3.7(a) shows the longitudinal ($R_{xx}$) and transverse ($R_{xy}$) resistance for the (112)-oriented 30 nm thick $Cd_3As_2$ films. Two different types of carriers were identified by fitting the $R_{xx}$ and $R_{xy}$; high mobility n-type carrier from the surface electronic state and low mobility p-type carrier from the bulk electronic state. X-ray photoemission spectroscopy (XPS) studies showed the absorption of $OH^-$ ions on the top surface. These ions bend the electronic bands upward at the surface (Fig.3.7(c)). To overcome this issue, surface passivation by low energy $N^*$ plasma was developed. After the surface treatment, the Fermi level increased and as

a result a single n-type carrier transport from surface states was measured[110]. Similar results in magnetotransport were obtained when films were annealed at 350 K before measurement. Figure 3.7(b) shows the longitudinal ($R_{xx}$) and transverse ($R_{xy}$) resistance after 20 minutes annealing at 350 K. A linear Hall resistance with a negative slope was observed. Moreover, pronounced quantum oscillations in longitudinal resistance ($R_{xx}$) from the surface states were measured. These results show that the transport properties of thin $Cd_3As_2$ films are very sensitive to the surface conditions.

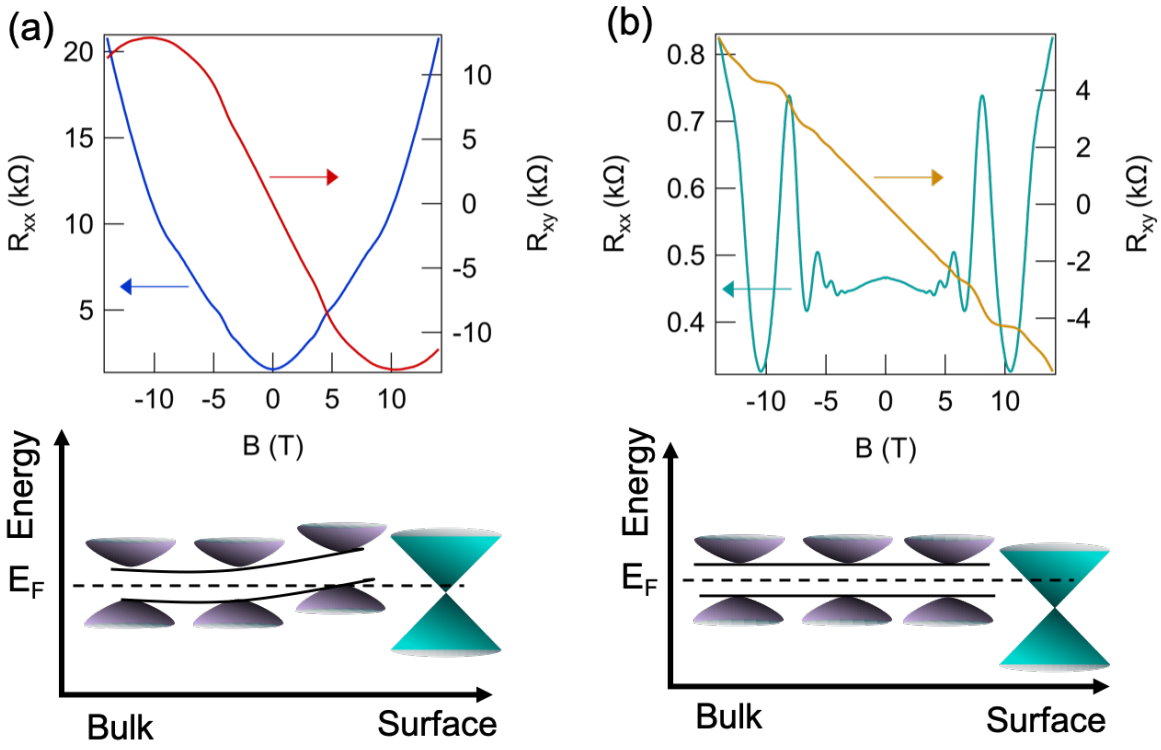


Figure 3.7: (a, b), Longitudinal ($R_{xx}$) and transverse ($R_{xy}$) resistance at 2 K for the 30 nm thick $Cd_3As_2$ film before (a) and after (b) annealing. (c, d), Schematic of relative surface and bulk Fermi level of $Cd_3As_2$ before (a) and after (b) annealing.

*In-situ* growth of GaSb on top of $Cd_3As_2$ was developed to improve the consistency of electrical measurement in the thin films. Surface treatment provided a way to measure the transport from the surface states, however, this method had some limitations. First,

transport measurements were time-sensitive because it was inevitable to avoid air exposure during transfer for measurements after the surface treatment. Second, exposure to $N^*$ plasma damages the surface. For the thick films, the increase in the carrier density depended on the plasma power and exposure time. Moreover, device yield for the thin films (<30 nm) was low due to the damage on the surface by processing steps. Therefore, a stable and robust solution was needed to protect the top surface and improve the consistency in transport measurements.

## 3.6 Low temperature growth of GaSb

Migration enhanced epitaxy (MEE) was used to develop the growth of GaSb at low temperatures. The growth temperature for $Cd_3As_2$ is relatively low (<130 °C) and high-temperature treatment degrades the film. Thus, a low-temperature growth technique was needed to grow the capping layer. However, high-quality III-V compounds films are grown at high temperatures with an overpressure of the group V element. MEE has been shown to produce high-quality atomically smooth epitaxial films of GaAs and AlGaAs at relatively low temperatures [114, 115, 116]. In this method, group III and V fluxes are supplied separately with an intermediate annealing step. For GaAs growth by MEE, when Ga atoms are supplied on As terminates surface, they bond with As. However, their boding with As is unstable due to another unsatisfied bond. Therefore, Ga atoms diffuse on the surface and nucleate on the kinks and steps which promotes two-dimensional growth. This diffusion length is controlled by the annealing time after the Ga deposition. After annealing, As is supplied while Ga is off. Like the conventional MBE technique discussed previously, the growth is monitored by the RHEED. However, RHEED oscillations in MEE originate due to the difference in the reflectivity of Ga covered and As covered surfaces [114]. When Ga flux is supplied, RHEED intensity

drops. The RHEED intensity is recovered by supplying As flux. Molecular flux supply and annealing time are optimized to recover the RHEED intensity as before growth. It has been shown that RHEED intensity is recovered most when Ga and As are supplied for a monolayer growth[114, 115, 116]. In this study, we decided to grow the GaSb on $Cd_3As_2$ using the same approach.

GaSb growth on GaSb was optimized at a low temperature (<200 °C) using MEE. The substrates temperature was measured by optical pyrometer. For the best quality growth, a controlled supply of molecular flux is important. Ga and Sb fluxes were calibrated using RHEED oscillation during high-temperature GaSb growth. A monolayer of Ga and Sb was deposited with a shutter interruption. A flux of $1.55\times10^{-7}$ Torr and $4\times10^{-7}$ Torr for 2.7 and 3.1 seconds were supplied for monolayers of Ga and As, respectively. Figure 3.8 shows the RHEED intensity during the growth with a 3 seconds annealing time. RHEED intensity after growth is almost similar to before growth, indicating the high-quality growth of GaSb. Further growth was done using these optimized conditions.

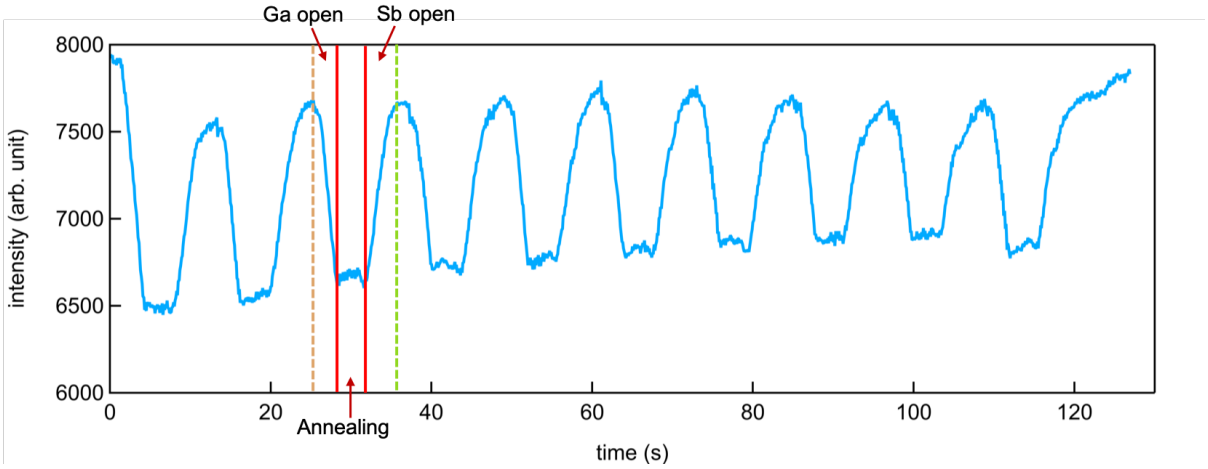


Figure 3.8: Change in the RHEED intensity during the GaSb growth by MEE.

## 3.7 Growth of GaSb on $Cd_3As_2$

GaSb was grown on $Cd_3As_2$ using the conditions optimized for the growth on GaSb. $Cd_3As_2$ was grown on the thick Type II lattice-matched buffer layer. Fig. 3.9 shows the RHEED after $Cd_3As_2$ and capping layer growth. RHEED after the capping layer growth showed the amorphous growth of the GaSb on $Cd_3As_2$. This amorphous growth is likely due to different bonding energy between the Sb and $Cd_3As_2$ surface that affects the diffusion length of the Sb atom on the surface. In another attempt, the growth of the capping layer growth was started with Ga flux. This did not give any significant difference in the growth mode and a similar amorphous RHEED was observed.

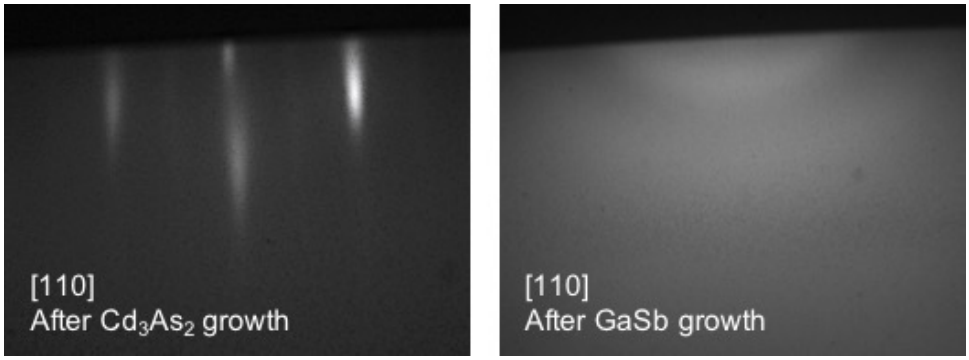


Figure 3.9: RHEED after the $Cd_3As_2$ (left) and GaSb capping layer (right) growth.

Figure 3.10 shows the AFM for a GaSb capping layer grown on $Cd_3As_2$. AFM shows a similar surface roughness as the uncapped $Cd_3As_2$ film with no significant change in surface morphology. This indicates the conformal growth of GaSb on $Cd_3As_2$. This conformal growth satisfies our requirement that the capping layer protects the surface from air exposure.

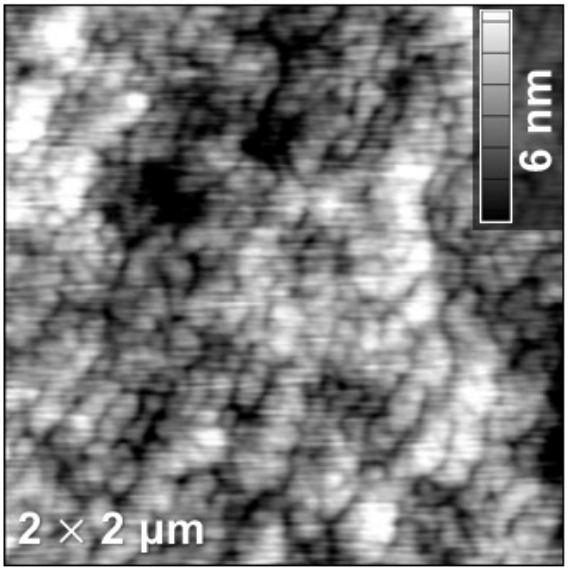


Figure 3.10: AFM image for the GaSb capping layer grown on the top of $Cd_3As_2$.

Temperature annealing steps were tested to improve the structural quality of the capping layer. The amorphous growth of GaSb indicates the poor diffusion length of Ga and Sb on the $Cd_3As_2$ surface. Initially, longer annealing times were tried to improve the diffusion length of the molecules but this did not improve the film quality. Increasing the substrate temperature is another way to improve the diffusion length, however, the maximum temperature is limited by the $Cd_3As_2$. Therefore, the first growth of 4 monolayers was done at a lower temperature and then the temperature was raised to improve the capping layer quality.

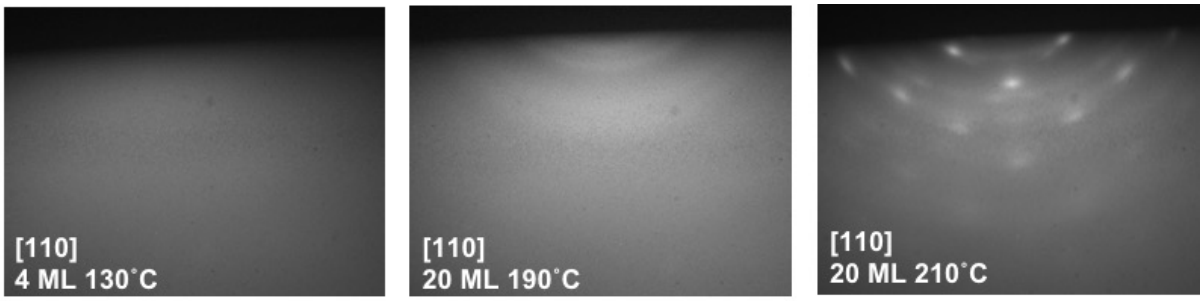


Figure 3.11: RHEED at different growth temperatures of the GaSb capping layer.

Figure 3.11 shows RHEED after various steps of temperature annealing. First, 4 monolayers of the GaSb capping layer were grown at the $Cd_3As_2$ growth temperature (125 °C). RHEED shows a diffuse pattern indicating an amorphous layer. The substrate temperature was then raised to 190 °C and another 20 layers were grown. RHEED after growth shows a ring pattern indicating a polycrystalline structure. Upon further increasing the substrate temperature to 210 °C, and growing an additional 20 monolayers, RHEED showed polycrystalline spots. This indicates an improvement in the crystalline quality of the films by temperature treatment.

## 3.8 Effect of capping layer on the electrical transport

We studied the effect of the capping layer on electrical transport. A thin layer (10 monolayers) of GaSb was grown on top of $Cd_3As_2$. The $Cd_3As_2$ films were grown on a thick Type II lattice-matched buffer layer. 25 nm thick $Cd_3As_2$ films showed carrier mobilities in the range of 10,500−12,500 $cm^{-2}V^{-1}s^{-1}$ with carrier densities $1-3\times10^{12}$ $cm^{-2}$. The carrier density is in the same range after the surface passivation steps on uncapped films, which confirmed no carrier depletion after air exposure. Further, we studied the electrical transport in the capped $Cd_3As_2$ film after annealing. This annealing was done to improve the structural quality of the capping layer. The carrier mobility

was measured to be 7,000 $cm^{-2}V^{-1}s^{-1}$. This mobility is slightly lower in comparison to the unannealed film with the capping layer. Further growth study with low annealing temperature and longer time is needed to minimized thermal damage to the $Cd_3As_2$ films.

Films with a capping layer showed significantly improved electrical transport compared to uncapped films, with a factor of 1.5 increase in the mobility of thin films. Moreover, electrical transport from 10 nm thick film was measured. In our previous study, the electrical transport from the films was sensitive to device-fabrications steps and surface treatment processes and device yield was significantly lower for films thinner than 30 nm. By developing the capping layer, we were able to measure electrical transport on films as thin as 10 nm. Consistent electrical transport, independent of air exposure time, was measured and the need for surface treatment was eliminated.

### 3.8.1 Carrier density dependent carrier mobility

We further measured the carrier mobility at different Fermi levels. Figure 3.12 shows the carrier mobility as a function of carrier density for 18 nm and 24 nm thick $Cd_3As_2$ films. The disconnected points showed the carrier mobilities before gate oxide deposition. The carrier density was modulated from $5\times10^{11}$ $cm^{-2}$ to $2\times10^{12}$ $cm^{-2}$ by electrostatic gating. We observed a decrease in carrier mobility with the increase in the carrier density. A high Hall mobility of 22,000 $cm^{-2}V^{-1}s^{-1}$ was observed for 25 nm thick films at $5\times10^{11}$ $cm^{-2}$ carrier density. This is one of the highest mobilities achieved in our thin films (25 nm).

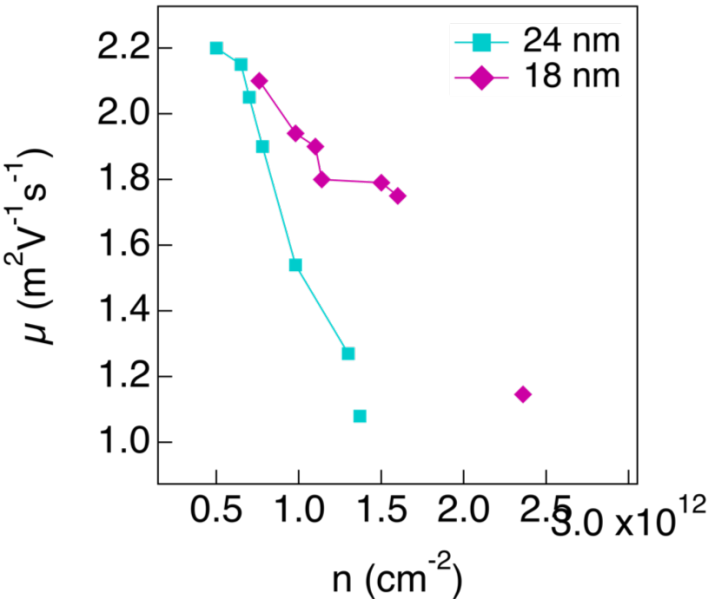


Figure 3.12: Carrier mobility as a function of carrier density for capped $Cd_3As_2$ films.

The mobility behavior with carrier density can be explained by two scattering mechanisms; long-range Coulomb scattering and short-range scattering. These mechanisms dominate in different carrier density ranges. Since all the measurements were done at 2 K, we can disregard the contribution from phonon scattering. The long-range scattering is due to remote charged impurities. At low carrier density, the long-range scattering dominates the scattering time and the scattering time increases with the rise in carrier density due to the enhanced screening of charge impurities[117, 118]. For parabolic bands, the scattering time is proportional to $n$ in the strong screening limit, where $n$ is the carrier density. As a result, the mobility increases with the increase in carrier density for conventional 2D semiconductors. For 2D Dirac electrons, the scattering time is proportional to $\sqrt{n}$[40, 39]. The carrier mobility for Dirac materials is defined differently than for the parabolic bands. The carrier mobility is proportional to scattering time and inversely proportional to Fermi energy (discussed in chapter 1). The Fermi

energy is proportional $\sqrt{n}$ for 2D Dirac dispersion. As a result, mobility is unaffected by the screening. In the high carrier density limit, short-range scattering dominates. For short-range scattering, the scattering time for 2D semiconductor and 2D Dirac material decreases with the increase in the carrier density[40, 39]. As a result, carrier mobility decreases with a further increase in carrier density.

Carrier density-dependent electrons mobility indicated the Dirac nature of carriers in our films. We observed the reduction in carrier mobility with the increase in the carrier density. This showed that the carrier mobility is not influenced by the long-range scattering. The hysteresis in the gating study confirmed the presence of charged impurities in our films. The decrease in mobility is due to short-range scattering. Interface roughness has been shown as a short-range scattering source for conventional 2D semiconductors [117]. For conventional semiconductors, the carriers are pushed to the interface with the increase in the Fermi level, and therefore, carrier mobility decreases with the increase in carrier density. In the previous section, we showed that surface roughening is not the mobility limiting mechanism in our films. The source of short-range scattering is not clear yet and requires further studies.

In conclusion, we achieved high carrier mobility in thin films by developing the capping layer. The surface treatment procedure was eliminated and consistent results in electrical transport were obtained. The gating study confirmed the Dirac nature of the carrier in our films. This study opens the door for heterostructuring of $Cd_3As_2$.

# Chapter 4

# Electrical transport

Magnetotransport measurements are an experimental tool to probe the electronic states of materials. We performed electrical transport measurements at high magnetic field to study the electronic structure of bulk and surface electronic states and explored their evolution under quantum confinement and epitaxial strain. In the first part, thickness-dependent magnetotransport is discussed. In the second part, a magnetotransport study was done on biaxially strained $Cd_3As_2$ films.

## 4.1 Thickness dependence study

### 4.1.1 Motivation

$Cd_3As_2$ has gapless Dirac dispersion in bulk electronic structure and an arc-type surface state. Quantum oscillations from these gapless surface states are predicted in the form of a new Weyl orbit mechanism[60, 61]. This Weyl orbit mechanism is explained in chapter 1. The oscillations by the Weyl orbit were experimentally shown for different microstructures of $Cd_3As_2$[62, 63, 119]. These studies were done on a relatively thick (>50 nm) sample with a large contribution from bulk electronic states.

It is important to reduce the bulk contribution to understand the nature of quantum oscillations from surface states. Molecular beam epitaxy provides an excellent way to control the thickness up to a single layer. Therefore, a systematic study with great control over the bulk contribution is possible in epitaxial films. Theoretical studies for the thin films showed that the bulk Dirac nodes gapped out due to the quantum confinement and surface states remains gapless up to very thin films of 5 nm [7, 120]. We reported the quantum Hall effect from the two-dimensional surface statest in 30 nm $Cd_3As_2$ grown on GaSb/GaAs [121]. The quantum Hall effect was shown from surface states and the bulk electronic band developed a bandgap due to quantum confinement. However, in another study done on the thin films of $Cd_3As_2$ (10 nm–30 nm), these two dimensional states were assigned to quantum-confined bulk states [122].

A systematic magnetotransport study with a controlled thickness is required to obtain additional insight into the surface and bulk electronic states. The study on GaSb for 30 nm thick $Cd_3As_2$ confirms the existence of 2D surface states in thin films. However, the questions about the relative bulk and surface state contributions remained unanswered. The remaining unanswered questions were the extent to which the bulk contributes to the total electrical transport and the thickness range for gapping out the bulk bands due to quantum confinement. To answer these questions, we performed a detailed magneto-transport study by systematically varying the films' thickness. Moreover, the transport study would provide further insight into the origin of these 2D electronic states.

### 4.1.2 Effect of thickness on magnetotransport

We performed a magnetotransport study on a series of $Cd_3As_2$ film with a thickness range of 10–350 nm. Films were grown on 4° miscut CdTe substrates. Electrical measurements were done on 100×100 $\mu m^2$ size Hall bars structure except for the 350 nm

thick film. The Van der Pauw method was used to perform electrical characterization on the 350 nm thick film. Hall mobility and carrier density were measured by the slope at the low magnetic field (-0.5 T to +0.5 T). All the films showed electrical transport from n-type carriers. Figure.4.1 shows the carrier mobility as a function of temperature. The highest mobility of 22,000 $cm^{-2}V^{-1}s^{-1}$ was measured for 350 nm thick films. The carrier mobility decreased with the films thickness.

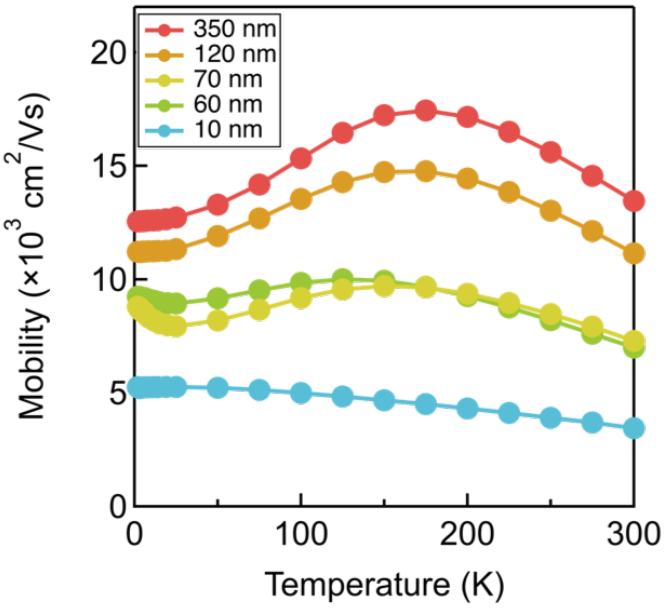


Figure 4.1: Carrier mobility for different thicknesses of $Cd_3As_2$ films grown on CdTe.

Figure. 4.2 shows longitudinal ($R_{xx}$) and Hall resistance ($R_{xy}$) for a 10 nm thick $Cd_3As_2$ film at 40 mK. Hall resistance ($R_{xy}$) showed well-developed plateaus. These plateaus coincide with the minima in the $R_{xx}$. The resistance for quantum Hall plateaus is given by the expression $h/\nu e^2$, where $\nu$ is the filling factor, $\hbar$ is Plank's constant, and $e$ is the electron charge. Based on the resistance value, 2-fold degenerated Landau level with filling number 2,4,6,8 were identified. The lowest Landau level of 2 was observed at 10 T magnetic field with no sign of lifting in the degeneracy up-to 14 T. An almost

vanishing longitudinal resistance and well-matched quantized Hall plateaus confirmed the contribution was solely from 2D electronic states in 10 nm thin film.

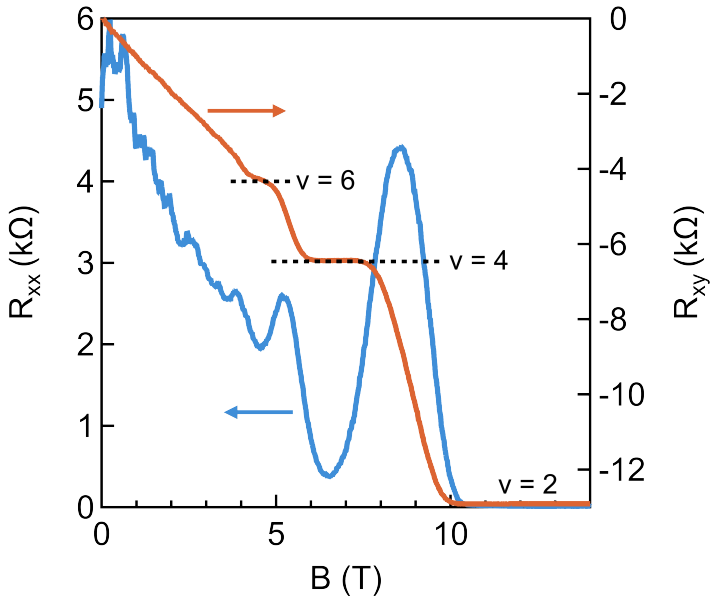


Figure 4.2: $R_{xx}$ and $R_{xy}$ for 10 nm thick $Cd_3As_2$ films showing the quantum Hall effect.

Figure.4.3 (a) shows the normalized longitudinal resistance ($R_{xx}$) for films with different thicknesses at 2 K. Longitudinal resistance was normalized to zero magnetic field resistance value. We observed Shubnikov-de Haas oscillations (quantum oscillations) for all films.

Carrier density was abstracted from Shubnikov-de Haas oscillations. Shubnikov-de Haas oscillations are periodic in 1/B. The carrier density for two-dimensional carriers is given by $2 * f * \frac{e}{\hbar}$. $\hbar$,$e$,$f$ are the reduced Plank's constant, electron charge, and oscillation frequency. The frequency is calculated from the slope of the fan diagram. The fan diagram is the plot of the Landau level index with the inverse of the magnetic field.

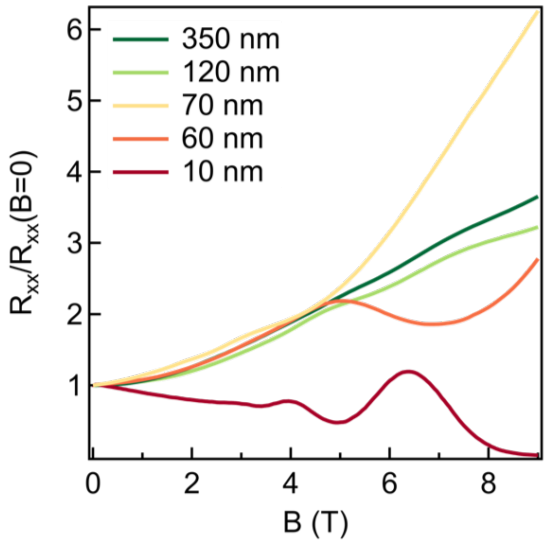


Figure 4.3: Longitudinal resistance at 2 K for $Cd_3As_2$ films of different thicknesses.

Figure 4.4 (a) shows the fan diagram plotted for the different thicknesses. The fan diagrams for the 60 and 70 nm thick films are not plotted due to the limited number of quantum oscillations. The intercept of the fan diagram gives the Berry phase. We observed zero intercepts for all the films indicating zero Berry phase (Fig. 4.4 (a)). Figure 4.4 (b) shows the 2 D carrier density calculated from the fan diagram and low field (-0.5 T $<$ B $>$ 0.5 T) Hall measurements for different thicknesses. The carrier density calculated from the Hall measurement depended on the film thickness, whereas the carrier density calculated from quantum oscillations was nearly independent of the film thickness. Moreover, the 3D carrier density remained the same, indicating the similar structural quality of the films irrespective of their thickness.

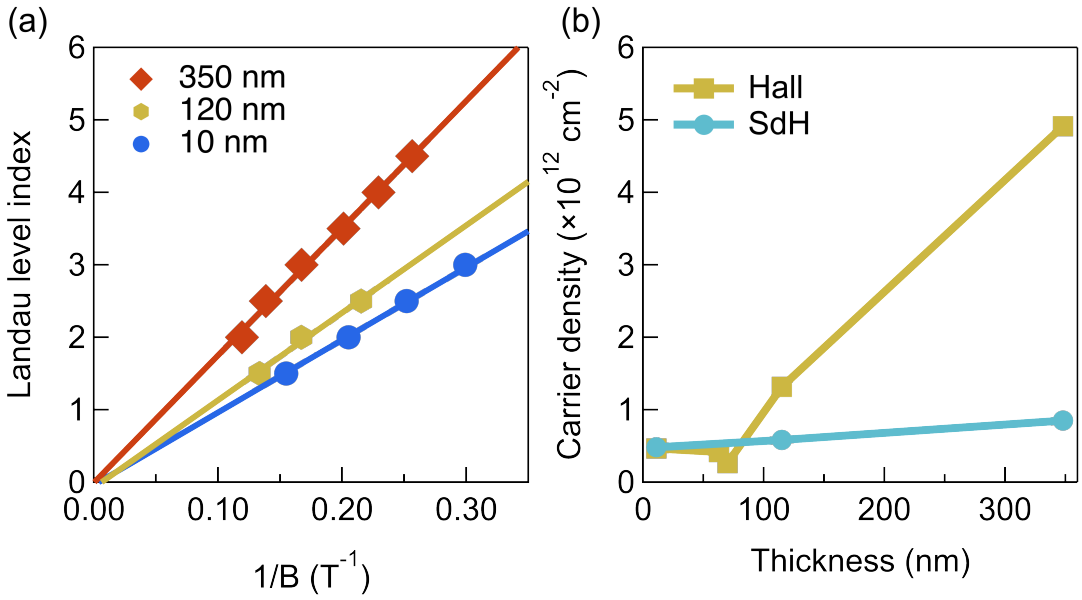


Figure 4.4: (a), Fan diagram plotted for the Landau levels used for the carrier density calculation for (b). Data is shown for the minima and maxima of oscillations where maxima are assigned to half-integer Landau indices. (b), comparison of carrier density calculated by low field Hall data and Shubnikov-de Haas (SdH) oscillations.

We further fit quantum oscillation amplitude ($\Delta$R/R) at different temperatures. The effective mass ($m^*$) and quantum mobility ($\tau_q$) were extracted by the fitting. $\Delta$R/R were fitted by the following equation[123]

$$\frac{\Delta R_{xx}}{R_0} = \frac{8 * \pi^2 k_B T/\hbar\omega_c}{\sinh(2\pi^2 k_B T/\hbar\omega_c)} \exp(-\frac{\pi}{\omega_c \tau_q}).$$

$$\text{where,} \quad \omega_c = \frac{eB}{m^*},$$

$\hbar$ is reduced Plank's constant, $\omega_c$ is cyclotron frequency and $k_B$ is Boltzmann's constant. Figure.4.5 shows the fitting of $\Delta$R/R as a function of temperature. The quantum mobility is calculated by the relation $\mu_q = m^* e/\tau_q$.

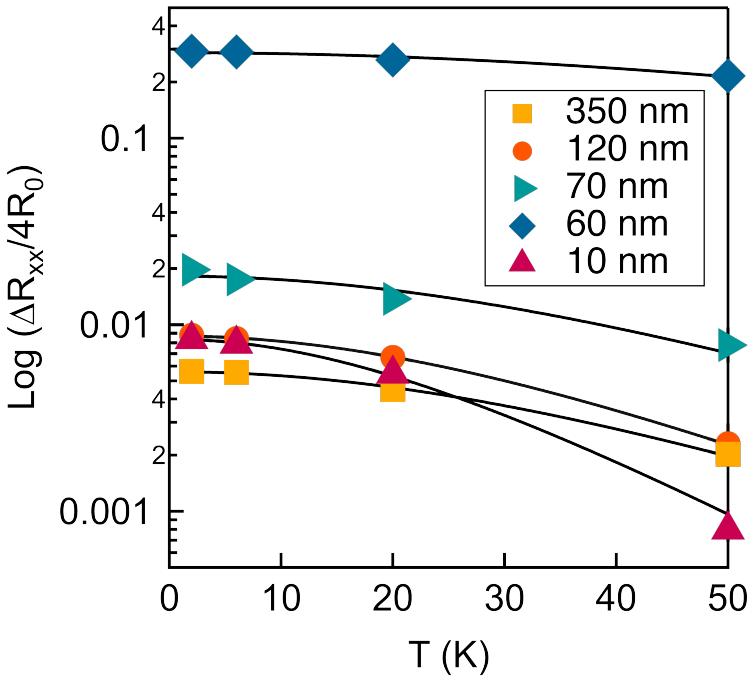


Figure 4.5: Relative amplitude ($\Delta$R/R) and fitting (solid line) of SdH oscillations as a function of temperature.

The extracted parameters from the fitting are shown in Table 1. We observed a very small effective mass for all the films. A small effective mass is expected for the Dirac electrons due to linear band dispersion. Low quantum mobility in comparison to Hall mobility was obtained for all the films. Quantum mobility, which is sensitive to all angle scattering, is generally lower than the Hall mobility. For a Dirac material, the difference between these mobilities is higher in comparison to conventional semiconductors because of backscattering protection from large-angle scattering.

| **Thickness (nm)** | **10** | **60** | **70** | **120** | **350** |
|---|---|---|---|---|---|
| $\mu_H$ ($cm^2$/V-s) | 5250±50 | 9230±20 | 8790±20 | 11210±50 | 12550±20 |
| $\mu_q$ ($cm^2$/V-s) | 1300±80 | 4300±700 | 1900±500 | 990±30 | 920±50 |
| $m^*$ | 0.034±0.001 | 0.011±0.001 | 0.014±0.002 | 0.029±0.001 | 0.024±0.001 |

Table 4.1: Quantum mobility, Hall mobility, and effective mass for different thicknesses of the $Cd_3As_2$films.

### 4.1.3 Discussion

Quantum Hall effect is measured for the 10 nm thin film, similar to the finding on films grown on GaSb substrates[121]. The fact that the quantum Hall effect in the thin films is independent of the substrate indicates that these 2D states are intrinsic to $Cd_3As_2$. Sheet density measured from low field Hall data increased with the film thickness. This showed the contribution of the additional carriers from bulk electronic states. These bulk states gapped out due to the quantum confinement effect and the gap increases with the decrease in the film thickness. In our study, we observed this gap opening for 60–70 nm thick films. Since all these measurements are compared at 2 K, thermal excitation of carriers does not play a significant role. The decrease in Hall mobility with film thickness implied that high mobility carriers are from the bulk electronic states.

An intriguing finding of our study was carrier density calculated by the quantum oscillations was independent of the film thickness. These carriers are from 2D electronic states and present in all films. These carriers give Shubnikov-de Haas oscillations in thick films and quantum Hall effect in the thin films. This finding confirmed that these 2D states are not from quantum-confined bulk. For quantum-confined bulk state, one would expect these 2D states to be strongly dependent on the film's thickness.

A small effective mass is observed for thin films. The effective mass dropped to a significantly lower value for 60–70 nm thickness. Interestingly, this is the thickness range

at which the bulk electronic bands gap out and the Fermi surface of the surface states disconnects from the bulk electronic states. A theoretical study would be helpful to understand this behavior. We observed a zero Berry phase in our films. This zero Berry phase is shown for the conventional electrons and a non-zero Berry phase is expected for Dirac electrons[124]. The surface states of 3 D Dirac semimetal are sensitive to the Fermi level and perturbation. For the special case, these states form a loop disconnected from the bulk nodes[29]. If that is the case, we would expect a zero Berry phase due to two Dirac nodes of opposite chirality enclosed in the electron orbit. Thus we do not draw any conclusion about the Dirac nature of electronic states based on the Berry phase.

Further, we discuss the degeneracy of the Landau level. We observed a 2-fold degeneracy for 10 nm thick films. Due to the large g-factor for $Cd_3As_2$, we expect that spin degeneracy is already lifted at the low magnetic field [125, 126]. Since the surface states of a 3D Dirac semimetal consists of two sets of Fermi arc[127], we expect a two-fold degeneracy in the quantum Hall effect. The lifting of degeneracy at high magnetic field was observed in the quantum Hall effect for $Cd_3As_2$ grown on GaSb[121]. For the $Cd_3As_2$ films grown on GaSb, we measured a slight tilt in $Cd_3As_2$ film with respect to GaSb/GaAs by omega scan in XRD measurements. The tilt has been shown to lift the valley degeneracy for Si/SiGe quantum wells[128]. Moreover, the carrier mobility for $Cd_3As_2$ on GaSb is 2-fold higher than the thin films grown on CdTe. This low mobility leads to Landau level broadening and limits the resolution of Landau levels. Additionally, thickness and carrier densities are different for each film. The films grown on GaSb is 30 nm thick with $3\times10^{11}$ $cm^{-2}$[121]in comparison to the $Cd_3As_2$ film in this study is 10 nm thick with $5\times10^{11}$ $cm^{-2}$ sheet density. As shown in the study the surface states are very sensitive to the perturbation and Fermi level[29]. A theoretical study in this thickness range would be helpful to understand the evolution of surface states. Moreover, a gating study would provide more experimental data to get additional insight into the surface

states at different Fermi levels.

In conclusion, we showed the quantum Hall effect from the gapless surface states. This two-dimensional state is present for all the films and the bulk electronic states are gapped out for the thin films. This study confirmed that surface and the bulk states are simultaneously present for the thick films, as observed for the single crystal, and can be engineered by confinement.

## 4.2 Strain study

### 4.2.1 Motivation

3D Dirac semimetals sit in the proximity of many topologically trivial and non-trivial electronic states and can be tuned by breaking certain symmetries [129, 130, 5]. For example, by breaking the four-fold symmetry of $Cd_3As_2$, the 3D Dirac semimetal phase can be converted to a 3D topological insulator [7]. Moreover, the breaking of inversion symmetry would transform a 3D Dirac semimetal into a Weyl semimetal phase[130, 5].

Epitaxial strain provides an excellent way to study the strain-induced phase diagram. Straining can be carried out with great control. With that, it allows systematic studies, needed for the understanding of the underlying physics of phase transitions. For example, the in-plane strain is shown to engineer the semimetallic phase of HgTe into a topological insulator or the Weyl semimetal phase by selecting the suitable sign of strain[131, 132, 133].

### 4.2.2 Strain in thin films

We conducted a transport study in (112)-oriented $Cd_3As_2$ films by inducing epitaxial strain. This biaxial strain in (112)-oriented film breaks the 4-fold symmetry and as a

result, would transform $Cd_3As_2$ into a topological insulator[7]. Additionally, in this case, an additional topological phase transition as a function of strain has been predicted when mirror symmetry is present along a certain plane[134]. For this study, we tuned the lattice parameter of $In_xGa_{(1-x)}Sb$ buffer layer to induce the strain in $Cd_3As_2$. All films were grown on 3° miscut towards $<\bar{1}\bar{1}2>$ (111)B GaAs substrates. $Cd_3As_2$ growth conditions were kept the same for all the films. The electrical transport measurements were done on 30 nm thick $Cd_3As_2$ films in Hall bar geometry at 2 K.

Figure. 4.6 shows the out-of-plane XRD for 80 nm thick $Cd_3As_2$ films grown under different amounts of strain. The vertical dash line represents the peak position for relaxed $Cd_3As_2$ 2 2 4 reflections grown on GaSb/GaAs. Under compressive strain (bottom two plots in Fig.4.6), the $Cd_3As_2$ 2 2 4 peaks shift towards left. This indicates the increase in the out-of-plane lattice parameter of the film due to strain. We were unable to calculate the strain in the films due to the significant overlap between the film and the buffer layer peak. For the well-separated peak, a $-0.40\%$ of compressive strain is calculated in 80 nm $Cd_3As_2$ film. For the tensile strain direction, no change in $Cd_3As_2$lattice parameter was observed.

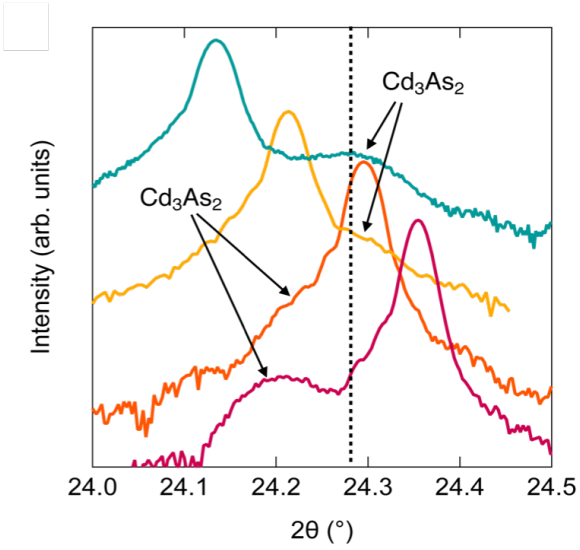


Figure 4.6: Out-of-plane $2\theta - \Omega$ scans for 224 reflection of $Cd_3As_2$ and 111 reflection of $In_xGa_{(1-x)}Sb$.

Figure.4.7 shows HAADF-STEM images for different films. Compressive strained films (Fig.4.7 (a)) and unstrained films (Fig.4.7 (b)) show an abrupt interface with no sign of misfit dislocations. Interestingly, we did not see any change in Cd vacancy ordering under strain. However, a semi-coherent interface was observed for (nominal) tensile strained films (Fig.4.7 (c)). This semicoherent interface can be seen from the inverse Fourier-filtered image (Fig.4.7 (d)) of Fig.4.7 (c). This incoherent interface for the tensile strain is consistent with the XRD finding and indicates relaxation in the films. The reason for this relaxation below critical thickness is not entirely clear and could be related to the thermal mismatch.

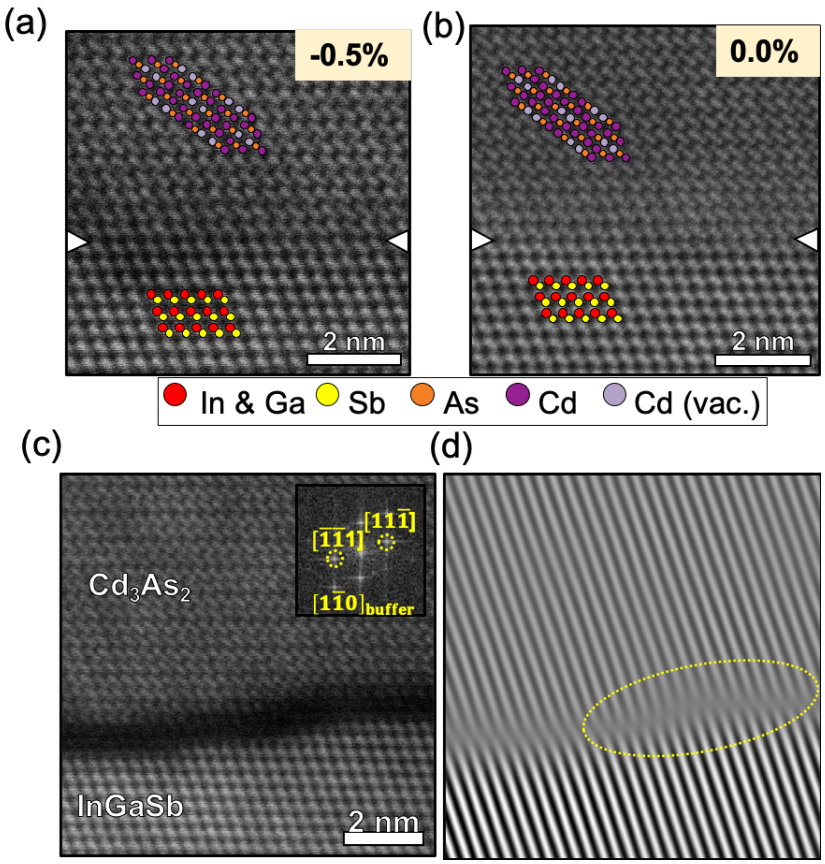


Figure 4.7: HAADF-STEm image for compressive strain (a), unstrained (b), and tensile strained (c) films. Figure. 4.7 (d) shows the inverse Fourier transform of Fig. 4.7 (c). (Image courtesy of Honggyu Kim).

### 4.2.3 Effect of strain on electrical transport

We studied and compared electrical transport in the films with different strains. Figure 4.8 shows the electron mobility for 30 nm thick films at 2 K as a function of the in-plane lattice parameter of the buffer layer. The dashed line indicates the lattice constant for relaxed films. The mobility was measured by the low field Hall effect ($0.5 < B < 0.5$ T). All films showed electrical transport from n-type carriers. The strain induced a large effect on carrier mobility. The carrier mobility changed by more than an order of magnitude from a compressive to (nominal) tensile strain direction. The mobility

dropped to 1,000 $cm^{-2}V^{-1}s^{-1}$ under 0.5% compressive strain. For the (nominal) tensile strain, the mobility increased monotonically up to 14,000 $cm^{-2}V^{-1}s^{-1}$. XRD measurements on 80 nm thick films indicate no tensile strain in the films. The change in carrier mobility under tensile strain is likely due to the residual strain in the films, since this transport study was done on 30 nm thick films and XRD was compared for the 80 nm thick films. This indicates the partial relaxation in the thin films. On further increase in the tensile strain (not shown in the figure), mobility dropped to 5,000 $cm^2$/V-sec indicating the full relaxation of the films.

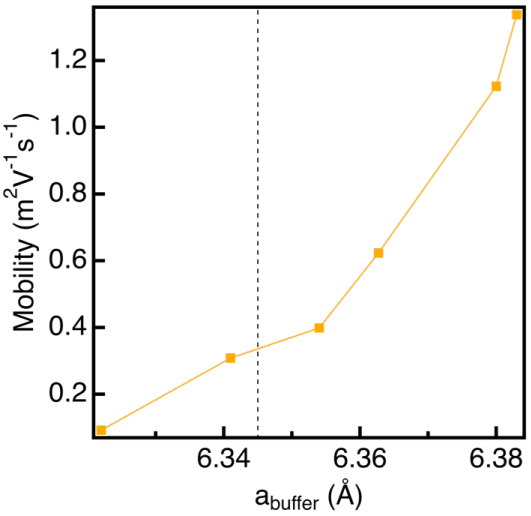


Figure 4.8: Electrical mobility of 30 nm thick $Cd_3As_2$ films grown on different buffer layer compositions. The horizontal axis shows the lattice parameters of the buffer layer calculated from out-of-plane XRD measurements. Mobilities are measured at 2 K along the $[\bar{1}10]$ of the buffer layer. The vertical dash line represents the lattice parameter for the relaxed $Cd_3As_2$ films grown on GaSb/GaAs.

Figure.4.9 shows longitudinal resistance ($R_{xx}$) and Hall resistance ($R_{xy}$) for 30 nm thick films under tensile and compressive strains. All films showed quantum Hall effect irrespective of the magnitude and type of strain. The carrier density measured from the frequency of these oscillations is in the range $4-7 \times 10^{11}$ $cm^{-2}$ for the films. We observed an increase in the carrier density measured by the low field Hall data. The carrier

density increased from $6.5\times10^{11}$ cm$^{-2}$ to $1.5\times10^{12}$ cm$^{-2}$ from tensile to compressive strain direction. The difference between the carrier density measured by quantum oscillations and low field Hall data increases in the compressive strain direction. For the tensile strained films, the carrier density measured by two different methods matched closely. This additional carrier in compressively strained films appeared to be from bulk states. A study shows that epitaxial strain modifies the band structure and impurity level for narrow band gap semiconductors [135]. In this study, we were limited to low-temperature transport due to a relatively small electrical bandgap of underlying $In_xGa_{(1-x)}Sb$ alloy. Thus, we were unable to find the thermal activation value for the additional carrier. Moreover, the Hall plateaus were not well-developed for compressively strained films, and the Landau level filling factors were not identified. Since the 2D carrier density was the same irrespective of the type of strain, this Landau level broadened due to low carrier mobility.

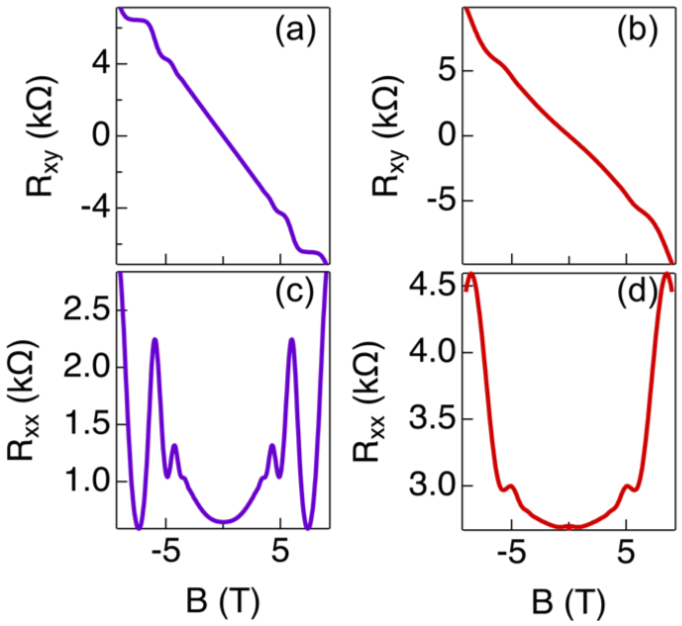


Figure 4.9: Hall resistance (a, b) and longitudinal resistance (c, d) of 30 nm thick $Cd_3As_2$ films grown under tensile (a, c) and compressive (b, d) strain.

In the electrical transport measurement, we observed a strong in-plane anisotropy. This anisotropy was measured as a non-zero voltage drop in the transverse direction at zero magnetic fields. This anisotropy was measured in all the films irrespective of type and strength of strain. The relaxed $Cd_3As_2$ films grown on GaSb and CdTe showed no transverse voltage at zero magnetic fields and an isotropic electrical transport was measured. For an anisotropic medium when the measurement axis is not in the direction of the principal axis, the longitudinal resistance ($R_{xx}$) and transverse resistance ($R_{xy}$) is given by the following equations:

$$R_{xx} = R_a \cos^2\theta + R_b \sin^2\theta,$$

$$R_{xy} = -R_a \sin\theta\cos\theta + R_b \sin\theta\cos\theta.$$

Where, $R_a$ and $R_b$ are the component of the resistivity tensor and $\theta$ is the angle of measurement with the principal resistivity axis.

To study this transport anisotropy, we fabricated a device with multiple Hall bars in different crystallographic directions. The size of Hall bars was 100 $\times$100 $\mu m^2$. Figure. 4.10 (a) shows the schematic of the Hall bar device. Figure.4.10 (b,c) show $R_{xx}$ and $R_{xy}$ for the devices at different crystallographic angles. The dashed line shows the fitting of the experimental data with the equation. The experimental data fit well with the equations, indicating the reduction in the crystalline symmetry by strain.

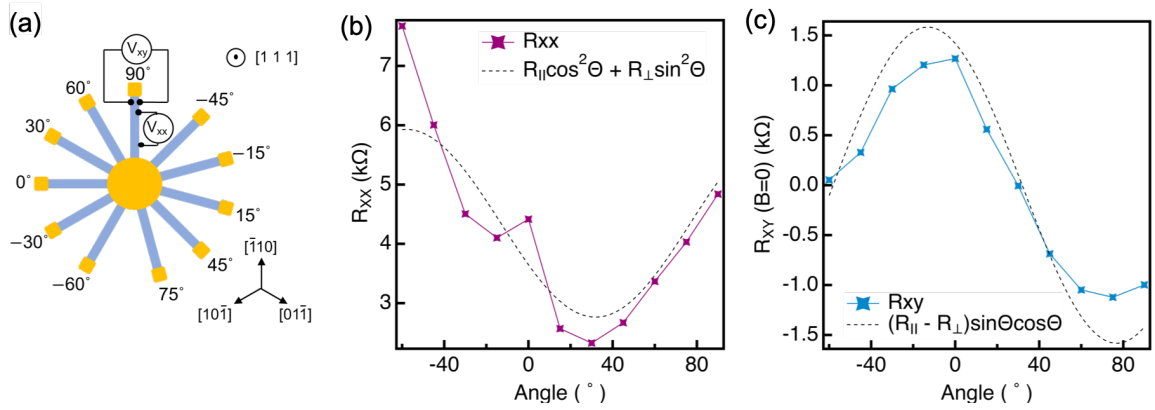


Figure 4.10: Figure. 4.10 (a) shows the schematic of the Hall bar device in different crystallographic directions. The crystallographic directions are shown for the substrates. Figure. 4.10 (b,c) show the longitudinal resistance (b) and transverse resistance (b) measured for different crystallographic directions. The dashed line shows the fitting by the equation shown in the figure.

### 4.2.4 Discussion

The observation of the quantum Hall effect in all the films confirmed the presence of robust 2D surface states. The strain breaks 4-fold symmetry and lifts the protection for bulk band crossing. However, a gapless surface state is expected due to an odd topological invariant $\mathbb{Z}_2$ number[7]. Additionally, in this thickness range (30 nm), the bulk would gap out due to quantum confinement. This finding gave additional confirmation that the quantum Hall effect in our thin films is not due to the Weyl orbit, that would require a gapless bulk state.

The in-plane anisotropy showed a reduction in the crystalline symmetry. The different vacancy ordered structures are indistinguishable in a 2D projection of the STEM images. Further, we observed an increase in carrier density and a decrease in carrier mobility in the compressive strain direction. Since all the films were grown under the same conditions, we expect similar defect densities in all the films. The decrease in mobility is most likely due to the change in the electronic band structure that would influence the carrier scattering

and effective mass. Moreover, films under the compressive strain showed additional 3D carriers. The films under (nominal) tensile strain showed only a 2D carriers with well-developed Hall plateaus. This indicates a change in bandgap by strain. A theoretical calculation for this specific biaxial strain would be helpful to explain this change in carrier density and mobility.

In summary, we demonstrated the growth of strained $Cd_3As_2$ films on the III-V substrates. The strain breaks the 4-fold symmetry and bulk electronic bands are gapped out. However, surface states remained gapless due to band inversion in the bulk. We can safely disregard the contribution of the Weyl orbit in the thin films for the quantum Hall effect. Our findings pave the way for the systematic study of Dirac semimetal under strain.

# Chapter 5

# In-plane angle dependence electronic transport

## 5.1 In-plane magnetotrasport

Observation of chiral anomaly and planar Hall effect in magnetotransport studies is used to identify the non-trivial electronic band structure of topological semimetals. The chiral anomaly is an imbalance of chiral current when an electric field is applied parallel to a magnetic field. As a result, a negative longitudinal magnetoresistance (NLMR) is observed. [51, 52]. This NLMR has been used as a signature for the Dirac and Weyl semimetals [53, 54, 55, 56, 57, 58, 59]. The planar Hall effect (PHE) is a result of induced in-plane anisotropy when a magnetic field is applied in-plane of the sample. The planar Hall effect has been predicted as another consequence of the chiral anomaly in topological semimetals[136, 137].

The chiral anomaly induced transport is from zeroth Landau level which is the lowest Landau level. As a result, the magnitude of NLMR due to chiral anomaly depends on the Fermi level. A robust NLMR is predicted even when the Fermi level is far from

the Weyl nodes [138]. Additionally, the Berry phase has been predicted to give NLMR and PHE for 3 D topological insulators[139, 140]. This NLMR and PHE are due to the non-zero Berry phase near the band edge of the bulk electronic band[139, 140]. In addition to these mechanisms (chiral anomaly and Berry phase), NLMR can originate due to different macroscopic effects such as current jetting, conductivity fluctuations, disorder [141, 142, 143, 144].

## 5.2 Anisotropic magnetoresistance and planar Hall effect

When a magnetic field is applied in-plane, an anisotropy in electrical transport originates due to a change in resistivity along and transverse to the magnetic field. As a result, the resistivity of the film depends on the angle between the magnetic field and current direction. Anisotropic magnetoresistance (AMR) and PHE can be given as longitudinal and transverse components of the anisotropic resistivity. Longitudinal resistance ($R_{xx}$) and transverse resistance ($R_{xy}$) follow the equations

$$R_{xx} = R_{\perp} - \Delta R \cos^2\theta, \qquad (1)$$

$$R_{xy} = -\Delta R \sin\theta \cos\theta. \qquad (2)$$

$R_{\perp}$ is the transverse resistance (B lies within the film plane and B$\perp$I) and $R_{\parallel}$ is the longitudinal resistance (B $\parallel$ I). $\Delta$R is given by $R_{\perp} - R_{\parallel}$ and describes the amplitude of the anisotropy. The sign and the amplitude of $\Delta$R depend on the dominating mechanism of the magnetoresistance. Equations (1) and (2) represent the anisotropic magnetoresistance (AMR) and planar Hall effect (PHE). There have been many reports on the obser-

vation of PHE in topological semimetal assigning this effect to chiral anomaly induced magnetoresistance[145, 146, 147, 148]. However, one must be careful before assigning the mechanism without considering the individual $R_{\perp}$ and $R_{\parallel}$. There are different mechanisms that could induce an anisotropic magnetoresistance and would result in the AMR and the PHE. For the case of a non-magnetic topological semimetal, we consider the three most likely ones and discuss their effect on measured quantities:

**Orbital Magnetoresistance (OMR)**: This magnetoresistance is due to Lorentz force that increases the resistance in the transverse direction ($R_{\perp}$) and has no effect on $R_{\parallel}$. In this case, the sign of $\Delta$R is positive. For topological semimetals, a large OMR is observed and explained by different mechanisms such as compensated n and p-type carriers [31, 32, 33], lifted backscattering protection [34] and quantum resistance due to linear band dispersion [35]. Thus, a large contribution in $\Delta$R is expected due to OMR.

**Chiral anomaly/Berry phase**: In this case, $R_{\parallel}$ decreases with the magnetic field, and $R_{\perp}$ remains unchanged. The magnetic field dependence of $R_{\parallel}$ depends on the quantum limit and type of scattering [149]. For the semiclassical case, $R_{\parallel}$ changes as $B^2$[52]. A positive $\Delta$ R is expected in AMR and PHE from this mechanism. For the case of a topological insulator, $R_{\parallel}$ decreases with the magnetic field due to the non-zero Berry phase. The Berry phase contribution strongly depends on the Fermi level and diverges when the Fermi level is near the band edge of bulk electronic bands[139, 150].

**Spin scattering**: For Dirac materials, the spin of the charge carriers is locked with the momentum that gives a well-defined chirality, and therefore, the backscattering is suppressed. By an in-plane magnetic field, this protection is lifted for the electron with perpendicular spin to the magnetic field. This results in the increase of $R_{\parallel}$ with the

magnetic field and $R_{\perp}$remains unaffected. The contribution from this scattering changes with the Fermi level and have a minimum contribution when the Fermi level is at the Dirac point. In the case of topological insulators where the electrical transport is from the two-dimensional surface states a negative $\Delta R$ is reported[151].

## 5.3 AMR and PHE study in $Cd_3As_2$

$Cd_3As_2$ is a viable candidate to study the different mechanisms that give rise to the planar Hall effect. It has gapless bulk and surface states with Dirac dispersion. These bulk states can be gapped by quantum confinement or strain converting this material into a topological insulator like electronic states [65, 67, 152, 121]. Additionally, the Fermi level can be tuned by annealing or surface passivation by $N^*$ plasma[110]. As mentioned above, the contribution from these different mechanisms depends on the Fermi level and bulk and surface electronic states. Therefore, $Cd_3As_2$ is the best candidate to study most of the above exotic mechanisms in one system by tuning the bulk and surface states with different Fermi levels.

We conduct a detailed in-plane magnetotransport study in $Cd_3As_2$ to isolate the contribution of surface and bulk electronic states. Samples with different thicknesses and different crystallographic orientations were studied to understand the mechanism contributing to AMR and PHE. 30-nm-thick and 60-nm-thick (112) oriented $Cd_3As_2$ films, as well as 45-nm-thick (001)-oriented $Cd_3As_2$ films were studied under different in-plane magnetic field. These three films have different surface states with a different contribution. Figure. 5.1 (a-c) shows a schematic of the bulk and surface electronic states for these three films. The 60-nm-thick $Cd_3As_2$ has gapless bulk and gapped surface states. Thus, the contribution from the spin scattering, chiral anomaly, and trivial magnetoresistance is expected in the magnetotransport of this film. The thin $Cd_3As_2$ has gapped bulk

electronic states but gapless surface states, independent of the film orientation. However, the surface states spectrum for two directions is quite different. The surface state for the thin (001) film is a point-like and an arc type for (112) thin film (shown in Fig. 5.1 (b) and 5.1 (c)).

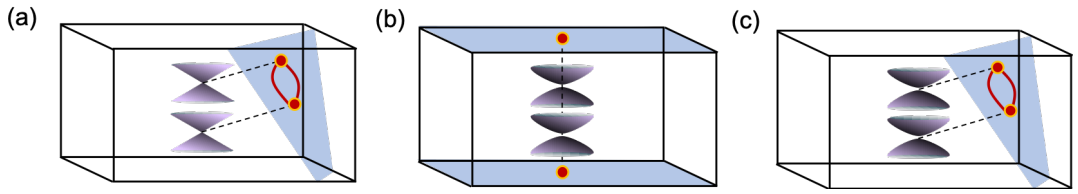


Figure 5.1: Schematic of surface and bulk electronic states for (112)-oriented 60 nm (a), (001)-oriented 45 nm (b) and (112)-oriented 30 nm (c) $Cd_3As_2$ films.

Figure. 5.2 shows the longitudinal resistance ($R_{xx}$) and Hall resistance ($R_{xy}$) for (112)-oriented 60 nm (a) and 30 nm (b) thick $Cd_3As_2$ films after growth. A non-linear Hall resistance at the high magnetic field is observed. The fitting of magnetoresistance by 2-carrier model gives n-type and p-type carriers with carrier mobility of 12,400 $cm^{-2}V^{-1}s^{-1}$ and 180 $cm^{-2}V^{-1}s^{-1}$ and sheet density of $2.9\times10^{11}$ $cm^{-2}$ and $1.3\times10^{12}$ $cm^{-2}$ respectively.

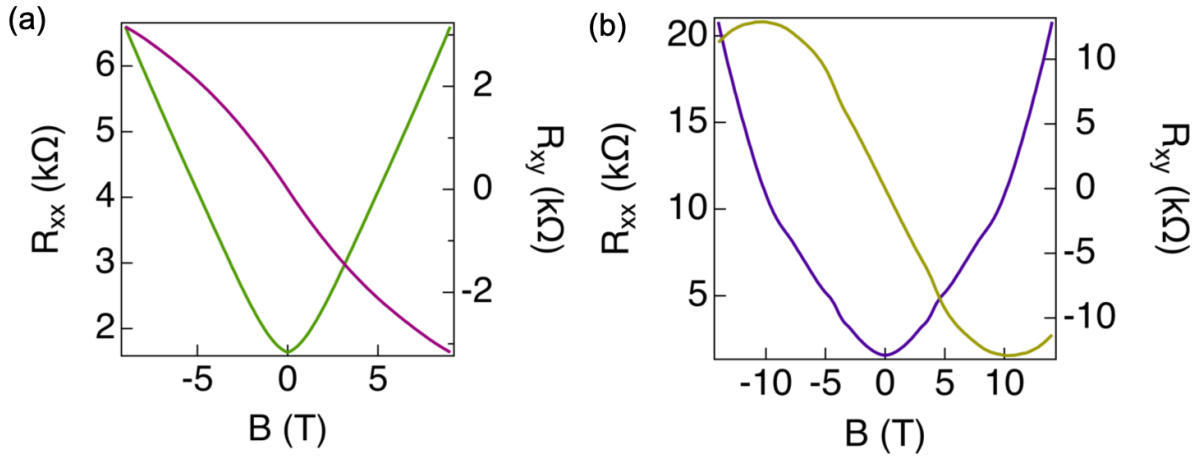


Figure 5.2: Longitudinal resistance ($R_{xx}$) and Hall resistance ($R_{xy}$) for (112)-oriented 60 nm thick (a) and 30 nm (b) thick films at low Fermi level.

Previously, we showed that the exposure of low energetic $N^*$ plasma eliminates the

hole transport and the 2D quantum oscillations were observed[110]. In our experiment, we measured the in-plane magnetoresistance for as-grown films that have low Fermi level. These measurements were compared with $N^*$ plasma clean thick (112) $Cd_3As_2$ (001) $Cd_3As_2$ and an annealed (112) $Cd_3As_2$ films with higher Fermi level. The annealing of the sample at 350 K for 20 minutes has the same effect as $N^*$ plasma exposure. Figure.5.3 shows the longitudinal resistance ($R_{xx}$) and Hall resistance ($R_{xy}$) for (112)-oriented 60 nm (a), (001)-oriented 45 nm (b), and (112)-oriented 30 nm (b) thick $Cd_3As_2$ films after cleaning/annealing. Thin (112) and (001) films show the quantum Hall effect as a signature of 2D transport (Fig.5.3 (b) (c)). 60 nm thick (112)-oriented films show 2D quantum oscillations from the surface state with a background magnetoresistance from the bulk states(Fig.5.3 (a)).

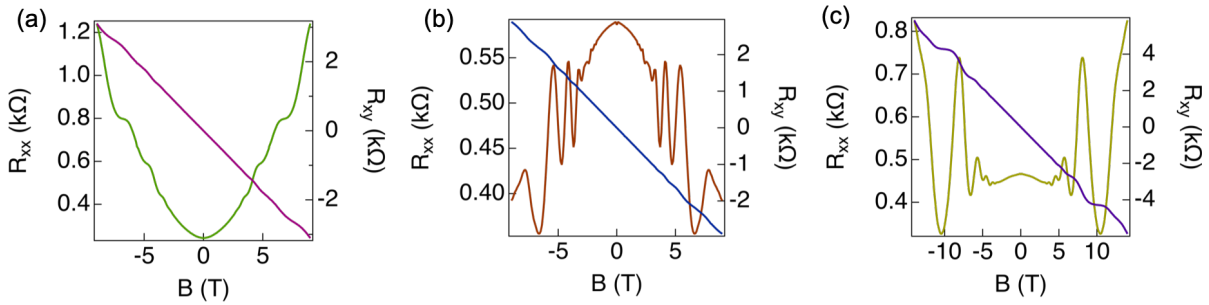


Figure 5.3: Longitudinal resistance ($R_{xx}$) and Hall resistance ($R_{xy}$) for (112)-oriented 60 nm (a), (001)-oriented 45 nm (b) and (112)-oriented 30 nm (c) $Cd_3As_2$ films after cleaning/annealing.

Figure.5.4 shows the measurement geometry used to study the AMR and PHE in the films. Measurements were done on 100×100 $\mu m^2$ Hall bar with the magnetic field rotated in the plane of the film. The longitudinal magnetoresistance ($R_{xx}$) and transverse resistance ($R_{xy}$) were measured as a function of the angle of rotation. The data for the PHE and AMR was symmetrized to eliminate the contribution from the Hall resistance due to misalignment that gives an out-of-plane component of the magnetic field. This Hall resistance is antisymmetric and can be eliminated by the symmetrization of PHE data.

For the AMR, this component also follows the $\cos^2\phi$ behaviors with a different phase $\phi$. We would also specify that the value of $\Delta$R from the individual fitting of Eq. (1) and (2) gives the same value that eliminates the possibility of the out-of-plane component in AMR due to misalignment. Thus, all the $\Delta$R discussed further are obtained by the simultaneous fitting of AMR and PHE by Eq. (1) and (2).

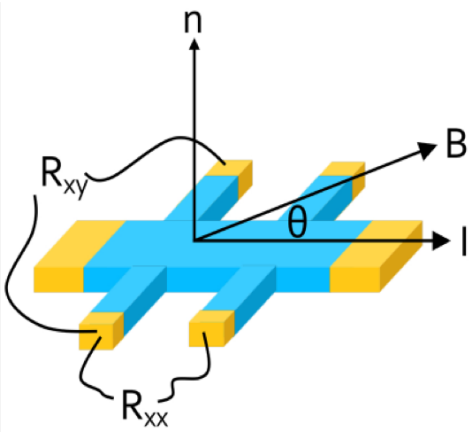


Figure 5.4: The measurement geometry for the AMR and PHE measurements.

Figure.5.5 shows the $R_{xx}$ (AMR) and $R_{xy}$ (PHE) at the different in-plane angle for (112)-oriented 60 nm thick $Cd_3As_2$ film. Figure. 5.5 (a) and (b) show the AMR and PHE for the lower Fermi level. The value of $\Delta$R approaches up to 50% for thick (112) films. In the earlier report, this large value of $\Delta$R is assigned solely to the chiral anomaly [145, 146, 147, 148]. However, when we consider the change in the $R_{xx}$ at 0° ($R_{\parallel}$) and 90° ($R_{\perp}$) separately we observe these resistance change in different directions, and $\Delta$R shows the combined effect. $R_{\parallel}$ reduces with an increasing magnetic field related to chiral anomaly or Berry phase induced NLMR. The mechanism for this NLMR is discussed in the later section. The $R_{\perp}$ increase with the magnetic field due to OMR. The sign of $\Delta$R is positive irrespective of the mechanisms. The same measurements were done for samples with a higher Fermi level. The in-plane magnetoresistance shows a drastic change in the

behavior (Fig.5.5 (c) (d)). The amplitude of PHE ($\Delta$R) dropped significantly and AMR showed a complex behavior with the magnetic field.

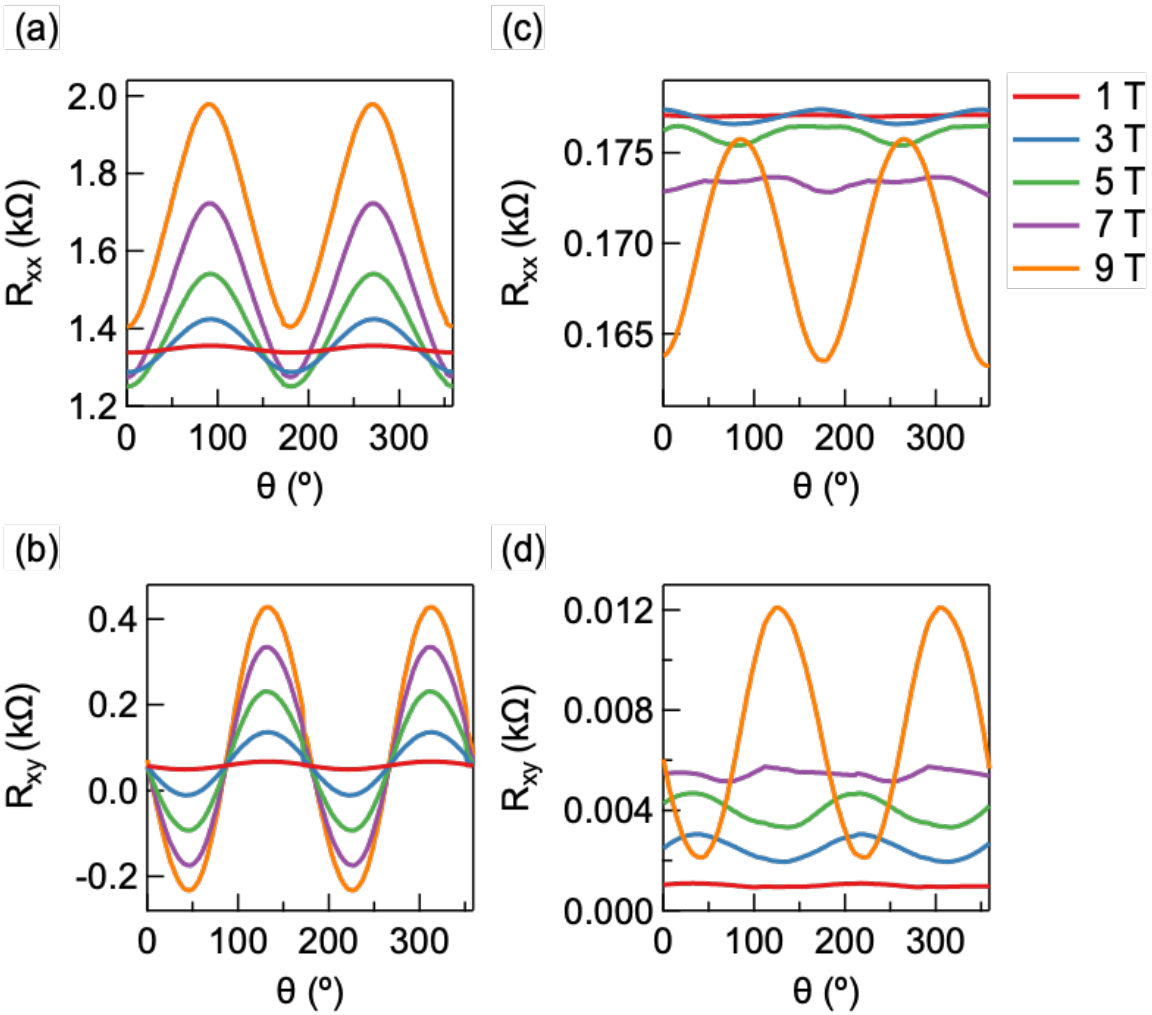


Figure 5.5: AMR (a, c) and PHE (b, d) for the (112)-oriented 60 nm thick $Cd_3As_2$ film at the low (left) and the high (right) Fermi level.

To get a clear picture and distinguish the different effects we plot $R_{\perp}$, $R_{\parallel}$, and $\Delta$R vs magnetic field (Fig. 5.6). The resistances are normalized to $R_{\parallel}$ at 1 T. Figures. 5.6(a) and 5.6(b) are for the (112) oriented 60 nm thick films for which the whole data is

shown in Fig.5.5. Figure 5.6(c) and 5.6(d) show $R_{\perp}$ and $R_{\parallel}$ with $\Delta R$ for the thin (001)-oriented film for lower and higher Fermi level. In the case of lower Fermi level, the film shows a very large negative magnetoresistance up-to 35% seen in the $R_{\parallel}$ with an OMR contribution in $R_{\perp}$. This AMR and PHE are similar to the thick (112) film. Figure. 5.6(e) and 5.6(f) show the AMR and PHE for the thin (112) film for lower and higher Fermi level. For the lower Fermi level, $R_{\perp}$ and $R_{\parallel}$ both show positive magnetoresistance with different scaling that gives an overall positive AMR.

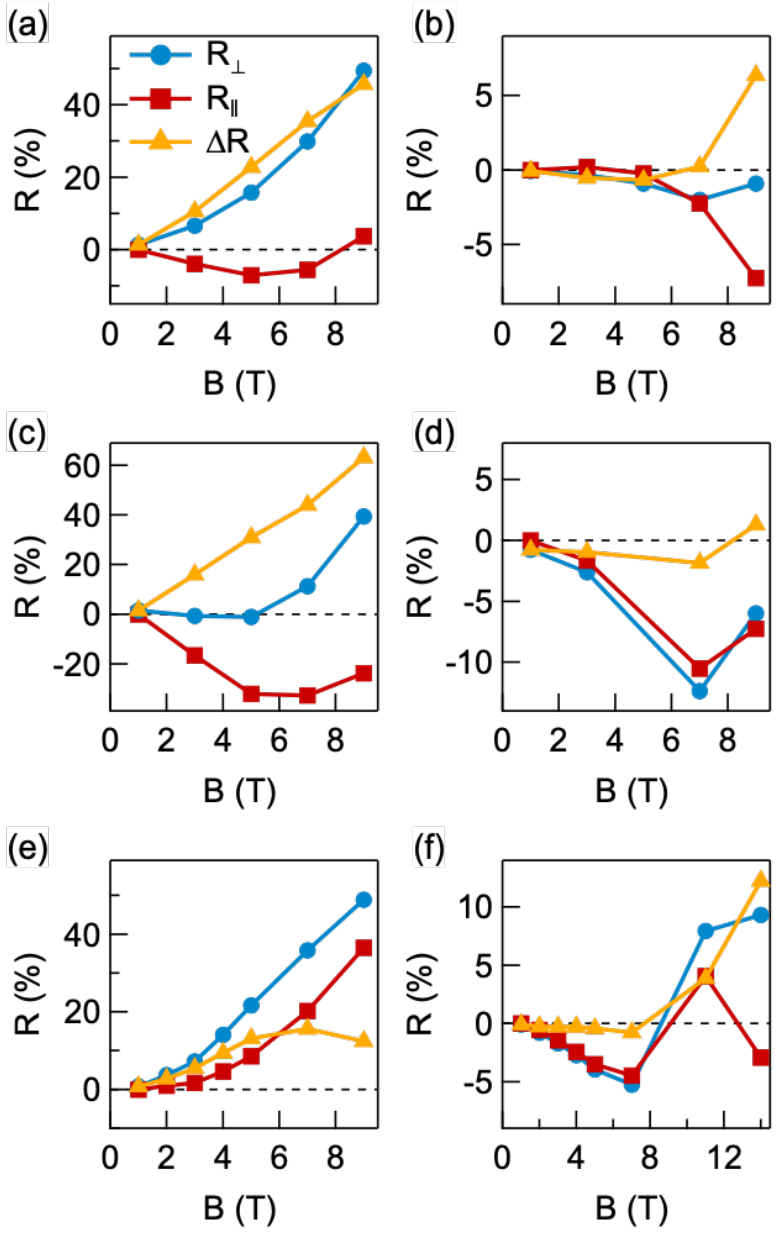


Figure 5.6: $R_{\perp}$, $R_{\parallel}$ and $\Delta R$ as a function of B for (112)-oriented 60 nm thick $Cd_3As_2$ (a, b), (001)-oriented 45 nm thick $Cd_3As_2$ (c, d) and (112)-oriented 30 nm thick $Cd_3As_2$ (e, f). The left column shows the data for the low Fermi level and the right column shows the data for the high Fermi level.

## 5.4 Discussion

We observed AMR and PHE in our films as a combined effect by multiple mechanisms. Magnetoresistance behavior is highly sensitive to the Fermi level. This indicates that the origin of AMR and PHE is not due to the macroscopic effects such as disorder, conductivity fluctuation. For the low Fermi level, we observed a negative magnetoresistance for 60 nm and 45 nm thick films. Conductivity fluctuation as an origin for NLMR is unlikely for these films because the (001) films show stronger NLMR than thick (112) $Cd_3As_2$ films. The NLMR due to conductivity fluctuation is large for the thick films in comparison to thin films [66]. Further, the current jetting can be excluded based on the fact that all the measurements were done in Hall bar geometry and the size of metal contact pads are larger than the Hall bar width (see Fig.5.4).

At the low Fermi level, p-type carrier from the bulk and n-type carrier from the surface states contribute to the electrical transport. This indicates that the Fermi level for the depleted films is at the edge of the bulk electronic band. The Berry phase diverges at the band edge and therefore, a larger NLMR is observed due to chiral anomaly or Berry phase. This NLMR disappears for the 30 nm thick film, due to a large bandgap in the bulk. Additionally for this film, a positive $R_{\parallel}$ is observed. The origin of this positive $R_{\parallel}$ is not completely understood, however, can be postulated as an increase in resistance due to lifted backscattering protection. Moreover, all of these films show an increase in $R_{\perp}$ due to OMR. This contribution from OMR is large for low Fermi level due to the presence of n and p-type carriers. Thus, the total PHE in the films is due to the total effect and as a result, a large value of $\Delta R$ is observed.

For the high Fermi level, the amplitude of $\Delta R$ decreased significantly. The chiral anomaly and Berry phase contribution is reduced due to high Fermi level. Moreover, a reduction in OMR is also expected due to transport from n-type carriers. For 45 nm

and 30 nm thick films, the carrier transport is by high mobility surface carrier and the transport from quantized Landau level is observed at a relatively low magnetic field. In the AMR and PHE measurements, $R_{\perp}$, $R_{\parallel}$ follows each other closely with the magnetic field for these films. This Landau quantization and change in scattering significantly affect the AMR and PHE behavior[153]. Therefore, it is hard to draw any conclusion for these films for high Fermi level. A further in-plane magnetotransport study with an electrostatic gating would be helpful to understand this behavior.

In conclusion, we showed that AMR and PHE are very sensitive to the Fermi level and film thickness. Chiral anomaly, Berry phase, and OMR have large contribution when transport is from the bulk electronic states. We observed AMR and PHE as a combined effect due to multiple mechanisms.

# Chapter 6

# Summary and Outlook

## 6.1 Summary

In this thesis, I discussed the epitaxial growth and magnetotransport study of $Cd_3As_2$. The films were grown with different crystallographic orientations ((112) and (001)) on single crystal III-V and II-VI substrates. The $Cd_3As_2$ film quality was found to be greatly influenced by the structural quality of the underlying layer. A combination of chemical etch with $H_2$ plasma was used to find the optimal surface treatment to remove the native oxide from the substrates. The structural study by XRD and HAADF-STEM confirmed the epitaxial growth of $Cd_3As_2$ in the low-temperature Dirac semimetal phase.

Structural quality and electrical transport were further improved by designing the buffer layer and developing the growth of an *in situ* GaSb capping layer. Buffer layers with different structures were compared for their effectiveness for dislocation filtering, and their effect on electrical transport was studied. The electrical transport study shows that the Hall mobility of the carriers from bulk electronics states was not limited by the misfit dislocation density in the films, however, the Hall mobility of the carriers from surface electronic states degrades with the increase in the misfit dislocation density. Further,

the growth of the capping layer was developed to protect the electrical transport from surface electronic states. Capped films showed an improvement in Hall mobility.

The effect of quantum confinement and epitaxial strain was studied on bulk and surface electronic transport. The contributions in total electronic transport by surface and bulk states were distinguished by performing electrical characterization in films with different thicknesses. Thick films (>70 nm) showed two different n-type carriers indicated the contribution from two electronic states. However, thin films showed a single carrier transport, and the quantum Hall effect was observed, indicated 2D transport. This 2D transport is intrinsic to $Cd_3As_2$ and from surface electronic states. Consistent with theoretical predictions, this study showed the quantum confinement effect lead to a bulk bandgap opening while surface states remained gapless. Further, we observed robust gapless surface states under biaxial strain. The epitaxial strain in (112)-oriented films breaks the 4-fold symmetry and as a result, the bulk electronic band gapped out. We further showed that epitaxial strain significantly affects the Hall mobility and reduces the crystal symmetry. This lowering in the crystal symmetry was observed by the in-plane electrical transport.

The in-plane magnetotransport study was done to investigate the anisotropic magnetoresistance (AMR) and planar Hall effect (PHE) in the $Cd_3As_2$. The films with different thicknesses, orientations, and Fermi levels were compared to distinguish the contribution from different mechanisms giving AMR and PHE in the $Cd_3As_2$ films. The AMR and PHE were observed as a combined effect from mechanisms such as OMR, spin scattering, chiral anomaly, and Berry phase.

## 6.2 Future work

The high-quality growth of $Cd_3As_2$ with great control of thickness and crystallographic orientation enabled us to understand and engineer the electronic structure. The study can be further expanded in many directions discussed below.

### 6.2.1 Growth study

The film growth can be further studied by Cd and As co-depositions. In our study, we obtained the highest mobility of 40,000 for 1.3$\mu$m thick $Cd_3As_2$ film. This mobility is low in comparison to previously reported for the single crystals study[34]. The dislocation study showed the insensitivity of carrier mobility by misfit dislocations. This finding indicated that mobility is insensitive due to topological protection, or is limited by some other mechanism such as point defects due to As or Cd deficiency. This can be further addressed by co-deposition of As with $Cd_3As_2$, or Cd and As co-deposition. This growth study would further provide insight about mobility limiting mechanisms in the bulk of $Cd_3As_2$.

### 6.2.2 Selective area growth

The selective area growth of $Cd_3As_2$ can be developed to study the quantum transport in nanostructures. Growth of nanowire by selective area would open the door for proximity effect study, which generally requires a nanoscale device due to small coherence length of cooper pairs. Transport measurements in nanoscale devices are very sensitive to interface and device fabrication steps. Selective area growth would provide a way to grow nanostructures of $Cd_3As_2$. In my preliminary study, I have achieved the selective growth of $Cd_3As_2$ on GaSb/GaAs. The Hall bar structure was patterned on the GaSb/GaAs substrates by using $SiO_2$. In my study, I found that $Cd_3As_2$ does not grow on $SiO_2$. This

method can be further explored to develop the growth of nanostructures.

### 6.2.3 Utrathin films and Multilayers

Theoretical study predicted quantum spin Hall insulator[154] states in 5-10 nm thick $Cd_3As_2$ films[7]. The capping layer enabled us to measure the transport in films of 10 nm. The transport study on ultra-thin films (<10 nm) would be interesting to explore this new exotic phase in $Cd_3As_2$.

The capping layer further opens the door for heterostructure. The multilayer of $Cd_3As_2$ films can be grown with the separation layer grown by migration enhanced epitaxy. The thickness of this layer can further systematically change to study the effect of interaction between two surface states of $Cd_3As_2$. This study can be expanded for different crystallographic orientations of $Cd_3As_2$ to explore the interaction between the Fermi arcs.

# Bibliography


[1] A. A. Burkov, *Topological semimetals*, *Nature Materials* **15** (2016), no. 11 1145–1148.

[2] H. Weyl, *Elektron und gravitation. i*, *Zeitschrift für Physik* **56** (1929), no. 5 330–352.

[3] G. E. Volovik, *Momentum space topology of fermion zero modes brane*, *Journal of Experimental and Theoretical Physics Letters* **75** (2002), no. 2 55–58.

[4] P. A. M. Dirac, *The quantum theory of the electron*, *Proceedings of the Royal Society of London. Series A, Containing Papers of a Mathematical and Physical Character* **117** (1928), no. 778 610–624.

[5] S. M. Young, S. Zaheer, J. C. Y. Teo, C. L. Kane, E. J. Mele, and A. M. Rappe, *Dirac semimetal in three dimensions*, *Phys. Rev. Lett.* **108** (Apr, 2012) 140405.

[6] B.-J. Yang and N. Nagaosa, *Classification of stable three-dimensional dirac semimetals with nontrivial topology*, *Nature Communications* **5** (2014), no. 1 4898.

[7] Z. Wang, H. Weng, Q. Wu, X. Dai, and Z. Fang, *Three-dimensional dirac semimetal and quantum transport in $cd_3as_2$*, *Phys. Rev. B* **88** (Sep, 2013) 125427.

[8] Z. Wang, Y. Sun, X.-Q. Chen, C. Franchini, G. Xu, H. Weng, X. Dai, and Z. Fang, *Dirac semimetal and topological phase transitions in $A_3bi$ ($a = Na, k, rb$)*, *Phys. Rev. B* **85** (May, 2012) 195320.

[9] G. A. Steigmann and J. Goodyear, *The crystal structure of $Cd_3As_2$*, *Acta Crystallographica Section B* **24** (Aug, 1968) 1062–1067.

[10] M. N. Ali, Q. Gibson, S. Jeon, B. B. Zhou, A. Yazdani, and R. J. Cava, *The crystal and electronic structures of cd3as2, the three-dimensional electronic analogue of graphene*, *Inorganic Chemistry* **53** (2014), no. 8 4062–4067. PMID: 24679042.

[11] H. Kim, M. Goyal, S. Salmani-Rezaie, T. Schumann, T. N. Pardue, J.-M. Zuo, and S. Stemmer, *Point group symmetry of cadmium arsenide thin films*

*determined by convergent beam electron diffraction*, *Phys. Rev. Materials* **3** (Aug, 2019) 084202.

[12] R. Sankar, M. Neupane, S. Y. Xu, C. J. Butler, I. Zeljkovic, I. Panneer Muthuselvam, F. T. Huang, S. T. Guo, S. K. Karna, M. W. Chu, W. L. Lee, M. T. Lin, R. Jayavel, V. Madhavan, M. Z. Hasan, and F. C. Chou, *Large single crystal growth, transport property and spectroscopic characterizations of three-dimensional dirac semimetal cd3as2*, *Scientific Reports* **5** (2015), no. 1 12966.

[13] A. Pietraszko and K. Łukaszewicz, *A refinement of the crystal structure of $\alpha$"-$Cd_3As_2$*, *Acta Crystallographica Section B* **25** (May, 1969) 988–990.

[14] A. Pietraszko and K. ukaszewicz, *Thermal expansion and phase transitions of cd3as2 and zn3as2*, *physica status solidi (a)* **18** (1973), no. 2 723–730, [https://onlinelibrary.wiley.com/doi/pdf/10.1002/pssa.2210180234].

[15] E. Arushanov, *Crystal growth and characterization of ii3v2 compounds*, *Progress in Crystal Growth and Characterization* **3** (1980), no. 2 211 – 255.

[16] E. O. Kane, *Band structure of indium antimonide*, *Journal of Physics and Chemistry of Solids* **1** (1957), no. 4 249 – 261.

[17] D. Armitage and H. Goldsmid, *Non-parabolic conduction band in cd3as2*, *Physics Letters A* **28** (1968), no. 2 149 – 150.

[18] L. M. Rogers, R. M. Jenkins, and A. J. Crocker, *Transport and optical properties of the cd3-xZnxAs2 alloy system*, *Journal of Physics D: Applied Physics* **4** (jun, 1971) 793–809.

[19] M. J. Aubin, L. G. Caron, and J. P. Jay-Gerin, *Band structure of cadmium arsenide at room temperature*, *Phys. Rev. B* **15** (Apr, 1977) 3872–3878.

[20] L. G. Caron, J. P. Jay-Gerin, and M. J. Aubin, *Energy-band structure of* $\mathrm{cd_3as_2}$ *at low temperatures and the dependence of the direct gap on temperature and pressure*, *Phys. Rev. B* **15** (Apr, 1977) 3879–3887.

[21] J. P. Jay-Gerin and A. A. Lakhani, *The dependence ofg-factor on the electron concentration in cadmium arsenide at low temperatures*, *Journal of Low Temperature Physics* **28** (1977), no. 1 15–20.

[22] H. Kildal, *Band structure of cdge*$\mathrm{as_2}$ *near* $\vec{\mathrm{k}}= 0$, *Phys. Rev. B* **10** (Dec, 1974) 5082–5087.

[23] J. Bodnar, *Band structure of cd _3 as _2 from shubnikov-de haas and de haas-van alphen effects*, *arXiv preprint arXiv:1709.05845* (2017).

[24] A. Mosca Conte, O. Pulci, and F. Bechstedt, *Electronic and optical properties of topological semimetal cd3as2*, *Scientific Reports* **7** (2017), no. 1 45500.

[25] X. Wan, A. M. Turner, A. Vishwanath, and S. Y. Savrasov, *Topological semimetal and fermi-arc surface states in the electronic structure of pyrochlore iridates*, *Phys. Rev. B* **83** (May, 2011) 205101.

[26] H. Weng, C. Fang, Z. Fang, B. A. Bernevig, and X. Dai, *Weyl semimetal phase in noncentrosymmetric transition-metal monophosphides*, *Phys. Rev. X* **5** (Mar, 2015) 011029.

[27] S.-Y. Xu, I. Belopolski, N. Alidoust, M. Neupane, G. Bian, C. Zhang, R. Sankar, G. Chang, Z. Yuan, C.-C. Lee, S.-M. Huang, H. Zheng, J. Ma, D. S. Sanchez, B. Wang, A. Bansil, F. Chou, P. P. Shibayev, H. Lin, S. Jia, and M. Z. Hasan, *Discovery of a weyl fermion semimetal and topological fermi arcs*, *Science* **349** (2015), no. 6248 613–617, [https://science.sciencemag.org/content/349/6248/613.full.pdf].

[28] W. Witczak-Krempa, G. Chen, Y. B. Kim, and L. Balents, *Correlated quantum phenomena in the strong spin-orbit regime*, *Annual Review of Condensed Matter Physics* **5** (2014), no. 1 57–82.

[29] M. Kargarian, M. Randeria, and Y.-M. Lu, *Are the surface fermi arcs in dirac semimetals topologically protected?*, *Proceedings of the National Academy of Sciences* **113** (2016), no. 31 8648–8652, [https://www.pnas.org/content/113/31/8648.full.pdf].

[30] E. H. Hall, *On a new action of the magnet on electric currents*, *American Journal of Mathematics* **2** (1879), no. 3 287–292.

[31] C. Shekhar, A. K. Nayak, Y. Sun, M. Schmidt, M. Nicklas, I. Leermakers, U. Zeitler, Y. Skourski, J. Wosnitza, Z. Liu, Y. Chen, W. Schnelle, H. Borrmann, Y. Grin, C. Felser, and B. Yan, *Extremely large magnetoresistance and ultrahigh mobility in the topological weyl semimetal candidate nbp*, *Nature Physics* **11** (2015), no. 8 645–649.

[32] W. Gao, N. Hao, F.-W. Zheng, W. Ning, M. Wu, X. Zhu, G. Zheng, J. Zhang, J. Lu, H. Zhang, C. Xi, J. Yang, H. Du, P. Zhang, Y. Zhang, and M. Tian, *Extremely large magnetoresistance in a topological semimetal candidate pyrite* $\mathrm{ptbi}_2$, *Phys. Rev. Lett.* **118** (Jun, 2017) 256601.

[33] M. N. Ali, J. Xiong, S. Flynn, J. Tao, Q. D. Gibson, L. M. Schoop, T. Liang, N. Haldolaarachchige, M. Hirschberger, N. P. Ong, and R. J. Cava, *Large, non-saturating magnetoresistance in wte2*, *Nature* **514** (2014), no. 7521 205–208.

[34] T. Liang, Q. Gibson, M. N. Ali, M. Liu, R. J. Cava, and N. P. Ong, *Ultrahigh mobility and giant magnetoresistance in the dirac semimetal cd3as2*, *Nature Materials* **14** (2015), no. 3 280–284.

[35] A. A. Abrikosov, *Quantum magnetoresistance*, *Phys. Rev. B* **58** (Aug, 1998) 2788–2794.

[36] N. W. Ashcroft, *Solid state physics*. Holt, Rinehart and Winston, New York ; London, 1976.

[37] H. Bruus and K. Flensberg, *Many-body quantum theory in condensed matter physics - an introduction*. Oxford University Press, United States, 2004.

[38] T. Ando, A. B. Fowler, and F. Stern, *Electronic properties of two-dimensional systems*, *Rev. Mod. Phys.* **54** (Apr, 1982) 437–672.

[39] T. Ando, *Screening effect and impurity scattering in monolayer graphene*, *Journal of the Physical Society of Japan* **75** (2006), no. 7 074716, [https://doi.org/10.1143/JPSJ.75.074716].

[40] E. H. Hwang, S. Adam, and S. D. Sarma, *Carrier transport in two-dimensional graphene layers*, *Phys. Rev. Lett.* **98** (May, 2007) 186806.

[41] K. Nomura and A. H. MacDonald, *Quantum transport of massless dirac fermions*, *Phys. Rev. Lett.* **98** (Feb, 2007) 076602.

[42] L. Landau, *Diamagnetismus der metalle*, *Zeitschrift für Physik* **64** (1930), no. 9-10 629–637.

[43] A. Pippard, *The Dynamics of Conduction Electrons*. Documents on modern physics. Gordon and Breach, 1965.

[44] M. V. Kartsovnik, *High magnetic fields: a tool for studying electronic properties of layered organic metals*, *Chemical Reviews* **104** (2004), no. 11 5737–5782, [https://doi.org/10.1021/cr0306891]. PMID: 15535667.

[45] I. Lifshitz and L. Kosevich, *On the theory of the shubnikov-de haas effect*, *Sov. Phys. JETP* **6** (1958) 67–77.

[46] I. Lifshitz and A. Kosevich, *Theory of magnetic susceptibility in metals at low temperatures*, *Sov. Phys. JETP* **2** (1956), no. 4 636–645.

[47] D. Shoenberg, *Magnetic Oscillations in Metals*. Cambridge Monographs on Physics. Cambridge University Press, 1984.

[48] A. Pariari, P. Dutta, and P. Mandal, *Probing the fermi surface of three-dimensional dirac semimetal* $cd_3as_2$ *through the de haas–van alphen technique*, *Phys. Rev. B* **91** (Apr, 2015) 155139.

[49] J. S. Bell and R. Jackiw, *A pcac puzzle: 0in the -model*, *Il Nuovo Cimento A (1965-1970)* **60** (1969), no. 1 47–61.

[50] S. L. Adler, *Axial-vector vertex in spinor electrodynamics*, *Phys. Rev.* **177** (Jan, 1969) 2426–2438.

[51] H. Nielsen and M. Ninomiya, *The adler-bell-jackiw anomaly and weyl fermions in a crystal*, *Physics Letters B* **130** (1983), no. 6 389 – 396.

[52] D. T. Son and B. Z. Spivak, *Chiral anomaly and classical negative magnetoresistance of weyl metals*, *Phys. Rev. B* **88** (Sep, 2013) 104412.

[53] X. Huang, L. Zhao, Y. Long, P. Wang, D. Chen, Z. Yang, H. Liang, M. Xue, H. Weng, Z. Fang, X. Dai, and G. Chen, *Observation of the chiral-anomaly-induced negative magnetoresistance in 3d weyl semimetal taas*, *Phys. Rev. X* **5** (Aug, 2015) 031023.

[54] J. Xiong, S. K. Kushwaha, T. Liang, J. W. Krizan, M. Hirschberger, W. Wang, R. J. Cava, and N. P. Ong, *Evidence for the chiral anomaly in the dirac semimetal na3bi*, *Science* **350** (2015), no. 6259 413–416, [https://science.sciencemag.org/content/350/6259/413.full.pdf].

[55] H. Li, H. He, H.-Z. Lu, H. Zhang, H. Liu, R. Ma, Z. Fan, S.-Q. Shen, and J. Wang, *Negative magnetoresistance in dirac semimetal cd3as2*, *Nature Communications* **7** (2016), no. 1 10301.

[56] A. C. Niemann, J. Gooth, S.-C. Wu, S. Bäßler, P. Sergelius, R. Hühne, B. Rellinghaus, C. Shekhar, V. Süß, M. Schmidt, C. Felser, B. Yan, and K. Nielsch, *Chiral magnetoresistance in the weyl semimetal nbp*, *Scientific Reports* **7** (2017), no. 1 43394.

[57] C. Zhang, E. Zhang, W. Wang, Y. Liu, Z.-G. Chen, S. Lu, S. Liang, J. Cao, X. Yuan, L. Tang, Q. Li, C. Zhou, T. Gu, Y. Wu, J. Zou, and F. Xiu, *Room-temperature chiral charge pumping in dirac semimetals*, *Nature Communications* **8** (2017), no. 1 13741.

[58] C.-L. Zhang, S.-Y. Xu, I. Belopolski, Z. Yuan, Z. Lin, B. Tong, G. Bian, N. Alidoust, C.-C. Lee, S.-M. Huang, T.-R. Chang, G. Chang, C.-H. Hsu, H.-T. Jeng, M. Neupane, D. S. Sanchez, H. Zheng, J. Wang, H. Lin, C. Zhang, H.-Z. Lu, S.-Q. Shen, T. Neupert, M. Zahid Hasan, and S. Jia, *Signatures of the adler–bell–jackiw chiral anomaly in a weyl fermion semimetal*, *Nature Communications* **7** (2016), no. 1 10735.

[59] S. Nishihaya, M. Uchida, Y. Nakazawa, K. Akiba, M. Kriener, Y. Kozuka, A. Miyake, Y. Taguchi, M. Tokunaga, and M. Kawasaki, *Negative*

*magnetoresistance suppressed through a topological phase transition in* $(cd_{1-x}zn_x)_3as_2$ *thin films*, *Phys. Rev. B* **97** (Jun, 2018) 245103.

[60] A. C. Potter, I. Kimchi, and A. Vishwanath, *Quantum oscillations from surface fermi arcs in weyl and dirac semimetals*, *Nature Communications* **5** (2014), no. 1 5161.

[61] Y. Zhang, D. Bulmash, P. Hosur, A. C. Potter, and A. Vishwanath, *Quantum oscillations from generic surface fermi arcs and bulk chiral modes in weyl semimetals*, *Scientific Reports* **6** (2016), no. 1 23741.

[62] P. J. W. Moll, N. L. Nair, T. Helm, A. C. Potter, I. Kimchi, A. Vishwanath, and J. G. Analytis, *Transport evidence for fermi-arc-mediated chirality transfer in the dirac semimetal cd3as2*, *Nature* **535** (2016), no. 7611 266–270.

[63] C. Zhang, Y. Zhang, X. Yuan, S. Lu, J. Zhang, A. Narayan, Y. Liu, H. Zhang, Z. Ni, R. Liu, E. S. Choi, A. Suslov, S. Sanvito, L. Pi, H.-Z. Lu, A. C. Potter, and F. Xiu, *Quantum hall effect based on weyl orbits in cd3as2*, *Nature* **565** (2019), no. 7739 331–336.

[64] T. Schumann, M. Goyal, H. Kim, and S. Stemmer, *Molecular beam epitaxy of cd3as2 on a iii-v substrate*, *APL Materials* **4** (2016), no. 12 126110, [https://doi.org/10.1063/1.4972999].

[65] M. Goyal, L. Galletti, S. Salmani-Rezaie, T. Schumann, D. A. Kealhofer, and S. Stemmer, *Thickness dependence of the quantum hall effect in films of the three-dimensional dirac semimetal cd3as2*, *APL Materials* **6** (2018), no. 2 026105.

[66] T. Schumann, M. Goyal, D. A. Kealhofer, and S. Stemmer, *Negative magnetoresistance due to conductivity fluctuations in films of the topological semimetal* $Cd_3As_2$, *Phys. Rev. B* **95** (Jun, 2017) 241113.

[67] M. Goyal, H. Kim, T. Schumann, L. Galletti, A. A. Burkov, and S. Stemmer, *Surface states of strained thin films of the dirac semimetal* $cd_3as_2$, *Phys. Rev. Materials* **3** (Jun, 2019) 064204.

[68] M. Goyal, S. Salmani-Rezaie, T. N. Pardue, B. Guo, D. A. Kealhofer, and S. Stemmer, *Carrier mobilities of (001) cadmium arsenide films*, *APL Materials* **8** (2020), no. 5 051106.

[69] M. Goyal, D. A. Kealhofer, T. Schumann, and S. Stemmer, *Magnetoresistance effects in cadmium arsenide thin films*, *Applied Physics Letters* **117** (2020), no. 17 170601, [https://doi.org/10.1063/5.0031781].

[70] J. J. Dubowski and D. F. Williams, *Growth and properties of cd3as2 films prepared by pulsed-laser evaporation*, *Canadian Journal of Physics* **63** (1985), no. 6 815–818, [https://doi.org/10.1139/p85-131].

[71] J. Dubowski and D. Williams, *Growth of polycrystalline cd3as2 films on room temperature substrates by a pulsed-laser evaporation technique*, *Thin Solid Films* **117** (1984), no. 4 289 – 297.

[72] L. danowicz and S. Miotkowska, *Effect of deposition parameters on the structure of vacuum-evaporated cadmium arsenide films*, *Thin Solid Films* **29** (1975), no. 1 177 – 183.

[73] L. danowicz, S. Miotkowska, and M. Niedwied, *Structure, growth and crystallization effects in thin films of cadmium arsenide*, *Thin Solid Films* **34** (1976), no. 1 41 – 45.

[74] J. Jurusik and L. danowicz, *Electron microscope investigations of the growth morphology of cadmium arsenide films vacuum deposited at various substrate temperatures*, *Thin Solid Films* **67** (1980), no. 2 285 – 292.

[75] H. Matsunami and T. Tanaka, *Cd3as2thin film magnetoresistor*, *Japanese Journal of Applied Physics* **10** (may, 1971) 600–603.

[76] M. Din and R. Gould, *Van der pauw resistivity measurements on evaporated thin films of cadmium arsenide, cd3as2*, *Applied Surface Science* **252** (2006), no. 15 5508 – 5511. Proceedings of the Eight International Conference on Atomically Controlled Surfaces, Interfaces and Nanostructures and the Thirteenth International Congress on Thin Films.

[77] J. Portal, M. Abdel Moaty, W. danowicz, and L. danowicz, *The shubnikov-de haas effect in thin films of cd3as2 i: Crystalline films*, *Thin Solid Films* **76** (1981), no. 4 391 – 400.

[78] M. Gould, R.D.Din, *Capacitance variations in cd3as2 thin film sandwich structures*, *Superficies y vaco* (1999).

[79] W. danowicz, L. danowicz, J. Portal, and S. Askenazy, *Shubnikov-de haas effect in thin films of cadmium arsenide*, *Thin Solid Films* **61** (1979), no. 1 41 – 50.

[80] L. P. He, X. C. Hong, J. K. Dong, J. Pan, Z. Zhang, J. Zhang, and S. Y. Li, *Quantum transport evidence for the three-dimensional dirac semimetal phase in* $cd_3as_2$, *Phys. Rev. Lett.* **113** (Dec, 2014) 246402.

[81] K. Ploog, *Molecular beam epitaxy of III–V compounds*. Springer, 1980.

[82] Y. Suzuki, Y. Ohmori, and H. Okamoto, *Influence of [v]/[iii] beam ratio on crystal qualities of gasbalsb superlattice films grown by molecularbeam epitaxy*, *Journal of Applied Physics* **59** (1986), no. 11 3760–3767.

[83] T. Zhang, S. K. Clowes, M. Debnath, A. Bennett, C. Roberts, J. J. Harris, R. A. Stradling, L. F. Cohen, T. Lyford, and P. F. Fewster, *High-mobility thin insb films grown by molecular beam epitaxy*, *Applied Physics Letters* **84** (2004), no. 22 4463–4465.

[84] E. Hall and H. Kroemer, *Surface morphology of gasb grown on (111)b gaas by molecular beam epitaxy*, *Journal of Crystal Growth* **203** (1999), no. 3 297 – 301.

[85] A. Y. Babkevich, R. A. Cowley, N. J. Mason, P. A. Shields, T. Stadelman, S. Brown, D. Mannix, and D. Paul, *Structure of gasb layers grown on (111) gaas surfaces*, *Journal of Applied Physics* **96** (2004), no. 5 3012–3019.

[86] M. C. Debnath, T. D. Mishima, M. B. Santos, K. Hossain, and O. W. Holland, *Improved electron mobility in insb epilayers and quantum wells on off-axis ge (001) substrates*, *Journal of Applied Physics* **111** (2012), no. 7 073525.

[87] G. A. Devenyi, S. Y. Woo, S. Ghanad-Tavakoli, R. A. Hughes, R. N. Kleiman, G. A. Botton, and J. S. Preston, *The role of vicinal silicon surfaces in the formation of epitaxial twins during the growth of iii-v thin films*, *Journal of Applied Physics* **110** (2011), no. 12 124316.

[88] Y. Kajikawa, Y. Son, H. Hayase, H. Ichiba, R. Mori, K. Ushirogouchi, and M. Irie, *Suppression of twin generation in the growth of gaas on ge (111) substrates*, *Journal of Crystal Growth* **477** (2017) 40 – 44. Proceeding of the 19th International Conference on Molecular Beam Epitaxy.

[89] M. Rebaud, M.-C. Roure, V. Loup, P. Rodriguez, E. Martinez, and P. Besson, *Chemical treatments for native oxides removal of GaAs wafers*, *ECS Transactions* **69** (oct, 2015) 243–250.

[90] A. Guilln-Cervantes, Z. Rivera-Alvarez, M. Lpez-Lpez, E. Lpez-Luna, and I. Hernndez-Caldern, *Gaas surface oxide desorption by annealing in ultra high vacuum*, *Thin Solid Films* **373** (2000), no. 1 159 – 163. Proceedings of the 11th International Conference on Thin Films.

[91] D. Fuster, L. Gins, Y. Gonzlez, J. Herranz, and L. Gonzlez, *Low temperature oxide desorption in gaas (111)a substrates*, *Thin Solid Films* **537** (2013) 70 – 75.

[92] Y. Luo, D. Slater, M. Levy, and R. Osgood, *Chemical preparation of cdte(100) and (110) surfaces using atomic hydrogen*, *Applied Surface Science* **104-105** (1996) 49 – 56. Proceedings of the Fifth International Conference on the Formation of Semiconductor Interfaces.

[93] G. Springholz, *Surface modifications due to strain relaxation in lattice-mismatched heteroepitaxy*, .

[94] D. A. Kealhofer, H. Kim, T. Schumann, M. Goyal, L. Galletti, and S. Stemmer, *Basal-plane growth of cadmium arsenide by molecular beam epitaxy*, *Phys. Rev. Materials* **3** (Mar, 2019) 031201.

[95] T. Mishima, J. Keay, N. Goel, M. Ball, S. Chung, M. Johnson, and M. Santos, *Anisotropic structural and electronic properties of insb/alxin1xsb quantum wells grown on gaas (001) substrates*, *Journal of Crystal Growth* **251** (2003), no. 1 551 – 555. Proceedings of the Twelfth International Conference on Molecular Beam Epitaxy.

[96] W. K. Liu, K. J. Goldammer, and M. B. Santos, *Effect of substrate temperature on si compensation in -doped insb and alxin1xsb grown by molecular beam epitaxy*, *Journal of Applied Physics* **84** (1998), no. 1 205–208.

[97] M. A. Ball, J. C. Keay, S. J. Chung, M. B. Santos, and M. B. Johnson, *Mobility anisotropy in insb/alxin1xsb single quantum wells*, *Applied Physics Letters* **80** (2002), no. 12 2138–2140.

[98] T. D. Mishima and M. B. Santos, *Effect of buffer layer on insb quantum wells grown on gaas (001) substrates*, *Journal of Vacuum Science & Technology B: Microelectronics and Nanometer Structures Processing, Measurement, and Phenomena* **22** (2004), no. 3 1472–1474.

[99] T. Mishima, M. Edirisooriya, and M. Santos, *Dislocation filtering at the interfaces between alxin1xsb and alyin1ysb layers*, *Physica B: Condensed Matter* **376-377** (2006) 591 – 594. Proceedings of the 23rd International Conference on Defects in Semiconductors.

[100] T. D. Mishima, M. Edirisooriya, and M. B. Santos, *Reduction of microtwin defects for high-electron-mobility insb quantum wells*, *Applied Physics Letters* **91** (2007), no. 6 062106, [https://doi.org/10.1063/1.2768033].

[101] A. M. Gilbertson, P. D. Buckle, M. T. Emeny, T. Ashley, and L. F. Cohen, *Suppression of the parasitic buffer layer conductance in insb/al$_x$in$_{1-x}$sb heterostructures using a wide-band-gap barrier layer*, *Phys. Rev. B* **84** (Aug, 2011) 075474.

[102] J. Solomon, L. Petry, and D. Tomich, *Optimizing gasb(111) and gasb(001) surfaces for epitaxial film growth*, *Thin Solid Films* **343-344** (1999) 500 – 503.

[103] G. Williams, C. Whitehouse, A. Cullis, N. Chew, and G. Blackmore, *Growth of cdte-insb multilayer structures on (100) insb substrates using molecular beam epitaxy*, *Applied physics letters* **53** (1988), no. 19 1847–1849.

[104] A. Bracker, M. Yang, B. Bennett, J. Culbertson, and W. Moore, *Surface reconstruction phase diagrams for inas, alsb, and gasb*, *Journal of crystal growth* **220** (2000), no. 4 384–392.

[105] Y. Ran, Y. Zhang, and A. Vishwanath, *One-dimensional topologically protected modes in topological insulators with lattice dislocations*, *Nature Physics* **5** (2009), no. 4 298–303.

[106] M. Yamaguchi, *Dislocation density reduction in heteroepitaxial iii-v compound films on si substrates for optical devices*, *Journal of Materials Research* **6** (1991), no. 2 376384.

[107] T. D. Mishima and M. B. Santos, *Impact of structural defects upon electron mobility in insb quantum wells*, *Journal of Applied Physics* **109** (2011), no. 7 073707, [https://doi.org/10.1063/1.3563587].

[108] Y. Shi, D. Gosselink, V. Y. Umansky, J. L. Weyher, and Z. R. Wasilewski, *Threading dislocations in mbe grown alinsb metamorphic buffers: Revealed and counted*, *Journal of Vacuum Science & Technology B* **35** (2017), no. 2 02B112, [https://doi.org/10.1116/1.4978025].

[109] J. Matthews and A. Blakeslee, *Defects in epitaxial multilayers: I. misfit dislocations*, *Journal of Crystal growth* **27** (1974) 118–125.

[110] L. Galletti, T. Schumann, T. E. Mates, and S. Stemmer, *Nitrogen surface passivation of the dirac semimetal* $Cd_3As_2$, *Phys. Rev. Materials* **2** (Dec, 2018) 124202.

[111] C. WEISBUCH and B. VINTER, *Quantum Semiconductor Structures*. Academic Press, San Diego, 1991.

[112] J. P. Harrang, R. J. Higgins, R. K. Goodall, P. R. Jay, M. Laviron, and P. Delescluse, *Quantum and classical mobility determination of the dominant scattering mechanism in the two-dimensional electron gas of an algaas/gaas heterojunction*, *Phys. Rev. B* **32** (Dec, 1985) 8126–8135.

[113] E. H. Hwang and S. Das Sarma, *Single-particle relaxation time versus transport scattering time in a two-dimensional graphene layer*, *Phys. Rev. B* **77** (May, 2008) 195412.

[114] Y. Horikoshi, M. Kawashima, and H. Yamaguchi, *Migration-enhanced epitaxy of GaAs and AlGaAs*, *Japanese Journal of Applied Physics* **27** (feb, 1988) 169–179.

[115] Y. Horikoshi, *Migration-enhanced epitaxy of GaAs and AlGaAs*, *Semiconductor Science and Technology* **8** (jun, 1993) 1032–1051.

[116] Y. Horikoshi, H. Yamaguchi, F. Briones, and M. Kawashima, *Growth process of iiiv compound semiconductors by migration-enhanced epitaxy*, *Journal of Crystal Growth* **105** (1990), no. 1 326 – 338.

[117] T. Ando, A. B. Fowler, and F. Stern, *Electronic properties of two-dimensional systems*, *Rev. Mod. Phys.* **54** (Apr, 1982) 437–672.

[118] S. Das Sarma, S. Adam, E. H. Hwang, and E. Rossi, *Electronic transport in two-dimensional graphene*, *Rev. Mod. Phys.* **83** (May, 2011) 407–470.

[119] C. Zhang, A. Narayan, S. Lu, J. Zhang, H. Zhang, Z. Ni, X. Yuan, Y. Liu, J.-H. Park, E. Zhang, W. Wang, S. Liu, L. Cheng, L. Pi, Z. Sheng, S. Sanvito, and F. Xiu, *Evolution of weyl orbit and quantum hall effect in dirac semimetal cd3as2*, *Nature Communications* **8** (2017), no. 1 1272.

[120] A. Narayan, D. Di Sante, S. Picozzi, and S. Sanvito, *Topological tuning in three-dimensional dirac semimetals*, *Phys. Rev. Lett.* **113** (Dec, 2014) 256403.

[121] T. Schumann, L. Galletti, D. A. Kealhofer, H. Kim, M. Goyal, and S. Stemmer, *Observation of the quantum hall effect in confined films of the three-dimensional dirac semimetal* $cd_3as_2$, *Phys. Rev. Lett.* **120** (Jan, 2018) 016801.

[122] M. Uchida, Y. Nakazawa, S. Nishihaya, K. Akiba, M. Kriener, Y. Kozuka, A. Miyake, Y. Taguchi, M. Tokunaga, N. Nagaosa, Y. Tokura, and M. Kawasaki, *Quantum hall states observed in thin films of dirac semimetal cd3as2*, *Nature Communications* **8** (2017), no. 1 2274.

[123] A. Isihara and L. Smrcka, *Density and magnetic field dependences of the conductivity of two-dimensional electron systems*, *Journal of Physics C: Solid State Physics* **19** (dec, 1986) 6777–6789.

[124] G. P. Mikitik and Y. V. Sharlai, *Berry phase and the phase of the shubnikov–de haas oscillations in three-dimensional topological insulators*, *Phys. Rev. B* **85** (Jan, 2012) 033301.

[125] A. Narayanan, M. D. Watson, S. F. Blake, N. Bruyant, L. Drigo, Y. L. Chen, D. Prabhakaran, B. Yan, C. Felser, T. Kong, P. C. Canfield, and A. I. Coldea, *Linear magnetoresistance caused by mobility fluctuations in n-doped* $cd_3as_2$, *Phys. Rev. Lett.* **114** (Mar, 2015) 117201.

[126] S. Jeon, B. B. Zhou, A. Gyenis, B. E. Feldman, I. Kimchi, A. C. Potter, Q. D. Gibson, R. J. Cava, A. Vishwanath, and A. Yazdani, *Landau quantization and quasiparticle interference in the three-dimensional dirac semimetal cd3as2*, *Nature Materials* **13** (2014), no. 9 851–856.

[127] M. Kargarian, Y.-M. Lu, and M. Randeria, *Deformation and stability of surface states in dirac semimetals*, *Phys. Rev. B* **97** (Apr, 2018) 165129.

[128] M. Friesen, S. Chutia, C. Tahan, and S. N. Coppersmith, *Valley splitting theory of* SiGeSiSiGe *quantum wells*, *Phys. Rev. B* **75** (Mar, 2007) 115318.

[129] D. Shao, J. Ruan, J. Wu, T. Chen, Z. Guo, H. Zhang, J. Sun, L. Sheng, and D. Xing, *Strain-induced quantum topological phase transitions in* $na_3Bi$, *Phys. Rev. B* **96** (Aug, 2017) 075112.

[130] C.-K. Chiu, J. C. Y. Teo, A. P. Schnyder, and S. Ryu, *Classification of topological quantum matter with symmetries*, *Rev. Mod. Phys.* **88** (Aug, 2016) 035005.

[131] C. Brüne, C. X. Liu, E. G. Novik, E. M. Hankiewicz, H. Buhmann, Y. L. Chen, X. L. Qi, Z. X. Shen, S. C. Zhang, and L. W. Molenkamp, *Quantum hall effect from the topological surface states of strained bulk hgte*, *Phys. Rev. Lett.* **106** (Mar, 2011) 126803.

[132] X. Dai, T. L. Hughes, X.-L. Qi, Z. Fang, and S.-C. Zhang, *Helical edge and surface states in hgte quantum wells and bulk insulators*, *Phys. Rev. B* **77** (Mar, 2008) 125319.

[133] J. Ruan, S.-K. Jian, H. Yao, H. Zhang, S.-C. Zhang, and D. Xing, *Symmetry-protected ideal weyl semimetal in hgte-class materials*, *Nature Communications* **7** (2016), no. 1 11136.

[134] G. Bednik, *Surface states in dirac semimetals and topological crystalline insulators*, *Phys. Rev. B* **98** (Jul, 2018) 045140.

[135] A. V. Germanenko and G. M. Minkov, *Narrow-gap and gapless semiconductors under uniaxial stress. energy spectrum and galvanomagnetic phenomena*, *physica status solidi (b)* **184** (1994), no. 1 9–67, [https://onlinelibrary.wiley.com/doi/pdf/10.1002/pssb.2221840102].

[136] A. A. Burkov, *Giant planar hall effect in topological metals*, *Phys. Rev. B* **96** (Jul, 2017) 041110.

[137] S. Nandy, G. Sharma, A. Taraphder, and S. Tewari, *Chiral anomaly as the origin of the planar hall effect in weyl semimetals*, *Phys. Rev. Lett.* **119** (Oct, 2017) 176804.

[138] H. Ishizuka and N. Nagaosa, *Robustness of anomaly-related magnetoresistance in doped weyl semimetals*, *Phys. Rev. B* **99** (Mar, 2019) 115205.

[139] X. Dai, Z. Z. Du, and H.-Z. Lu, *Negative magnetoresistance without chiral anomaly in topological insulators*, *Phys. Rev. Lett.* **119** (Oct, 2017) 166601.

[140] S. Nandy, A. Taraphder, and S. Tewari, *Berry phase theory of planar hall effect in topological insulators*, *Scientific Reports* **8** (2018), no. 1 14983.

[141] R. D. dos Reis, M. O. Ajeesh, N. Kumar, F. Arnold, C. Shekhar, M. Naumann, M. Schmidt, M. Nicklas, and E. Hassinger, *On the search for the chiral anomaly in weyl semimetals: the negative longitudinal magnetoresistance*, *New Journal of Physics* **18** (aug, 2016) 085006.

[142] F. Arnold, C. Shekhar, S.-C. Wu, Y. Sun, R. D. dos Reis, N. Kumar, M. Naumann, M. O. Ajeesh, M. Schmidt, A. G. Grushin, J. H. Bardarson, M. Baenitz, D. Sokolov, H. Borrmann, M. Nicklas, C. Felser, E. Hassinger, and B. Yan, *Negative magnetoresistance without well-defined chirality in the weyl semimetal tap*, *Nature Communications* **7** (2016), no. 1 11615.

[143] T. Schumann, M. Goyal, D. A. Kealhofer, and S. Stemmer, *Negative magnetoresistance due to conductivity fluctuations in films of the topological semimetal* $Cd_3As_2$, *Phys. Rev. B* **95** (Jun, 2017) 241113.

[144] O. Breunig, Z. Wang, A. A. Taskin, J. Lux, A. Rosch, and Y. Ando, *Gigantic negative magnetoresistance in the bulk of a disordered topological insulator*, *Nature Communications* **8** (2017), no. 1 15545.

[145] R. Singha, S. Roy, A. Pariari, B. Satpati, and P. Mandal, *Planar hall effect in the type-ii dirac semimetal* $val_3$, *Phys. Rev. B* **98** (Aug, 2018) 081103.

[146] H. Li, H.-W. Wang, H. He, J. Wang, and S.-Q. Shen, *Giant anisotropic magnetoresistance and planar hall effect in the dirac semimetal* $cd_3as_2$, *Phys. Rev. B* **97** (May, 2018) 201110.

[147] P. Li, C. H. Zhang, J. W. Zhang, Y. Wen, and X. X. Zhang, *Giant planar hall effect in the dirac semimetal* $ZrTe_{5-\delta}$, *Phys. Rev. B* **98** (Sep, 2018) 121108.

[148] M. Wu, G. Zheng, W. Chu, Y. Liu, W. Gao, H. Zhang, J. Lu, Y. Han, J. Zhou, W. Ning, and M. Tian, *Probing the chiral anomaly by planar hall effect in dirac semimetal* $cd_3as_2$ *nanoplates*, *Phys. Rev. B* **98** (Oct, 2018) 161110.

[149] H.-Z. Lu and S.-Q. Shen, *Quantum transport in topological semimetals under magnetic fields*, *Frontiers of Physics* **12** (2017), no. 3 127201.

[150] D. Xiao, M.-C. Chang, and Q. Niu, *Berry phase effects on electronic properties*, *Rev. Mod. Phys.* **82** (Jul, 2010) 1959–2007.

[151] A. A. Taskin, H. F. Legg, F. Yang, S. Sasaki, Y. Kanai, K. Matsumoto, A. Rosch, and Y. Ando, *Planar hall effect from the surface of topological insulators*, *Nature Communications* **8** (2017), no. 1 1340.

[152] D. A. Kealhofer, L. Galletti, T. Schumann, A. Suslov, and S. Stemmer, *Topological insulator state and collapse of the quantum hall effect in a three-dimensional dirac semimetal heterojunction*, *Phys. Rev. X* **10** (Feb, 2020) 011050.

[153] A. Yamada and Y. Fuseya, *Angular dependence of magnetoresistance and planar hall effect in semimetals in strong magnetic fields*, arXiv:2010.0707.

[154] B. A. Bernevig and S.-C. Zhang, *Quantum spin hall effect*, *Phys. Rev. Lett.* **96** (Mar, 2006) 106802.